核理研研究報告　第39巻　2006年

ISSN 0385-2105

TOHOKU

RESEARCH REPORT OF LABORATORY OF NUCLEAR SCIENCE

Vol.39 2006

TOHOKU UNIVERSITY

RESEARCH REPORT OF LABORATORY OF NUCLEAR SCIENCE Vol.39 2006 TOHOKU UNIVERSITY

TOHOKU

東北大学大学院理学研究科
原子核理学研究施設

Editors

TAMAE, Tadaaki

OHTSUKI, Tsutomu

HAMA, Hiroyuki

Laboratory of Nuclear Science

Tohoku University

1-2-1 Mikamine, Taihaku, Sendai 982-0826

Japan

Pone: +81, 22-743-3400

Fax: +81, 22-743-3401

Web site: http://www.lns.tohoku.ac.jp/

982-0826 仙台市太白区三神峯1-2-1

東北大学大学院理学研究科

附属原子核理学研究施設

電話　022-743-3400

Fax　022-743-3401

核理研研究報告　第39巻

2007年3月発行

発行所　東北大学大学院理学研究科
附属原子核理学研究施設
仙台市太白区三神峯1-2-1（郵便番号982－0826）
電話　022－743－3400

印刷所　株式会社　東北プリント
仙台市青葉区立町24番24号
TEL　022（263）1166㈹

RESEARCH REPORT OF
LABORATORY OF NUCLEAR SCIENCE
TOHOKU UNIVERSITY

Volume 39 March 2007

Laboratory of Nuclear Science, Tohoku University,
1-2-1, Mikamine, Taihaku, Sendai 982-0826, Japan

Preface

This issue of Research Report of Laboratory of Nuclear Science reports research activities of the LNS performed in the 2005 academic/fiscal year (April 2005-March 2006). Major research activities are based on the electron accelerator complex consisting of the 300-MeV LINAC and the 1.2-GeV STB ring. The accelerators have altogether provided a beam time of about 2,200 hours for various experiments through the year.

The (γ, η) and (γ, π^0) measurements performed with the SCISSORS II spectrometer at the Gev- γ experimental hall 2 are finished in this year, and a construction of a 4π spectrometer called FOREST has been planned. In the experimental hall 2, a construction of a larger spectrometer called New NKS spectrometer has started: A dipole magnet which was a main part of the cyclotron at the Cyclotron Radio Isotope Center was brought in and placed on the gamma-ray beam line. In this occasion, the vacuum chamber of the STB Tagger 1 was improved to reduce materials for recoil electrons to pass through. Experiments on coherent radiation were performed by using pulsed electron beams from the LINAC. Various radioactive isotopes were produced by using high intensity beams below 50 MeV at the experimental hall 1. They were served for element analyses as well as for detailed study of decay properties.

We hope that this Report will serve as a quick overview of the present LNS activities over a variety of nuclear research fields.

Jirohta KASAGI
Director

Research Report of Laboratory of Nuclear Science
Volume 39, 2006

Contents

核理研研究報告　第39巻　目　次

Ⅰ．原子核物理

Ⅱ．放射化学

Ⅲ．加速器・放射光・測定装置

Ⅳ．論文リスト

Ⅴ．課題採択結果

Ⅰ. Nuclear Physics

(LNS Experiment : #2446, #2506)

Study of Strangeness Photo-production in the Threshold Region at LNS-Tohoku

P. Bydžovský[1], M. Ejima[2], Y. Fujii[2], K. Futatsukawa[2], O. Hashimoto[2], K. Hirose[2], T. Ishikawa[3], S. Kameoka[2], H. Kanda[2], F. Kato[2], S. Kinoshita[2], T. Kinoshita[3], T. Kon[2], O. Konno[4], K. Maeda[2], A. Matsumura[2], Y. Miura[2], H. Miyahara[3], H. Miyase[2], T. Nakabayashi[3], K. Nonaka[2], A. Ohtani[2], Y. Okayasu[2], M. Oyamada[2], A. Sasaki[5], H. Shimizu[3], T. Takahashi[3], T. Tamae[3], H. Tamura[2], T. Terasawa[3], H. Tsubota[2], K. Tsukada[2], S.N. Nakamura[2], H. Nomura[2], M. Ukai[2], D. Uchida[2], H. Yamauchi[2], H. Yamazaki[3], K. Yawata[2], M. Wakamatsu[2], T. Watanabe

[1]*Nuclear Physics Institute, 25068, Res Czech Repubic*
[2] *Department of Physics, Tohoku University, Sendai, 980-8578*
[3]*Laboratory of Nuclear Science, Tohoku University, Sendai, 982-0826*
[4]*Department of Electrical Engineering, Ichinoseki National College of Technology, OIchinoseki, Iwate 010-8502*
[5]*Department of Electrical and Electronic Engineering, Akita University, Akita, 010-8502*

§1. Introduction

The investigation of the kaon production on a nucleon by the electromagnetic interaction provides invaluable information on the strangeness production mechanism, strength of meson-baryon coupling constants and structure of hadrons, being labeled by the strangeness degree of freedom. Such studies using beams of real photons and electrons have been conducted both experimentally and theoretically since the 1950's, taking advantage of the electromagnetic interaction that is understood better than the hadronic interaction. Until now, the experimental studies have been carried out in $p(\gamma, K^+)\Lambda$, $p(\gamma, K^+)\Sigma^0$ and $p(\gamma, K^0)\Sigma^+$ reactions among six isospin channels [1, 2]. However, no data have been measured for the other three channels on a neutron. Theoretically, phenomenological models have been constructed based on measured channels so far. The isobar models, Kaon-MAID [3] and SLA [4], were adopted in the present analysis. The predictions of the photon energy dependence and the kaon angular distribution of the other three channels on a neutron using these models are quite different.

The lack of the key data for strangeness photoproduction of the three channels on a neutron is due to the experimental difficulties to measure neutral kaons and to prepare a neutron target. The measurement of these three strangeness production channels provides much information on the strangeness photoproduction mechanism. In particular, the $n(\gamma, K^+)\Lambda$ reaction has following features:

(1) Since no charge is involved, the t-channel Born term does not contribute.

(2) It is a mirror reaction to $p(\gamma, K^+)\Lambda$.

For the hyperon resonance exchange terms, a coupling constant, $g_{K\Sigma N}$, changes its sign from the isospin symmetry, $g_{K^0\Sigma^0 n} = -g_{K^0\Sigma^0 p}$, resulting the different interference effect. Furthermore, the number

of resonances to be considered is small in the threshold region. Therefore, the $n(\gamma, K^0)\Lambda$ reaction is expected to play an essential role to investigate the strangeness photoproduction mechanism.

In this report, we present the results of photoproduction of neutral kaons on deuterons near the threshold. The resutls from a carbon target are described in Ref. [4].

§2. Experiment

We carried out the experiment of the $d(\gamma, K^0)$ reaction in the threshold region, E_γ = 0.8 ~ 1.1 GeV. The K^0s were measured in $\pi^+\pi^-$ decay mode with Neutral Kaon Spectrometer (NKS), which we installed in LNS-Tohoku. Figure 1 shows a schematic view of NKS which consists of a dipole magnet of 107 cm diameter and 60 cm gap with 0.5 T, straw drift chambers (SDC), cylindrical drift chambers (CDC), inner hodoscope (IH), outer hodoscope (OH) and electron veto counters (EV). The detector configuration was symmetric against the beam line. The solid angle of NKS was about π sr. The CDC and SDC were used to measure particle momenta in the horizontal plane by trajectory reconstruction. The magnetic field map was calculated by TOSCA. IH and OH were used for the time-of-flight measurement and event triggers. The momenta and time-of-flights were used for the particle identification. As a trigger condition, we required more than two charged particles; at least one event both in the left and right arms in coincidence with a tagger signal. EVs were employed to reduce the serious background triggered by $\gamma \rightarrow e^+e^-$ conversion. They covered vertically $\pm$ 2.5 cm in the horizontal plane at OH's positions. The geometrical acceptance was reduced by 8%.

The photon beam was generated from the 1.2 GeV electron beam via bremsstrahlung and its energy was tagged by the STB-tagger system [6]. The typical tagged photon intensity was 2×10^6 /sec and the tagging efficiency was 79 $\pm$ 1 %.

In order to investigate the K^0 quasi-free and elementary production process on a neutron, we used a natural carbon target and a liquid deuterium target. The thickness of both targets are 2.1 g/cm^2 for carbon and 0.54 g/cm^2 for deuterium. The liquid deuterium target system was developed for this experiment and provided the stable liquid-state deuterium during the experimental period [7].

§3. Analysis

The momenta of particles were derived from the curvature of trajectories. Besides, the velocities of particles were calculated from the time of flight and the flight length. The e^+e^- events were removed by rejecting the events of which the vertex position was upstream the target. Figure 2(a) shows the vertex point distribution of the $\pi^+\pi^-$ events. An opening angle (η) cut of $-0.9 < \cos\eta < 0.8$ was applied in order to remove the e^+e^- or vertex mis-reconstruction events. The vertex resolution was estimated to be 1.3 mm in RMS in the beam direction. Most of events were originated in the target. Backgrounds through such as a multi-pion productions, N* and ρ, whose production cross sections are much larger than that of kaon production. Hence, no peak is observed in the invariant mass spectrum as shown in Fig.2(b) for events in the target region. K^0 events are enhanced by selecting vertex points in the decay volume, because K^0_S has a relatively long life time of $c\tau$ = 2.68 cm. Figure 2(c) shows the invariant mass spectrum when events in the decay volume are chosen. The peak of K^0_S is clearly seen as shown in the

figure. Number of K^0 events is about 900 in the present data.

In order to obtain the cross section, we defined the gate in the invariant mass spectrum, $0.46 \leq M(\pi^+\pi^-) < 0.54$ GeV/c^2. Momentum distributions of K^0 were obtained after subtracting background contributions. The origin of the backgrounds were considered as (1) leakage from the target region due to the finite resolution of the vertex point reconstruction, and (2) wrong combination between π^+ from K^0 and π^- from Λ. The first one was estimated from the events originated in the target region, and the second one was estimated by a Geant4 simulation. These estimations gave the shape of the backgrounds, and the magnitude of the backgrounds were adjusted by fitting the invariant mass spectrum. Figure 3 shows the fitting result assuming a gaussian for K^0 and the shapes of backgrounds as estimated in the photon energy from 0.9 to 1.0 GeV (E_{low}) and form 1.0 to 1.1 GeV (E_{high}).

The acceptance of NKS was calculated by a Geant4 simulation. The geometry of NKS was

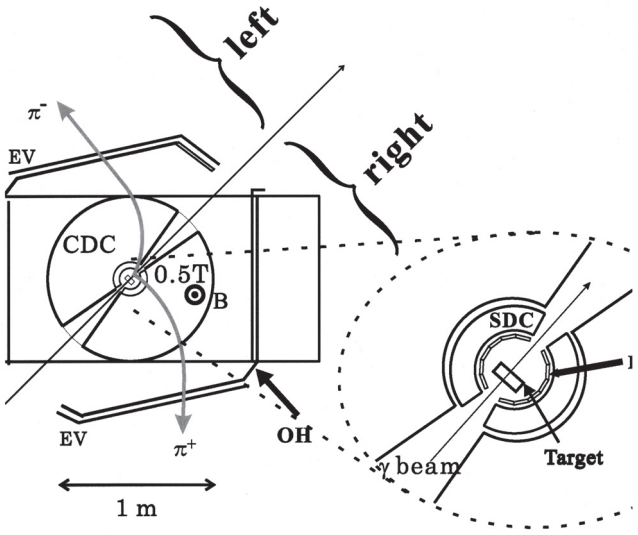

Fig.1. Schematic view of the Neutral Kaon Spectrometer (NKS).

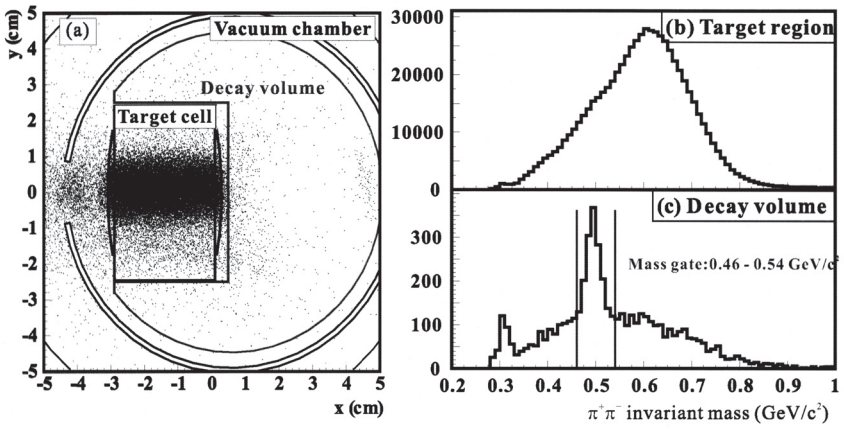

Fig.2. (a) Vertex distribution for $\pi^+\pi^-$ events. The beam comes from left to right. Events come mainly from the target region.(b) and (c) An invariant mass spectrum of $\pi^+\pi^-$ events with the gate that the vertex is in the target for (b) and outside the target denoted by decay volume for (c).

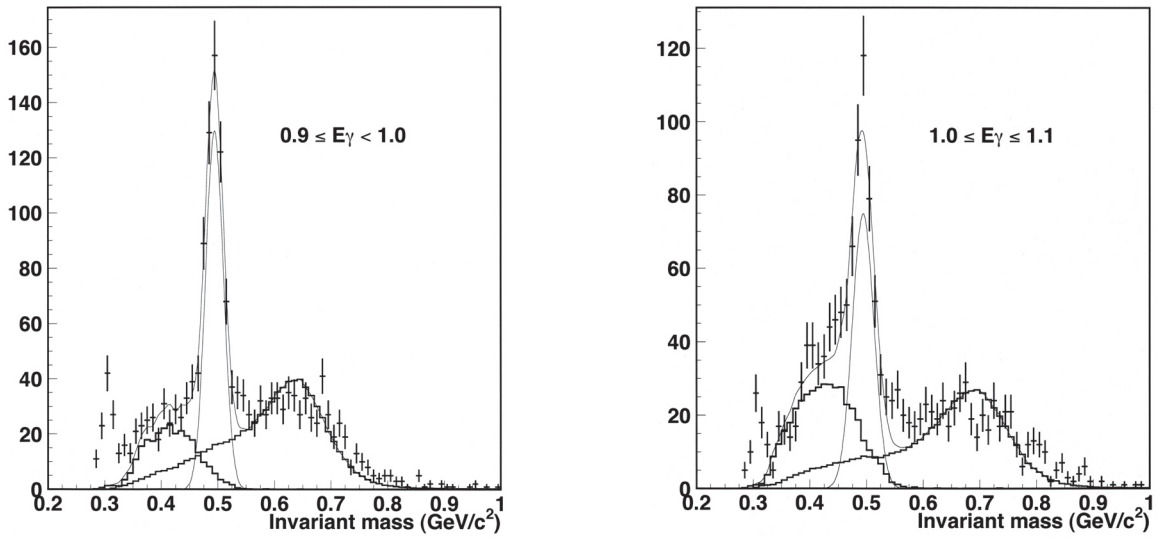

Fig.3. Fitting results of invariant mass spectra in the photon regions from 0.9 to 1.0 GeV (E_{low}, left) and from 1.0 to 1.1 GeV (E_{high}, right). The contribution around 0.4 GeV/c^2 comes from the wrong combination background and that around 0.6 GeV/c^2 comes from the leakage of the target events. The peak near 0.3 GeV/c^2 comes from the e^+e^- events.

considered realistically, and the position and time resolution of the detectors were taken into account. Various analysis efficiencies were also estimated in the acceptance.

§4. Results and Discussion

The obtained momentum spectra of K^0s are shown in Fig. 4. The backgrounds contributions are already subtracted. The integrated momentum range is limited as mentioned in the previous section. The obtained spectra are compared with the calculations using the representative two models, Kaon-MAID [3] and Saclay-Lyon A (SLA) [4]. The lines represent calculations in the plane wave impulse approximation framework using Bonn OBEPQ (One-Boson-Exchange-Potential in Q-space) deuteron wave function [8] by Bydžovský *et al*. [9]. The Kaon-MAID model is the only model to predict the elementary cross section of K^0 photoproduction on a neutron assuming SU(3) symmetry. On the other hand, SLA has an adjustable parameter for $K^0\Lambda$ photoproduction, since the ratio of the decay width between the charged and neutral K_1 resonance ($r_{K_1K\gamma}$) is unknown. In Kaon-MAID, this ratio was obtained from the $\gamma + p \rightarrow K^0 + \Sigma^+$ process. Therefore, the elementary cross sections of SLA are calculated assuming various $r_{K_1K\gamma}$. Kinematical regions are also selected for the calculations similarly to the experimental data.

Since we measured only K^0, the Σ production process may contribute in addition to $K^0\Lambda$ production. From the estimation using Kaon-MAID, the contributions of Σ production are negligibly small in the E_{low} region and sizable large at lower momentum in the E_{high} region. The prediction based on the Kaon-MAID model is consistent with our data in the E_{low} region but too large in the E_{high} region even if the Σ contribution is involved. The spectra calculated by SLA with $r_{K_1K\gamma} = -1.9$ well account for the present results at both energy regions.

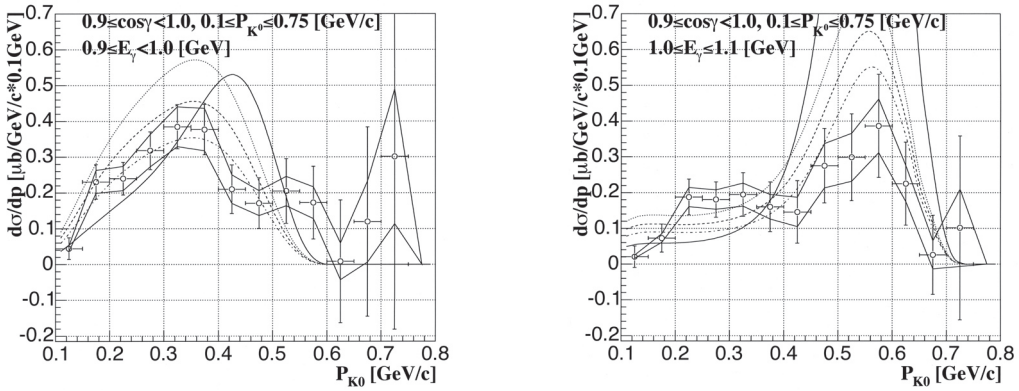

Fig.4. Momentum dependences after the correction for efficiencies and subtraction of backgrounds. The lines represent the calculations using Kaon-MAID (solid), SLA($r_{K\backslash K\gamma} = -1.8$, dotted), SLA($r_{K\backslash K\gamma} = -1.9$, dashed), and SLA($r_{K\backslash K\gamma} = -2.0$, dot-dashed), The photon energy ranges are from 0.9 to 1.0 GeV (E_{low}, left) and from 1.0 to 1.1 GeV (E_{high}, right). The error bars are statistical, and systematic erros are shown by kinked lines around data points.

In the E_{low} region, the shape of the momentum spectrum in the laboratory system mainly depends on the angular distribution in the center of mass system. From the momentum distributions using SLA with various $r_{K\backslash K\gamma}$ values, it is favored that the K^0 photoproduction on a neutron has a backward peak in the center of mass system.

§5. Summary

We have successfully measured neutral kaons, bombarding a liquid deuterium target with a photon beam in the threshold region from 0.8 to 1.1 GeV . It was the first data for K^0 photoproduction on the deuteron in this energy region. The momentum spectra of K^0 production were compared with theoretical spectra calculated assuming isobar models for the elementary process and a realistic deuteron wave function for the target The present experiment has demonstrated a usefulness of the neutral kaon measurement for the investigation of photo strangeness production reactions.

Acknowledgments

This work was supported by Grant-In-Aid for Scientific Research from The Ministry of Education of Japan, Nos. 09304028, 12002001, 14740150 and 16GS0201.

References

[1] D.S. Carman *et al.*: Phys. Rev. Lett. **90** (2003) 131804.

[2] R.G.T. Zegers *et al.*: Phys. Rev. Lett. **91** (2003) 1092001.

[3] F.X. Lee, T. Mart, C. Bennhold, and L.E. Wright: Nucl. Phys. A**695** (2001) 237.

[4] T. Mizutani, C. Fayard, G.H. Lamot, and B. Saghai: Phys. Rev. C**58** (1998) 75.

[5] T. Watanabe *et al.*: nucl-ex/0607022 (2006), submitted to Phys. Lett. B.

[6] H. Yamazaki *et al*.: Nucl. Instr. and Meth. A**536** (2005) 70.

[7] H. Kanda *et al*.: Research Report of LNS, Tohoku University **37** (2004) 27.

[8] R. Machleidt, K. Holinde, and C. Elster: Phys. Rep. **149** (1987) 1.

[9] P. Bydzovsky, M. Sotona, O. Hashimoto, and T. Takahashi: private communications (2004).

(LNS Experiment : #2464, #2551)

Double Pion Photoproduction on Deuteron

K. Hirose[1,*], M. Ejima[1], T. Fujibayashi[1], Y. Fujii[1], K. Futatsukawa[1], O. Hashimoto[1], T. Ishikawa[2], S. Kameoka[1], H. Kanda[1], F. Kato[1], S. Kinoshita[1], T. Kinoshita[2], T. Kon[1], O. Konno[4], K. Maeda[1], A. Matsumura[1], Y. Miura[1], F. Miyahara[2], H. Miyase[1], T. Nakabayashi[2], S.N. Nakamura[1], H. Nomura[1], A. Ohtani[1], Y. Okayasu[1], M. Oyamada[1], A. Sasaki[3], H. Shimizu[2], K. Tsukada[1], T. Takahashi[1,†], T. Tamae[2], H. Tamura[1], T. Terasawa[2], H. Tsubota[1], D. Uchida[1], M. Ukai[1,§], H. Yamauchi[1], H. Yamazaki[2], K. Yawata[1], M. Wakamatsu[1], T. Watanabe[1,‡]

[1] *Department of Physics, Tohoku University, Sendai, 980-8578*
[2] *Laboratory of Nuclear Science, Tohoku University, Sendai, 982-0826*
[3] *Department of Electrical and Electronic Engineering, Akita University, Akita, 010-8502*
[4] *Department of Electrical Engineering, Ichinoseki National College of Technology, Ichinoseki, 021-8511*

Exclusive cross sections for double-pion photoproductions on proton and deuteron were measured in an energy range from 0.8 to 1.1 GeV using tagged photons at Laboratory of Nuclear Science, Tohoku University. We employed the Neutral Kaon Spectrometer (NKS) to detect two pions in the final state, and deduced the cross section for the $\pi^+\pi^-$ photoproduction on the "free" and "bound" proton. We have discriminated between the quasi-free and non-quasi-free process applying the kinematical cut on the missing momentum. We found that the total cross section for the γ"p"$\rightarrow p\pi^+\pi^-$ reaction was about 60% of that for the "free" proton, and this is consistent with the previously obtained data. The one of the dominant part of the non-quasi-free process was found to be the double Δ production. Its cross section is smaller than the previous investigations.

§1. Introduction

In the pion photoproductions above the second resonance region, the doublepion emissions in the final state become important with increasing the photon energy. Recently, data for the multi-particle

* Present address : Laboratory of Nuclear Science, Tohoku University, Sendai, 982-0826
† Present address : Institute of Particle and Nuclear Studies, High Energy Accelerator Organization (KEK), Tukuba, 305-0801
§ Present address : Cyclotron and Radioisotope Center, Tohoku University, Sendai, 980-8678
‡ Present address : Gifu University, Gifu, 501-1193

detection are carried out using not only bubble chambers [1-4] but also large acceptance spectrometers using tagged photon beams.

Since large acceptance photon spectrometers became available, the compilation of the exclusive pion photoproduction data have proceeded including the neutral pion photoproductions [5, 6]. Measurements of double pion phtoproduction using a deuterium target have been also done. The deuteron is often used as a neutron target under the assumption of the quasi-free (QF) process.

One of the result from these studies is that a large isospin dependence is not found in double pion photoproduction on the nucleon. This is thought to be valid considering that the photoabsorption data approximately satisfy the following relation [7-9],

$$\sigma(\gamma d \rightarrow X) \approx 2\,\sigma(\gamma p \rightarrow X). \quad (1)$$

In the case of nuclear targets, the non quasi-free (NQF) process caused by the meson exchange current, the delta current and the final state interaction must be exclusively identified to select the QF channel. The contribution of the NQF process was studied in the $\gamma d \rightarrow pn\pi^+\pi^-$ reaction [10]. The result of this study is that the total cross section for $\pi^+\pi^-$ photoproduction on the "bound" proton is the same as that on the "free" proton within the statistical uncertainties, but the contribution of the NQF process is not negligible.

There are also data on the total cross section for the $\gamma n \rightarrow n\pi^+\pi^-$ reaction which were measured using the deuterium bubble chamber [3, 4]. The comparison between the total cross section for $\pi^+\pi^-$ photoproduction on the "bound" proton and that on the "bound" neutron has been done. Consequently, it is found that these values are the same within the statistical uncertainties, but they are smaller than that of "free" proton,

$$\sigma(\text{"}p\text{"} \rightarrow p\pi^+\pi^-) \approx \sigma(\gamma\,\text{"}n\text{"} \rightarrow n\,\pi^+\pi^-) < \sigma(\gamma p \rightarrow p\pi^+\pi^-), \quad (2)$$

where "p" and "n" denote the "bound" proton and "bound" neutron, respectively. If the cross sections for the "bound" nucleon are the same as those for the "free" nucleon and there is a large contribution of the NQF process, this seems to contradict the result of the photoabsorption data (Eq. (1)).

The NQF process has not been studied in detail. Many body effects seem to appear, even though the deuteron is the simplest nuclei. We have measured double pion photoproduction on the proton and deuteron in order to investigate the NQF process in detail. The aims of this study are :

- To measure the total cross sections for $\pi^+\pi^-$ photoproduction on the "free" and "bound" proton.
- To investigate the contribution of the NQF process and $\Delta^{++}\Delta^-$ production in the $\gamma d \rightarrow pn\pi^+\pi^-$ reaction.

In this article, we describe the results of the double pion photoproduction on the proton and the deuteron to study the contributions of the NQF process.

§2. Experimental Procedure

The experiments were carried out using an internal photon tagging system and a magnetic spectrometer at Laboratory of Nuclear Science, Tohoku University.

2.1 Tagged photon beam

Electrons from the linear accelerator were injected into the Stretcher-Booster (STB) ring and accelerated up to 1.2 GeV. Bremsstrahlung photons were produced by the internal photon tagging system (STB-Tagger) [11]. It consists of a bremsstrahlung radiator, a bending magnet and a tagging hodoscope. A carbon fiber of 11 μmϕ was used for the radiator. It was inserted into the electron orbit by synchronizing the storage-phase of the STB ring. The momenta of the recoil electrons were analyzed in the magnetic field of the bending magnet of the STB ring. The tagging hodoscope consists of 48 finger counters and 12 backup counters. It covers the photon energy range from 0.8 to 1.1 GeV. The energy span of each finger counter was about 6 MeV. The tagging rate was 2 $\sim$ 3 MHz, and the tagging efficiency was 74$\sim$83% in the whole tagging range. The photon beam impinged on the target through a lead collimator, 300-mm long and 10 mm in diameter, placed 3.8 m downstream of the bremsstrahlung radiator.

2.2 Target

A cryogenic system was used for liquid hydrogen and deuterium targets. The target container was a cylinder of 50 mmϕ and 30-mm length. It was located in the center of the spectrometer with its axis parallel to the beam line.

The cylinder was made of 1-mm thick aluminum frame with windows of 75-μm thick Upilex-S film [12] adhered on the both ends. A CFRP (carbon fiber reinforced plastic) chamber was employed for the vacuum insulation around the target. We also provided a beam window with the vacuum chamber.

The pressure and temperature of the target were monitored throughout the experiment. The temperature was automatically controlled and kept at 14.5 K and 19.1K, which correspond to the thickness of 254 mg/cm^2 and 571 mg/cm^2 for the hydrogen and deuterium target, respectively.

2.3 Spectrometer

The Neutral Kaon Spectrometer (NKS) was used for the detection of charged particles. It consists of two sets of drift chambers in the magnetic field, inner and outer hodoscopes, and electron veto counters.

2.3.1 Analyzer magnet

The dipole magnet had a 60-cm pole gap and a 107 cmϕ circular pole face with a nominal field strength of 0.5 T. The distribution of the magnetic field was calculated by the TOSCA code [13] and scaled to the value measured at the center of the magnet. The non-uniformity was taken into account in the off-line data analysis.

2.3.2 Hodoscopes

Two sets of scintillation hodoscopes, inner (IH) and outer hodoscope (OH), were employed to give triggering signals to the online data acquisition system and to measure the time-of-flight (TOF) of charged particles. Each IH was made of six plastic scintillator elements of 20 ~ 25-mm width, 120-mm height and 5-mm thickness. As shown in Fig.1, they were located 60 mm away from the pole axis and surround the target. Since IHs were within the magnetic field, optical-fiber bundles were used to guide scintillation photons to photo-multiplier tubes (PMTs) placed away from the magnetic field. The OHs were made of 34 plastic scintillator elements of 130 ~ 170-mm width, 600-mm length and 10-mm

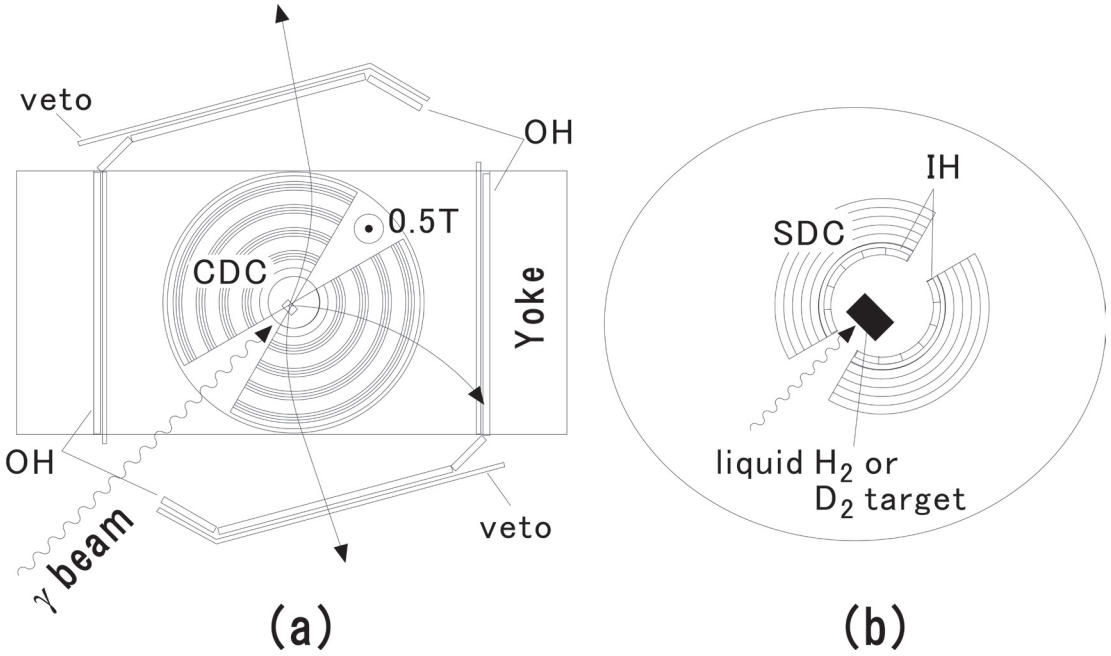

Fig.1. (a) Top view of the Neutral Kaon Spectrometer (NKS). It consists of a dipole magnet, hodoscopes (IH, OH), drift chambers (SDC, CDC) and veto counters. (b) Closeup of the center of the NKS. The target is located inside of the IH.

thickness. The hit position of the charged particle was determined by the time difference between two PMTs attached to the both ends of each scintillator. The typical TOF resolution was 0.5 ns.

2.3.3 Drift chambers

We employed two sets of drift chambers for the track and vertex reconstruction. Each set of the drift chamber consists of a straw type cylindrical drift chamber (SDC) and a honeycomb type one (CDC). They were located just around the IHs (Fig. 1). They covered an angular range from 15° to 165°on the both sides of the beam line. Each SDC contains 78 gold-plated tungsten wires of 20 μmϕ for drift-time readout. The straws made of 180-μm thick aluminized Mylar film were used for field shaping. Each CDC contains 402 gold-plated tungsten wires of 30 μmϕ for drift-time readout and 1094 molybdenum wires of 100 μmϕ for field shaping. All wires were strung vertically and arranged in 16 concentric layers. Mixture of 50% Ar and 50% C_2H_6 was used for the drift gas.

2.3.4 Veto counters

In order to reduce the e^+e^- background along the beam line, the electron veto counters (EV) were employed. Each was made of a plastic scintillator of 1050 to 1250-mm length, 50-mm width and 5-mm thickness. The EVs were placed at the mid plane of the NKS magnetic field.

2.4 Data acquisition

The trigger condition required that there were at least two charged particles detected in coincidence on opposite sides of the beam line. The coincident signal of the left-, right-arm triggers and of the tagger signal was used as the trigger signal,

$$[\mathrm{TRIGGER}] = ([\mathrm{TAG}]\otimes[\mathrm{IH}])\otimes[\mathrm{LEFT}]\otimes[\mathrm{RIGHT}]\otimes\overline{[\mathrm{VETO}]}. \quad (3)$$

The [TAG] is the sum signal of tagging counters, and [IH] is the coincident signal between left- and right-side IH. The [LEFT] is the left-arm trigger defined as a coincident signal of left-side IH and OH without any hit of the EV. The trigger serves as the gate signal for ADCs and as the start signal for TDCs. Signals of the tagger, IH, OH and the EV were converted using the TKO modules. The CAMAC TDCs were used for drift chamber signals.

§3. Data analysis

3.1 Particle identification

The trajectory of a charged particle reconstructed by the SDC + CDC drift chamber system determines the horizontal momentum p_h and horizontal flight length l_h. A spline-fit method was employed for the reconstruction [14]. The time difference between two signals from the PMTs attached to the top and bottom of the OH gives the vertical flight length l_v. The TOF t is given from the time difference between the IH and OH signals. The velocity β and the momentum of the charged particle p

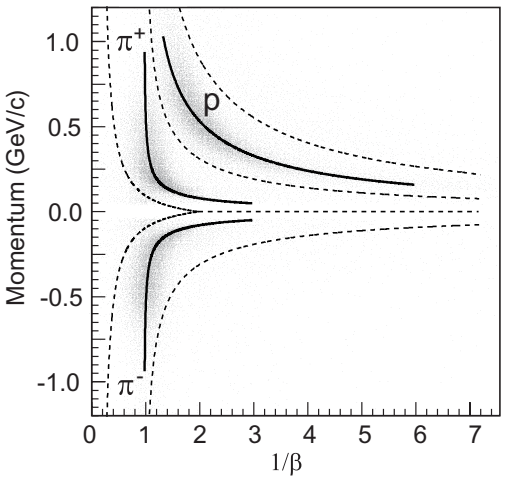

Fig.2. The β^{-1} vs. momentum of charged particles. Negatively charged particles are located in the negative signed momentum region.

are calculated by

$$\beta = \frac{\sqrt{l^2_{\mathrm{h}} + l^2_{\mathrm{v}}}}{ct}, \quad p = p_{\mathrm{h}} \sqrt{1 - \left(\frac{l_{\mathrm{v}}}{l_{\mathrm{h}}}\right)^2}. \tag{4}$$

The particle mass is given by

$$m = \sqrt{\left(\frac{p}{c}\right)^2 \left(\frac{1}{\beta^2} - 1\right)} \quad . \tag{5}$$

Figure 2 shows an example of the two-dimensional plot, where the abscissa and ordinate mean the β^{-1} and momentum, respectively. Solid lines indicate the masses of protons and charged pions. The proton contamination in the π^+ region and the π^+ contamination in the proton region are estimated to be less than 1.4% and less than 0.8%, respectively.

3.2 Vertex distribution

The vertex for the two-track events (V^{2track}) is defined as a point at which the distance between two tracks becomes minimum. Three V^{2track}s are found in the three-track events. As shown in Fig.3 (a), we

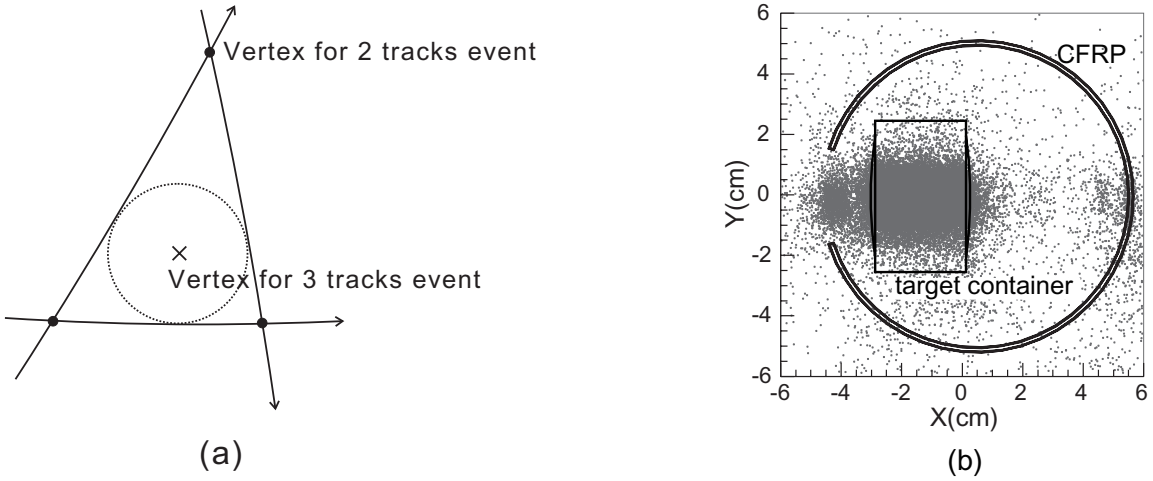

Fig.3. (a) A schematic drawing of the vertex definition for the three-track events. (b) The vertex distribution of three-track events.

determined the vertex for the three-track events V^{3track} as the center of the inscribed circle in the triangle constructed by three V^{2track}s. Figure 3 (b) shows the top view of the V^{3track} distribution. The solid lines indicate the position of the target container and the CFRP vacuum chamber.

3.3 Missing mass distribution

The missing mass for the $d(\gamma, p\pi^+\pi^-)X$,

$$M_X c^2 = \sqrt{\{(E_\gamma + M_d c^2) - (E_p + E_{\pi^+} + E_{\pi^-})\}^2 - c^2\{(p_\gamma + p_{\pi^+} + p_{\pi^-})\}^2}. \tag{6}$$

is shown in Fig.4 (a). The peak corresponding to the neutron mass is selected as the $d(\gamma, p\pi^+\pi^-)n$. The tail in higher energy side is supposed to be from 3π productions. The contamination of this background is estimated to be less than 4%

The M_X distribution for the $d(\gamma, p\pi^-)X$ is shown in Fig.4(b). The peak at a nucleon mass corresponds to the $d(\gamma, p\pi^-)p$. The peak at higher energy side is supposed to be double$^-$, triple-pion productions. In order to reduce them, we imposed cuts on the opening angle between p and π^-, $\cos x_{p\pi} < 0.2$, and the angle of the $p\pi^-$ system, $\theta_{p\pi^-} < 10°$. This cut condition favors the quasi-free (QF) kinematics. The curves are the result of two-Gaussian fitting. We selected $M\mathrm{x} < 1.1$ GeV/c^2 as the "n"$(\gamma, p\pi^-)$. the "n" denotes

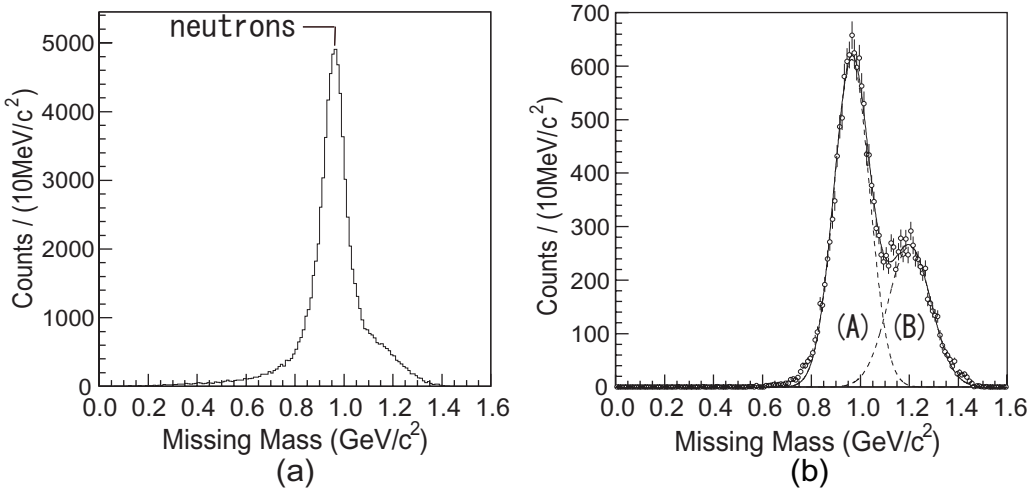

Fig.4. (a) The missing mass distribution for the $d(\gamma, p\pi^+\pi^-)X$. The peak corresponding to the neutron mass is selected as the $d(\gamma, p\pi^+\pi^-)n$. (b) The missing mass distribution for the $d(\gamma, p\pi^-)X$. It consists of two peaks as shown by dashed lines. The peak (A) is from $d(\gamma, p\pi^-)p$, and the peak (B) is thought to be from multi-pion productions.

the bound neutron in the deuteron. The contamination of the multi-pion background is estimated to be 2 ~ 15% in the entire photon energy range.

3.4 Invariant mass distribution

The invariant mass distributions for $N\pi$ and $\pi^+\pi^-$ pair in the $\gamma p \rightarrow p\pi^+\pi^-$ reaction are shown in Fig.5. Curves are the fitting results of Monte Carlo simulations described later. As reported in Refs. [1] and [15], the $\Delta^{++}\pi^-$ channel has a large contribution in this energy region. The peak around 1.35 GeV/c^2 in the $p\pi^-$ invariant mass corresponds to the $\Delta^{++}\pi^-$ channel, and the bump structure around 1.2 GeV/c^2 is thought to be the Δ^-.

The neutron momentum distribution for the $d(\gamma, p\pi^+\pi^-)n$ obtained from the missing momentum is shown in Fig.6. The solid curve corresponding to the nucleon momentum in the deuteron is derived by the simulation using Hulthén wave function [16]. The peak shifts toward higher momentum compared to Hulthen wave function because of the momentum resolution of the detected particles. If the

$p\pi^+\pi^-$ final state is produced through the QF kinematics with a neutron spectator, the neutron momentum (p_n) distribution should correspond to this curve. We selected $p_n < 0.2$ GeV/c as the "p"(γ, $p\pi^+\pi^-$). The "p" denotes the bound proton in the deuteron. It should be noted that the QF process with a proton spectator is also possible. But the momentum threshold of the NKS, about 0.25 GeV/c for protons, precludes the detection of these events almost entirely. We selected $p_n > 0.3$ GeV/c as the non quasi-free (NQF) kinematics in the $d(\gamma, p\pi^+\pi^-)n$.

The $N\pi$ invariant masses for the γ"p" $\rightarrow p\pi^+\pi^-$ reaction are shown in Fig.7. They are similar to those

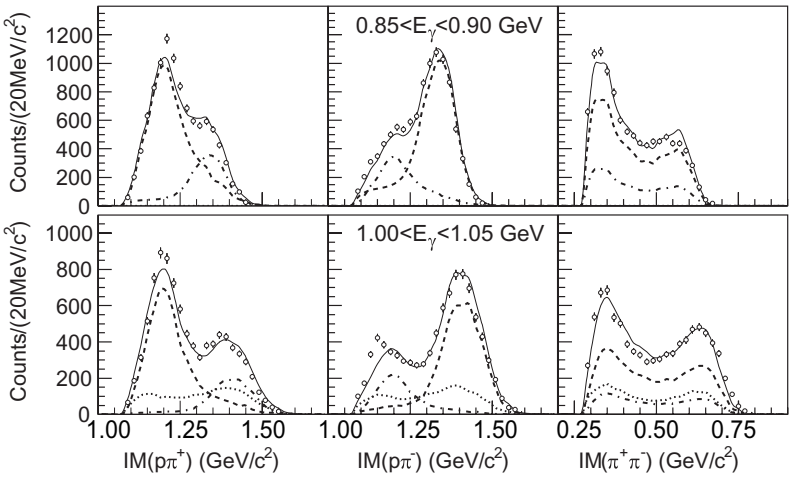

Fig.5. Invariant masses for the $\gamma p \rightarrow p\pi^+\pi^-$ reaction at two photon energies. The $\Delta^{++}\pi^-$ channel has a large contribution in this energy region. Curves show results of Monte Carlo simulations (see text). The dashed, dot-dashed and dotted curves represent the invariant masses for the $\Delta^{++}\pi^-$, $\Delta^0\pi^+$ channel and the three-body-phase-space simulation, respectively. The solid curves are the sums of them.

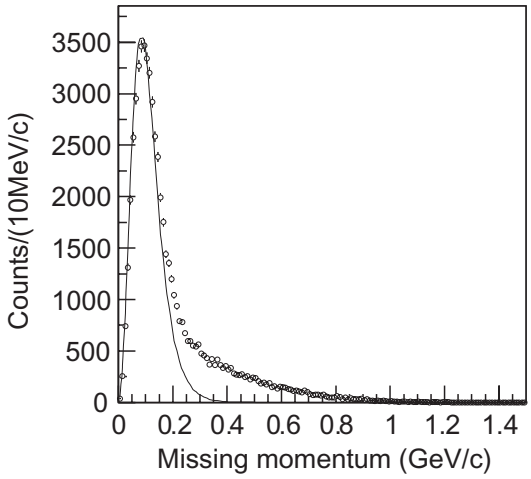

Fig.6. The neutron momentum distribution for the $d(\gamma, p\pi^+\pi^-)n$. The solid curve indicates the momentum distribution of the nucleon in the deuteron.

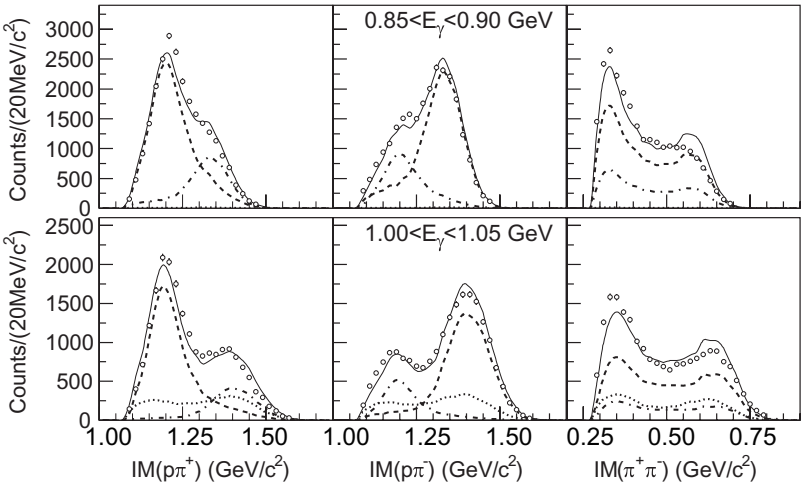

Fig.7. Invariant masses for the γ "p"$\rightarrow p\pi^+\pi^-$ reaction at two photon energies. Curves show results of Monte Carlo simulations (see text). The dashed, dot-dashed and dotted curves represent the invariant masses for the $\Delta^{++}\pi^-$, $\Delta^0\pi^+$ channel and the three-body-phase-space simulation, respectively. The solid curves are the sums of them.

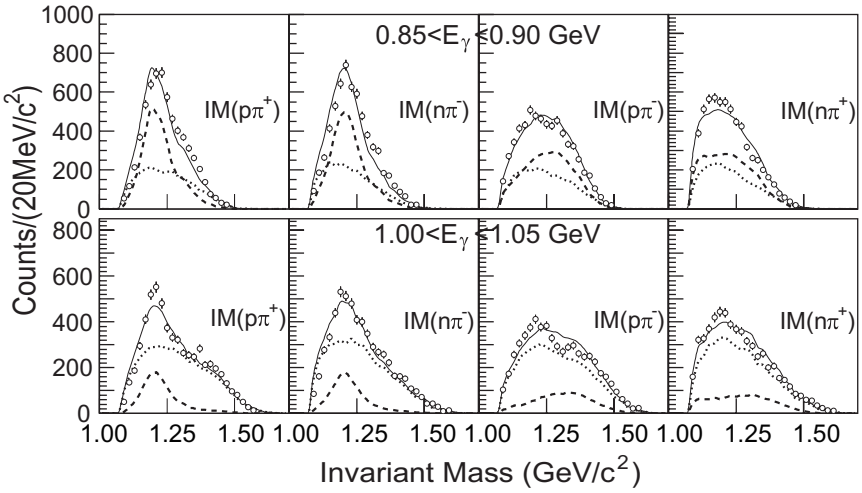

Fig.8. Invariant masses for the NQF process in the $d(\gamma, p\pi^+\pi^-)n$ at two photon energies. In this case, the peak of the Δ^- also appears. Curves show results of Monte Carlo simulations (see text). The dashed and dotted curves represent the invariant masses for the $\Delta^{++}\Delta^-$ channel and the four-body-phase-space simulation, respectively. The solid curves are the sums of them.

of the $\gamma p\rightarrow p\pi^+\pi^-$)n. reaction. Figure 8 shows the invariant masses in the NQF kinematics of the $d(\gamma, p\pi^+\pi^-)n$. Not only the peak of the Δ^{++} but also that of the Δ^- can be seen. A two-dimensional display of $p\pi^+$ and $n\pi^-$ invariant mass is shown in Fig.9. This figure suggests that there exists a large amount of the simultaneous excitation of two Δs.

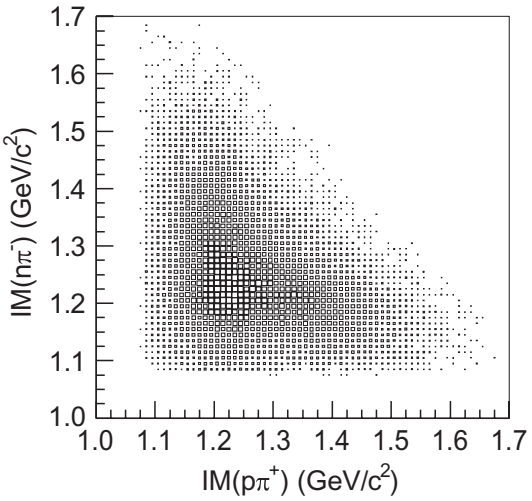

Fig.9. A two-dimensional display of $p\pi^+$ and $n\pi^-$ invariant mass.

3.5 Simulation

We have done Monte Carlo simulations, incorporating the geometry of the present experiment, in order to calculate the NKS acceptance and to separate each channel. The simulation outputs are transformed into the same format and analyzed in the same way as the experimental data.

We consider the $\Delta^{++}\pi^-$, $\Delta^0\pi^+$ channel and the three-body-phase-space as the channels in the $\gamma p \rightarrow p\pi^+\pi^-$ and γ"p" $\rightarrow p\pi^+\pi^-$ reaction. The angular distributions of the Δ^{++} were taken from Ref. [1]. We assume an isotropic angular distribution for the p and π^+ in the rest frame of the Δ^{++}. The $\Delta^0\pi^+$ was treated in the same manner as the $\Delta^{++}\pi^-$ described above. For the NQF in the $d(\gamma, p\pi^+\pi^-)n$, the $\Delta^+\Delta^-$ channel and the four-body-phase-space were taken into account. The $\Delta^+\Delta^0$ channel should also contribute. The Clebsh-Gordan coefficients lead to the following probability ratio of

$$\frac{\sigma(\Delta^{++}\Delta^- \rightarrow pn\pi^+\pi^-)}{\sigma(\Delta^+\Delta^0 \rightarrow pn\pi^+\pi^-)} = 9. \tag{7}$$

The most parts of the $\Delta^+\Delta^0$-decay contain at least one neutral pion. We exclude this channel, because it is invisible in the present experiment.

The sum of the simulated invariant masses were fitted to the experimental data. The curves in Figs. 5, 7 and 8 represent the results of this invariant mass fitting. The fractions of each channel were derived from this fitting. For example, the fraction of the $\Delta^{++}\Delta^-$ channel in the $\gamma p \rightarrow p\pi^+\pi^-$ reaction is given by

$$r_{\Delta^{++}\pi^-} = \frac{Y^{\mathrm{sim}}_{\Delta^{++}\Delta^-}}{Y^{\mathrm{sim}}_{\Delta^{++}\Delta^-} + Y^{\mathrm{sim}}_{\Delta^0\Delta^-} + Y^{\mathrm{sim}}_{\mathrm{3BPS}}}, \tag{8}$$

where the Y^{sim} is the fitted yield of each channel. The subscript 3BPS means the three-body-phase-space. We can obtain the experimental yield of the $\Delta^{++}\pi^-$ channel by

$$Y_{\Delta^{++}\pi^-} = Y_{p\pi^+\pi^-} r_{\Delta^{++}\pi^-}, \tag{9}$$

where the $Y_{p\pi^+\pi^-}$ is the experimental yield of the $\gamma p \rightarrow p\pi^+\pi^-$ reaction.

§4. Results and Discussion

The cross section for the i-th channel is calculated by

$$\sigma_i = \frac{Y r_i}{N_T N_\gamma \ \varepsilon_{DAQ} \ \varepsilon_{DC} \ \varepsilon^n_{track} \ \eta_i}, \tag{10}$$

where N_T is the number of the target atoms per unit area, N_γ is the number of the incident photons, Y is the total yield, r_i is the fraction of the i-th channel which is obtained by the invariant mass fitting, ε_{DAQ} is the data-acquisition efficiency, ε_{DC} is the selection efficiency of track candidates, and ε^n_{track} is the tracking efficiency. The number of the reconstructed tracks is n. The acceptance correction factor of the i-th channel η_i is obtained by the simulation and given as the ratio of the number of accepted events to that of the generated ones. The total cross section is given as the sum of the partial cross sections,

$$\sigma_{tot} = \Sigma \sigma_i . \tag{11}$$

The σ_{tot} for the $\gamma "n" \rightarrow p\pi^-$ reaction is shown in Fig.10. The error bars represent the statistical uncertainties. The results of previous works of Refs. [17-19] are also shown for comparison.

The total cross sections for the $\gamma p \rightarrow p\pi^+\pi^-$ and $\gamma p \rightarrow \Delta^{++}\pi^-$ reaction are shown in Fig.11 (a) and (b),

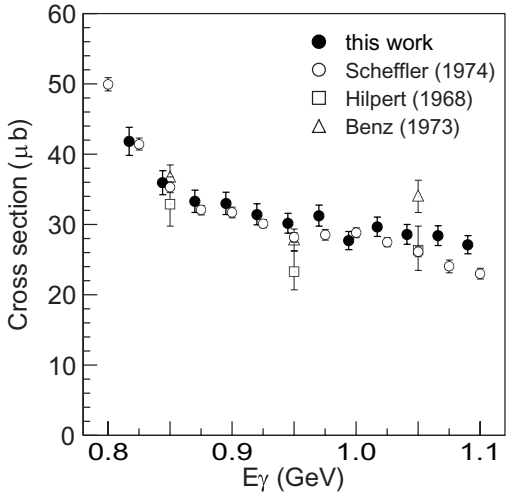

Fig.10. The σ_{tot} for the $\gamma d \rightarrow pp\pi^-$. The filled circles show the results of this work. The open circles, squares and triangles represent the results of Sheffler *et al*. [17], Hilpert *et al*. [18] and Benz *et al*. [19].

respectively. The error bars represent the statistical uncertainties. The results of previous works of ABBHHM [1] and SAPHIR [15] are also shown for comparison. Our results show good agreement with them.

The σ_{tot} for the $\gamma "p" \rightarrow p\pi^+\pi^-$ reaction is shown in Fig.12 (a). The error bars represent the statistical uncertainties. The results of previous works of Refs. [3, 4, 10] are also shown for comparison. The data of Refs. [3, 4] were measured using deuteron bubble chambers, while those of Ref. [10] were measured using a magnetic spectrometer. From the results of Refs. [4, 10] , the cross section values are about 75 μb around E_γ = 0.8 GeV. They are close to that of the $\gamma p \rightarrow p\pi^+\pi^-$ reaction. But from our results, it turned

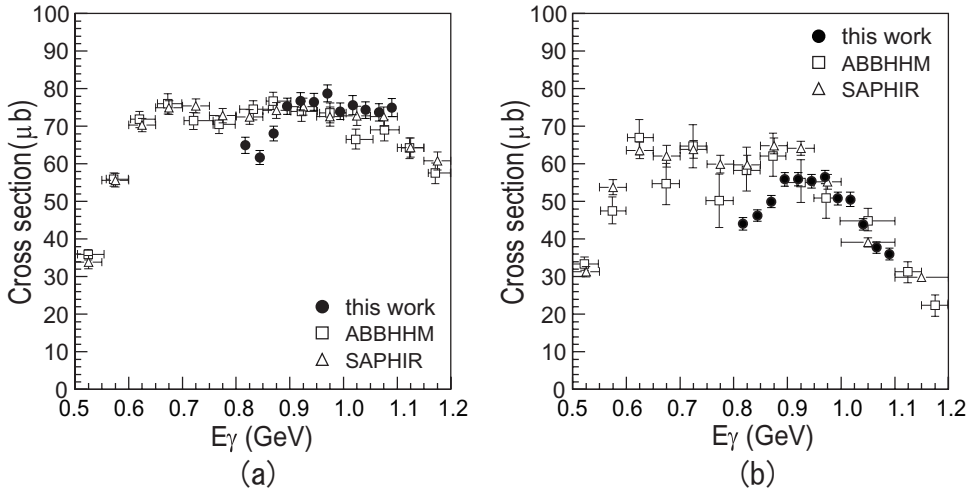

Fig.11. (a) The σ_{tot} for the $\gamma p \rightarrow p\pi^+\pi^-$. (b) The cross section for the $\gamma p \rightarrow \Delta^{++}\pi^-$. The filled circles show the results of this work. The open squares and triangles represent the results of ABBHHM [1] and SAPHIR [15].

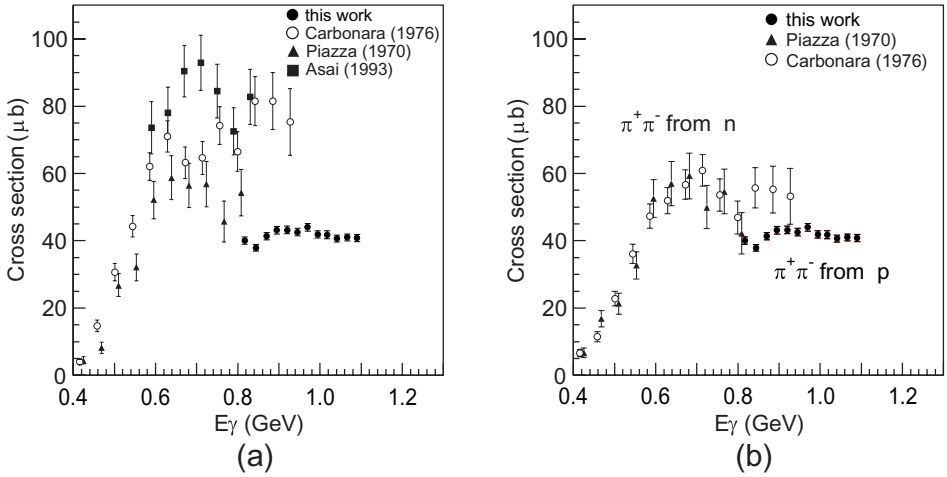

Fig.12. (a) The σ_{tot} for the $\gamma "p" \rightarrow p\pi^+\pi^-$. The filled circles show the results of this work. The filled triangles, open circles and filled squares represent the results of Piazza *et al*. [3]. Carbonara *et al*. [4] and Asai *et al*. [10] (b) Comparison with the $\gamma "n" \rightarrow n\pi^+\pi^-$. The filled circles show the results of this work for the $\gamma "p" \rightarrow p\pi^+\pi^-$, The filled triangles and open circles represent the results of Piazza *et al*. [3] . and Carbonara *et al*. [4] for the $\gamma "n" \rightarrow n\pi^+\pi^-$,

out that the cross section values were smaller than the previous results and were about 40 μb. Our results are in agreement with the results of Ref. [3] . In Fig. 12 (b), the σ_{tot} for the $\gamma "p" \rightarrow p\pi^+\pi^-$ reaction are compared with those for the $\gamma "n" \rightarrow n\pi^+\pi^-$ reaction. Filled triangles and open circles are taken from Refs. [3, 4], respectively. We conclude that the total cross section for the $\gamma "p" \rightarrow p\pi^+\pi^-$ reaction is roughly same as that for the $\gamma "n" \rightarrow n\pi^+\pi^-$ reaction. This seems to be consistent considering that the total photoabsorption cross section on the deuteron is about twice as large as that on the proton.

Figure 13 shows the cross section for the $\gamma d \rightarrow \Delta^{++}\Delta^-$ reaction. Filled circles show the results of this work. The statistical errors are smaller than the plot size. For comparison the results of previous works of Refs. [10, 20, 21] are also shown in this figure. Our results are smaller than others. But the errors of Refs.[10, 21] are very large. The results of this work shows the decreasing behavior with the photon energy.

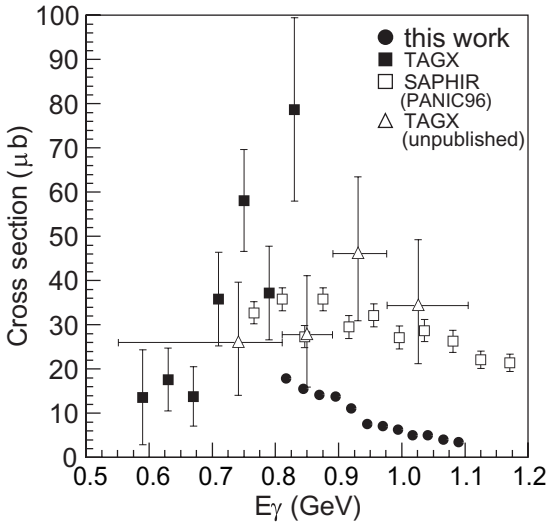

Fig.13. The cross section for the $\gamma d \rightarrow \Delta^{++}\pi^-$. The filled circles show the results of this work. The filled squares, open squares and open triangles represent the results of Asai *et al*, Wada *et al.* [20] and Shinozaki *et al*. [21].

The $\Delta^{++}\Delta^-$ production accounts for 4 % at E_γ= 0.8 GeV and 1% at E_γ= 1.1 GeV of the total photoabsorption cross section on the deuteron.

The cross section for the NQF process has almost no dependency on the photon energy as well as those of the QF process. The cross section ratio of the NQF to the QF process is found to be $\sigma_{NQF} / 2\,\sigma_{QF}$ ~ 0.3.

§5. Summary and Conclusion

Total cross sections have been measured for the $p(\gamma,\ p\pi^+\pi^-)$, $"p"(\gamma,\ p\pi^+\pi^-)$ reaction and the non-quasi-free process of the $d(\gamma,\ p\pi^+\pi^-)n$ reaction in the energy range from 0.8 to 1.1 GeV. The total cross section for the $\gamma p \rightarrow p\pi^+\pi^-$ reaction shows good agreement with previous data. The quasi-free process was selected by applying the kinematical cut on the missing momentum. The total cross section for the $\gamma "p" \rightarrow p\pi^+\pi^-$ reaction was found to be 50 ~ 60% compared to that of the "free" proton.

The cross section for the $\gamma d \rightarrow \Delta^{++}\Delta^{-}$ reaction was measured. The magunitude is smaller than previous data and shows decreasing behaviour with the photon energy.

Acknowledgement

We thank the accelerator and technical stuff at LNS for their contributions to the succsess of the experiment.

References

[1] Aachen-Berlin-Bonn-Hamburg-Heidelberg-Munchen Collaboration: Phys. Rev. **175** (1968) 1669.
[2] Canbridge Bubble Chamber Group: Phys. Rev. **169** (1968) 1081.
[3] A. Piazza *et al*.: Nuovo Cimento **3** (1970) 403.
[4] Carbonara *et al*.: Nuovo Cimento **36A** (1976) 219.
[5] F.Härter *et al*.: Phys. Lett. **B40** (1997) 229.
[6] B. Krusche *et al*.: Eur. Phys. J. **A6** (1999) 309.
[7] T.A. Armstrong *et al*.: Phys. Rev. **D5** (1972) 1640.
[8] T.A. Armstrong *et al*.: Nucl. Phys. **B41** (1972) 445.
[9] M. MacCormic *et al*.: Phys. Rev. **C53** (1996) 41.
[10] M. Asai *et al*.: Z. Phys. **A344** (1993) 335.
[11] H. Yamazaki *et al*.: Nucl. Instr. and Meth. **A536** (2005) 70.
[12] *Ube Ultra-High Heat-Resistant Polyimide Film,* Ube Industries Ltd. (2000).
[13] Vector Fields Limited, Oxford, England.
[14] H. Wind : Nucl. Instr. and Meth. **115** (1974) 431.
[15] C. Wu *et al*.: Eur. Phys. J. **A23** (2005) 317.
[16] D.H. White, R.M. Schectman, and B.M.Chasan: Phys. Rev. **120** (1960) 614.
[17] P.E. Scheffler and P.L. Walden: Nucl. Phys. **B75** (1974) 125.
[18] H.G. Hilpert *et al*.: Nucl. Phys. **B8** (1968) 535.
[19] P. Benz *et al*.: Nucl. Phys. **B65** (1973) 158.
[20] Y. Wada, for the SAPHIR Collaboration: *Particles and nuclei international conference, Williamsburg, Virginia, 1996.*
[21] A. Shinozaki, for the TAGX Collaboration: *private communication.*

(LNS Experiment : #2467)

Study of Giant Resonances in the ^{24}Mg (e, e′α) Reaction

K. Takahashi[1*], K. Abe[1], R. Hashimoto[2], Y. Hayashi[2], K. Hirose[1], T. Ishikawa[2], H. Kanda[1], K. Maeda[1], H. Miyase[1], I. Nishikawa[2], Y. Sato[2], T. Tamae[2], H. Tsubota[1], M. Utoyama[1], M. Wakamatsu[1], M. Watabe[2], Y. Yamaguchi[1]

[1]*Physics Department, Graduate School of Science, Tohoku University, Aramaki, Aoba-ku, Sendai 980-0845*
[2]*Laboratory of Nuclear Science, Tohoku University, Mikamine, Taihaku-ku, Sendai 982-0826*

§1. Introduction

The giant resonances in light nuclei have been investigated by the (e, e′α) reaction in several nuclei. In ^{12}C and ^{40}Ca, where the (e, e′α) reaction through the $E1$ transition is considered to be forbidden by the isospin selection rule because these are $Z = N$ nuclei. The reported $E1$ strength was very small or neglected and the $E2$ or $E0$ strength was dominant [1,2]. Concerning the $E0$ excitation, there are intensive studies by alpha scattering with the intention to find the isoscalar giant monopole resonance (ISGMR) [3-8]. The ISGMR is interesting with regard to the compressibility of nuclear matter. Considering that the (e, e′α) reaction occurs only through isoscalar resonances, the (e, e′α) reaction can be an alternative tool for searching the ISGMR. However, only a fraction of the ISGMR strength is related to α emission channels, although one can reconstruct the strength by using the statistical model for example [2].

This work reports an investigation of the excitation and decay of the giant resonances in ^{24}Mg (e, e′α) reaction.

§2. Experiment

The experiment was performed at Laboratory of Nuclear Science (LNS) in Tohoku University at an incident energy of E_0 =199.31MeV and a scattering angle of $\theta_e = 30^\circ$, corresponding to a momentum transfer of $q = 0.51$ fm^{-1}, using a continuous electron beam from the Stretcher-Booster Ring. A typical electron current during the experiment was from 0.5 to 1 μA.

A ^{24}Mg foil of 2mg/cm^2 and 99.99% enriched was used as a target. The thickness was fixed so that the energy loss of emitted α particles in the target is not too large. The scattered electrons were detected by is a double-focusing magnetic spectrometer with a solid angle of 6 msr. A vertical drift chamber (VDC) was used for detecting the electrons on the focal plane of the spectrometer. Three layers of plastic scintillator were set behind the VDC for trigger of data acquisition. With 5 % of acceptance of the spectrometer, the range of the excitation energy was 15-25 MeV. In this energy range, proton, deuteron, triton, and α particles can contribute to the charged particle decay. The range was chosen

*Present address: ART KAGAKU Co.,Ltd, Muramatsu, Tokai-mura, Naka-bun, Ibaraki 319-1112

because the α decay strength of ^{24}Mg (e, e′α) reaction was very small around 20 MeV or higher according to previous experiments.

Emitted charged particles were detected in coincidence with scattered electrons by using 12 SSD telescopes which consists of two layers of SSD. The first SSD was 50 μm thick and the second was 1 mm thick. These telescopes were placed in a plane rotated about q axis by ϕ =90°. With the out-of-plane detection, the telescopes were able to be arranged without disturbing the electron beam and scattered electrons. Furthermore, an analysis is easier because the longtudinal-transverse interference term vanishes.

§3. Experimental Results and Analysis

Figure 1 shows an example of the missing energy spectrum. According to the Bethe-Bloch formula, the energy loss of α particles in the target is not negligible. So it was taken into account assuming that the emitted particles pass a half of the target thickness.

The separation of α_0 and α_1 events were done by fitting two components of α_0 and α_1 generated by calculation to the experimental spectrum as shown in Fig. 2, because the energy resolution was not enough to separate the peaks clearly. A function used for the fitting is

$$g(E_{\mathrm{miss}}) = a_0 f_{\alpha 0}(E_{\mathrm{miss}} - b, \sigma) + a_1 f_{\alpha 1}(E_{\mathrm{miss}} - b, \sigma) + c, \quad (1)$$

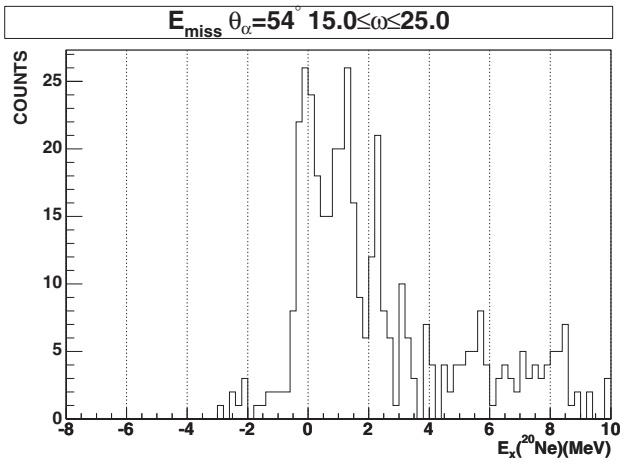

Fig. 1. Missing energy spectrum for excitation energys from 15 to 25 MeV. The excitation energy of the first excited state is 1.14 MeV. It was corrected for the energy loss in the target using the Bethe-Bloch formula by assuming that particle emissions started at the center of the target.

where $f_{\alpha 0}$ and $f_{\alpha 1}$ are functions for the contributions of α_0 and α_1, individually, generated by calculation; E_{miss} is the missing energy, σ is the energy resolution of each of SSD telescopes, and a_0, a_1, b, c are free parameters. Considering low quality of statistics of our data, the most likelihood method was used for fitting by utiliyzing MINUIT for maximization of the likelihood [9].

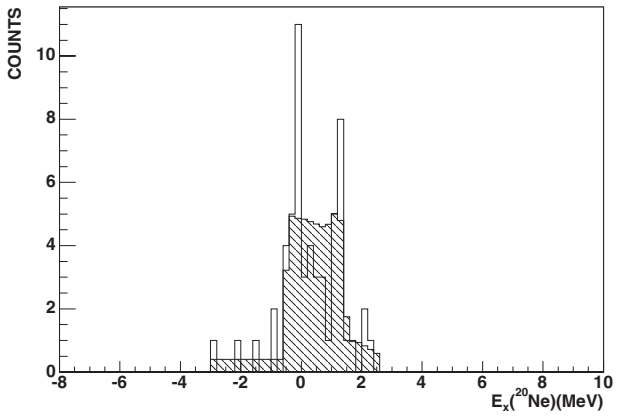

Fig.2. Fitting of the missing energy spectrum with the spectrum generated by the calculation. Hatched histogram is the sum of the calculations fitted with α_0, α_1 and the background. The calculation takes into account the initial energy of α, the energy loss while passing through the target, and the resolution of detectors.

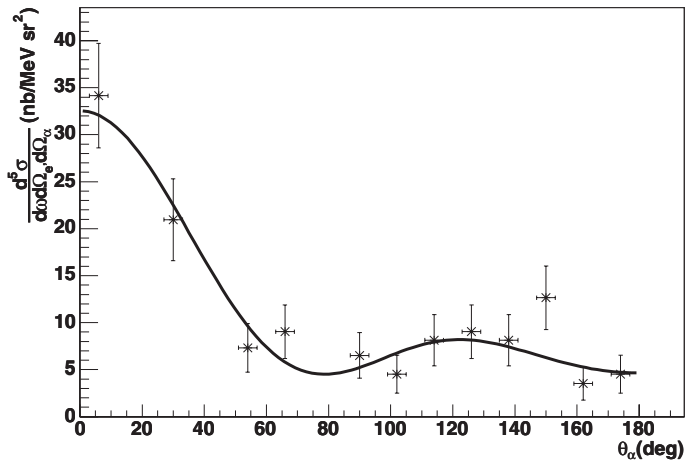

Fig.3. Angular distribution of α_0 for excitation energies of 15-16.4 MeV. The solid line shows a result of fitting by Eq.(2).

Figure 3 shows the angular distribution of the (e, e′α_0) reaction extracted by the method described above. The curve in the figure shows the angular correlation function which we discuss later.

§4. Discussion

In case of spin and parity of $J^\pi = 0^+$ for all of the target, residual nucleus, and emitted particle, the

(e, e′α) differential cross section with multipolarities up to 3 can be simplified as following [10]:

$$\frac{d^5\sigma}{d\omega d\Omega_{e'} d\Omega_{\alpha_0}} = \sigma_{\mathrm{Mott}} \left| \sum_{L=0}^{3} \sqrt{(2L+1)\,A_0(L)}\, F_{CL}\, e^{i\delta L} P_L(\cos\theta_{\alpha_0}) \right|^2, \tag{2}$$

where σ_{Mott} is the Mott cross section, F_{CL} is the longitudinal electric form factor, $A_0(L)$ is the decay coefficient, δ_L is the phase of the product of F_{CL} and $A_0(L)$. Taking $\sqrt{(2L+1)\,A_0(L)}\,F_{CL}$ and δ_L as free parameters, fitting by χ^2 minimization was performed. In the ^{24}Mg (e, e′ α_0) reaction, the angular momentum of the excited state J is defined unambiguously as equal to L because spins of the ground state of the residual nucleus and the emitted particle are zero. Concerning the upper limit of multipolarity in Eq.(2), $L \leq 2$ or $L \leq 3$ is adequate. In the ^{26}Mg (e, e′α) experiment [10], its momentum trasfers are 0.35 and 0.54 fm^{-1}, that are very close to ours. The $E3$ component was not included in the multipole decomposition because it was supposed to be negligible by the DWBA calculation. It was not included also in ^{40}Ca (e, e′ α) experiment [2]. In those results, there is a discrepancy between the experimental angular distribution and the fitted curve at 0°. On the other hand, the result of the ^{12}C (e, e′α) experiment [1] at in $q = 0.24$-0.61 fm^{-1} shows a relatively better fitting result at 0° by including the $E3$. Furthermore, 39% of the $E3$ EWSR (energy weighted sum rule) has been found in ^{24}Mg (e, e′) reaction. Considering these facts, we included the $C3$ component by defining $L \leq 3$ in Eq.(2). The solid line in Fig. 3 is the result of fitting by χ^2 minimization.

Using the parameters obtained by the fitting, the cross section for each multipolarity is given by

$$\frac{d^5\sigma_L}{d\omega d\Omega_{e'}} = \sigma_{\mathrm{Mott}}(2L+1)\,A_0(L)\,|F_{CL}|^2 \int \left[P_L(\cos\theta_{\alpha_0})\right]^2 \mathrm{d}\Omega_{\alpha_0}. \tag{3}$$

Using the values obtained from the fitting, we deduced the strength function $B_{CL}(q)$ which can be represented for spin 0 nuclei by the first Born approximation as follows [11],

$$B_{CL}(q) = \frac{d\sigma_{CL}}{d\Omega_{e'}} \left\{ 4\pi\sigma^1_{\mathrm{Mott}} \left(\frac{\Delta^2}{q^2}\right)^2 f_{\mathrm{rec}}\, q^{2L} [(2L+1)!!\,]^{-2} \right\}^{-1} \tag{4}$$

for $L \geq 1$, and

$$B_{C0}(q) = \frac{d\sigma_{C0}}{d\Omega_{e'}} \left\{ 4\pi\sigma^1_{\mathrm{Mott}} \left(\frac{\Delta^2}{q^2}\right)^2 f_{\mathrm{rec}}\, q^4 [15]^{-2} \right\}^{-1} \tag{5}$$

for $L = 0$, where σ^1_{Mott} is the Mott cross section for $Z = 1$, $\Delta^2 = q^2 - \omega^2$, and f_{rec} is described by

$$f_{\mathrm{rec}} \sim \left[1 + \frac{2k_1}{M} \sin^2\frac{\theta}{2}\right]^{-1}. \tag{6}$$

Furthermore, $B_{CL}(q)$ can be expanded as following,

$$\left(\frac{B_{CL}(q)}{B_{CL}(q=0)}\right)^{\frac{1}{2}} = 1 - \frac{q^2 < r^2_{CL} >_{\mathrm{tr}}}{2(2L+3)} + \frac{q^4 < r^4_{CL} >_{\mathrm{tr}}}{8(2L+3)(2L+5)} - \cdots\cdots, \tag{7}$$

$$< r^{l}_{CL} >_{\rm tr} = \frac{\int r^{L+l+2}\,\rho_L(r)dr}{\int r^{L+2}\,\rho_L(r)dr}\ , \tag{8}$$

for $L \geq 1$, and

$$\left(\frac{B_{C0}(q)}{B_{C0}(q=0)}\right)^{\frac{1}{2}} = 1 - \frac{q^2 < r^2_{C0} >_{\rm tr}}{20} + \frac{q^4 < r^4_{C0} >_{\rm tr}}{840} - \cdots\cdots, \tag{9}$$

$$< r^{l}_{C0} >_{\rm tr} = \frac{\int r^{l+4}\,\rho_0(r)dr}{\int r^{4}\,\rho_0(r)dr} \tag{10}$$

for $L = 0$. $\rho_L(r)$ is the transition charge distribution which is described by Tassie model [12],

$$\rho_L(r) \propto r^{L-1}\frac{d\rho_{\rm g.s.}(r)}{dr} \tag{11}$$

for $L \geq 1$, and

$$\rho_0(r) \propto 3\,\rho_{\rm g.s.}(r) + r\,\frac{d\,\rho_{\rm g.s.}(r)}{dr} \tag{12}$$

for $L = 0$, where $\rho_{\rm g.s.}(r)$ is the charge distribution for the ground state described by the three parameter Fermi model,

$$\rho_{\rm g.s.}(r) = \left(1 + \frac{\omega r^2}{t^2}\right)\left(1 + \exp\left(\frac{r-c}{t}\right)\right)^{-1}. \tag{13}$$

In Eq.(13), we used parameters

$$(\omega, c, t) = (-0.249,\ 3.192,\ 0.604) \tag{14}$$

according to Ref. [12].

$B_{CL}(q=0)$ for individual multipolarities was obtained by calculating the right-hand side of Eqs. (7) and (9) for $q = 0.51$ fm^{-1}, and applying $B_{CL}(q)$ given by Eqs. (4) and (5). Eventually, the strength at the photon point, $B_{CL}(q=\omega)$ was obtained by substituting the $B_{CL}(q=0)$ to Eq. (7) or (9).

Using the $B_{CL}(q=\omega)$ obtained above, the fraction of the energy weighted sum rule (EWSR) is given by

$$R = \frac{B_{CL}(\omega)\,\omega}{EWSR(EL,\,\Delta T)} \times 100, \tag{15}$$

where values of the EWSR are given as follows [13],

$$S(E0) = \frac{(2\hbar)^2}{m_p}\ \frac{Z^2}{A} < r^2 >\ ,$$

$$S(E1, \Delta T{=}1) = \frac{9\hbar^2}{8\pi m_p} \frac{NZ}{A},$$

$$S(EL, L > 1) = \frac{L(2L{+}1)^2\hbar^2}{8\pi m_p} \frac{Z^2}{A} < r^{2L-2} >, \quad (16)$$

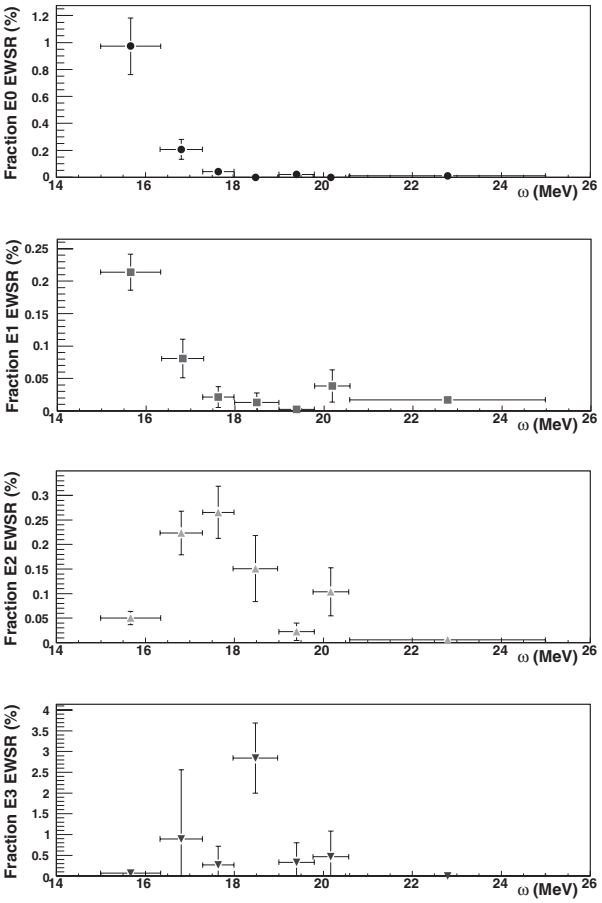

Fig.4. Fraction of the energy weighted sum rule for individual multipolarities.

Figure 4 displays the fraction of the EWSR obtained by Eq. (15), and the result is summarized in Table 1 with results of other experiments. Most of the strength was detected between 15 and 20 MeV. It must be affected by competition between various decay channels. Actually the $E0$ strength with 1.2% of the $E0$ EWSR was detected, while α scattering [6] found 72% with the centroid energy of 21 MeV. The $E1$ strength with 0.4% of the $E1$ EWSR was found, which is comparative with the (α, γ_0) reaction, and very small comparing with the (γ, p_0) reaction. This is the effect of the suppression by the isospin selection rule. The $E2$ strength with 0.8% of the $E2$ EWSR was found. Its distribution is similar to (α, γ) [14] reaction although the amount is different.

In the analysis of electron scattering [15], the separation of $E0$ and $E2$ was not possible by principle.

Table 1. Summary of strength obtained by this work and other experiments on ^{24}Mg.

$L \geq$	experiment	ω (MeV)	R (% EWSR)
0	^{24}Mg(e, e'α_0)	15.0-25.0	1.2 ± 0.2
0	^{24}Mg(α, α)[6]	0-41	72 ± 10
0	^{26}Mg(e, e'α_0)[10]	14.0-26.0	0.2
1	^{24}Mg(e, e'α_0)	15-25	0.4 ± 0.1
1	^{24}Mg(e, e')[15]	9.0-34.0	84.9
1	^{24}Mg(e, α_0)[16]	13.5-22.5	0.43
1	^{24}Mg(γ, p_0)[17]	15.1-23.0	3.3
1	^{24}Mg(γ, n)[18]	16.5-28.0	14.0
1	^{20}Ne(α, γ_0)[14]	14.6-20.6	0.33
1	^{24}Mg(α, α)[6]	0-41	81^{+26}_{-14}
1	^{26}Mg(e, e'α_0)[10]	14.0-26.0	0.45
2	^{24}Mg(e, e'α_0)	15-25	0.8 ± 0.1
2	^{24}Mg(e, e')[15]	0.0-34.0	117
2	^{24}Mg(e, α_0)	13.5-22.5	6.0 ± 0.5
2	^{20}Ne(α, γ_0)[14]	12.0-22.5	11.8 ± 1.0
2	^{24}Mg(α, α)[6]	0-41	72 ± 10
2	^{26}Mg(e, e'α_0)[10]	14.0-26.0	1.4
3	^{24}Mg(e, e'α_0)	15-25	4.8±2.1
3	^{24}Mg(e, e')[15]	0.0-34.0	115
3	^{24}Mg(α, α)[6]	0-41	31^{+9}_{-6}

Figure 5 shows comparison between the $C2(C0)$ differential form factor from (e, e′) inelastic scattering and our results of $C0$ and $C2$ differential cross sections. Comparison is limited to the excitation energies below 20 MeV because the cross sections in our data are small above it. There is a peak around 15 MeV in the (e, e′) reaction. The $C0/C2$ ratio is estimated from the present experiment as $C0/C2=5$ for the corresponding energy bin (15 ～ 16.4 MeV). For a peak between 16 and 18 MeV observed in the (e, e′) reaction the present result represents that $C2$ is dominant. The $C0/C2$ ratio is obtained as $C0/C2 = 0.9$ between 16.4 ～ 17.3 MeV, and $C0/C2 = 0.15$ between 17.3 and 18.0 MeV from our data.

Concerning the $C3$, the strength was 4.8% of the $E3$ EWSR. The validity of including $E3$ can be provided from the q dependence of the form factor investigated in the inelastic scattering experiment. In the inelastic scattering experiment, a significant amount of $E3$ strength was detected at $q = 0.73$ fm^{-1}. According to the q dependence, the $C3$ strength at $q = 0.51$ fm^{-1} (our experiment) is smaller than $C3$ at $q = 0.73$ fm^{-1} by a factor of 4. This difference is not too large to expect the presence of that at $q = 0.51$ fm^{-1}. Furthermore, we compared the ratio $C3/C2$ of the inelastic scattering data and of our work. The strength was reconstructed by the method of statistical model when calculating the ratio for our work. Then we obtained $C3/C2=0.35$ for the inelastic scattering data and 0.48 for our work in the range of

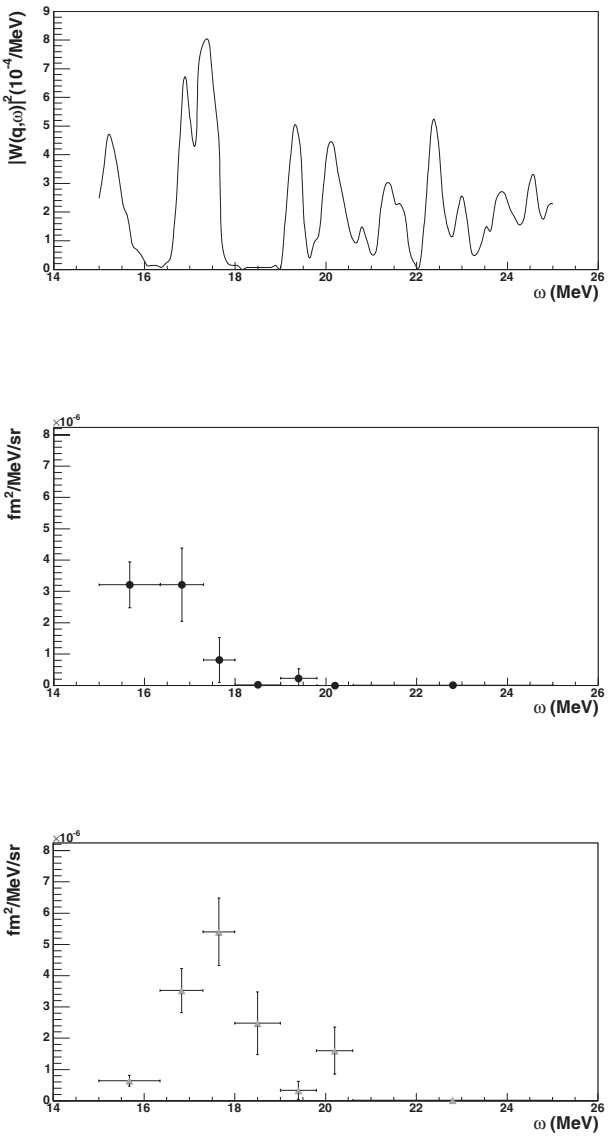

Fig.5. The Differential form factor of $C2(C0)$ at $q=0.73$ fm^{-1} from (e, e') experiment [15](top), differential cross section of $C0$ (middle), and $C2$ (bottom) of our expemriment.

15-19.8 MeV.

In the same manner, we compared the $C1/C2$ ratio in order to examine how much the C1 suppression can be seen. It was 1.79 for the inelastic scattering data and 0.79 for our work, that means the isospin mixing occured with the rate of 44%. That is 24% in the (e, α) [10] and (α, γ) [14] experiments.

§5. Conclusion

The ^{24}Mg(e, e′α) experiments was performed at $q=0.51$fm^{-1} and in the range of excitation energy of 15-25 MeV.

From analysis of the angular distribution for α_0 channel, the $C0$, $C1$, $C2$ and $C3$ form factors were

decomposed to obtain the strength distribution for each multipolarity. The $C0$ and $C2$ components, which was not able to be decomposed by (e, e′) data, were separated and the result indicated that the $C0$ excitation is dominant around 15-16 MeV and the $C2$ ($C0$) peak at 17 MeV found in the (e, e′) experiment is identified to be $C2$ from our result. From the comparison of the $C1/C2$ ratio for the data with (e, e′) result, it was found that the isospin mixing occurs with the rate of 41% in the $E1$ excitation. In our multipole decomposition, the $C3$ component was included that was sometime igonored or neglective in previous studies. Comparing the $C3/C2$ ratio with the (e, e′) result, the $C3$ strength which we obtained is thought to be reasonable. The $C1$ suppression by the isospin selection rule probably makes the $C3$ easier to be identified. Although it was clear that only a fraction of strength can be seen in the (e, e′α) reaction, the coincidence experiment can decompose the $C0$ and $C2$ components. Better statistics is required to discuss more precisely.

References

[1] D.J. DeAngelis, J.R. Calarco, J.E. Wise, H.J. Emrich, R. Neuhausen, and H. Weyand: Phys. Rev. C**52** (1995) 61.

[2] M. Kohl, P. von Neumann-Cosel, A. Richter, G. Schrieder, and S. Strauch: Phys. Rev. C**57** (1998) 3167.

[3] D.H. Youngblood, C.M. Rozsa, J.M. Moss, D.R. Brown, and J.D. Bronson: Phys. Rev. Lett. **39** (1977) 1188.

[4] Y.W. Lui, J.D. Bronson, D.H. Youngblood, Y. Toba, and U.Garg: Phys. Rev. C**31** (1985) 1643.

[5] S. Shlomo and D.H. Youngblood: Phys. Rev. C**47** (1993) 529.

[6] D.H. Youngblood, Y.-W. Lui, and L. Clark: Phys. Rev. C**60** (1999) 014304.

[7] D.H. Youngblood, H.L. Clark, and Y.-W. Lui: Phys. Rev. C**65** (2002) 034302.

[8] B. John, Y. Tokimoto, Y.-W. Lui, H.L. Clark, X. Chen, and D.H. Youngblood: Phys. Rev. C**68** (2003) 014305.

[9] F. James: CERN Program Library Long Writeup D506.

[10] L.A.A. Terremoto, V.P. Likhachev, M.N. Martins, H.J. Emrich, G. Fricke, Th. Kröhl, and K.W. Neff : Phys. Rev. C**56** (1997) 2597.

[11] T. deForest Jr. and J.D. Walecka: Adv. Phys. **15** (1966) 1.

[12] L.J. Tassie: Austr. J. Phys. **9** (1956) 407.

[13] R. Pitthan, F.R. Buskirk, W.A. Houk, and R.W. Moore: Phys. Rev. C**21** (1980) 28.

[14] E. Kuhlmann, E. Ventura, J.R. Calarco, D.G. Mavis, and S.S. Hanna: Phys. Rev. C**11** (1975) 1525.

[15] K. Itoh, S. Osawa, Y. Torizuka, T. Saito, and T. Terasawa: Phys. Rev. C**23** (1981) 945.

[16] M. Hirooka, T. Tanaka, T. Hino, A. Tanaka, T. Tamae, M. Sugawara, and M. Miyase: Nucl. Phys. **A431** (1984) 269.

[17] R.C. Bearse, L. Meyer-Sch\ützmeister, and R.E. Segel: Nucl. Phys. **A116**, (1968) 682.

[18] S.C. Fultz, R.A. Alvarez, B.L. Berman, M.A. Kelly, D.R. Lasher, and T.W. Phillips: Phys. Rev. C**4** (1971) 149.

Status Report of Neutral Kaon photo-production study using Neutral Kaon Spectrometer 2 (NKS2) at LNS-Tohoku

N. Chiga[1], T. Fujibayashi[1], Y. Fujii[1], K. Futatsukawa[1], O. Hashimoto[1], K. Hirose[1], H. Kanda[1], M. Kaneta[2], D. Kawama[2], Y. Ma[2], K. Maeda[2], N. Maruyama[2], A. Matsumura[2], M. Matsuzawa[2], Y. Miyagi[2], H. Miyase[2], S.N. Nakamura[2], K. Nonaka[2], Y. Okayasu[2], K. Shirotori[2], H. Tamura[2], K. Tsukada[2], T. Ishikawa[3], K. Suzuki[3], T. Nakabayashi[3], H. Shimizu[3], T. Tamae[3], H. Yamazaki[3], A. Sasaki[4] and O. Konno[5]

[1]*Department of Physics, Tohoku University, Sendai, Miyagi 980-8578*
[2]*Department of Physics, Tohoku University, Sendai, Miyagi 980-8578*
[3]*Laboratory of Nuclear Science, Tohoku University, Sendai, Miyagi 982-0826*
[4]*Department of Electrical and Electric Engineering, Akita University, Akita, Akita 010-8502*
[5]*Department of Electrical Engineering, Ichinoseki National College of Technology, Ichinoseki, Iwate 010-8502*

§1. Introduction

So far the elementary photo-strangeness production process has been intensively studied based on the high-quality data of the charged kaon channel, $\gamma + p \rightarrow K^+ + \Lambda\,(\Sigma^0)$. However, there were no reliable data for the neutral kaon channel $\gamma + n \rightarrow K^0_S + \Lambda$ and the theoretical investigations suffer seriously from the lack of the data. In order to have reliable data for the neutral kaon photo-production data, we have been putting an effort to measure the $\gamma + n \rightarrow K^0_S + \Lambda$ process in the $\pi^+ \pi^-$ decay channel, using a liquid deuterium target and a tagged photon beam in the threshold region at Laboratory of Nuclear Science, Tohoku University.We have already taken exploratory data quite successfully with use of Neutral Kaon Spectrometer (NKS) at LNS-Tohoku in 2003 and 2004.

We intend to extend the previous experiment by considerably upgrading the original neutral kaon spectrometer to a completely new neutral kaon spectrometer (NKS2), fully replacing the spectrometer magnet, tracking detectors and all the trigger counters. The new spectrometer NKS2 has significantly larger acceptance for neutral kaons compared with NKS, particularly covering forward angles, and much better invariant mass resolution. The estimated acceptance of NKS2 is about 3 to 4 times (depend on momentum and theoretical model) larger for K^0_S than that of NKS. Additionally, it is about 8 to 10 times larger for Lambda. With this advantage, we expect simultaneous measurements of K^0_S and Λ. Additionally, we plan to measure other strangeness production channels and also Λ hyperon polarization in $\gamma + n$ and $\gamma + p$ reactions.

§2. General setup of the NKS2 Experiment

The NKS2 spectrometer is located on the BM4 beam line of the second experimental hall of Laboratory of Nuclear Science (LNS), Tohoku University (see Fig. 1). The incident beam from LINAC

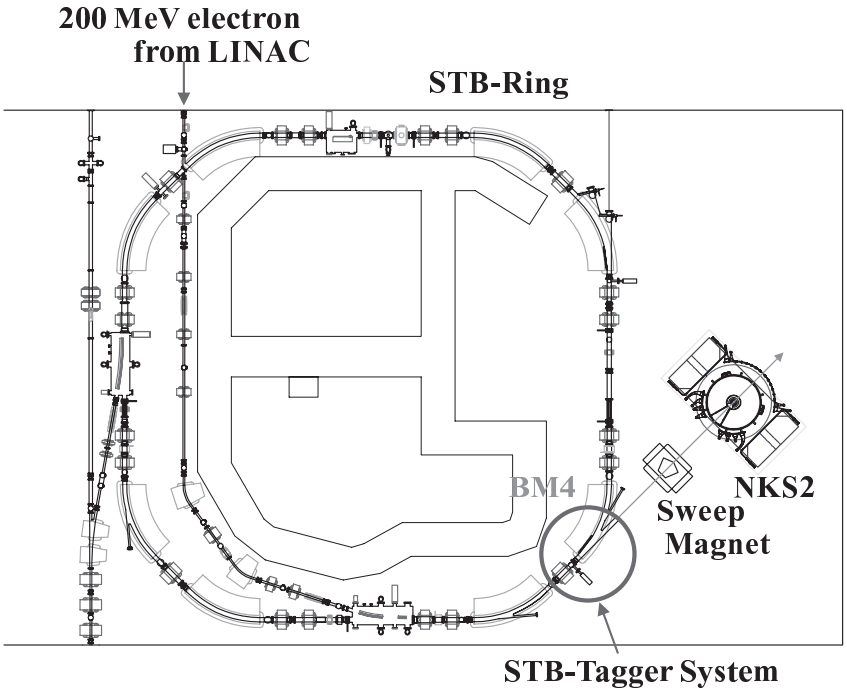

Fig.1. The outline of the second experimental hall of LNS (see text in detail).

has 0.2 GeV of the beam energy and is accelerated up to 1.2 GeV in Stretcher-Booster (STB) Ring. The photon beam is created as bremsstrahlung of electron by a carbon wire at STB Tagger system of Bending Magnet 4 (BM4). There is a dipole magnet which is called the sweep magnet for e^+e^- from photon conversion. The sweep magnet is the same one that was used in the previous experiment NKS.

The spectrometer is placed following the sweep magnet. The main magnet (680 magnet) is a dipole which is renovated from a cyclotron magnet of Cyclotron RI Center of Tohoku University. Detectors of NKS2 are: Inner Hodoscope (IH), Straw Drift Chamber (SDC), Cylindrical Drift Chamber (CDC), Outer Hodoscope (OH), and Electron Veto counter (EV). Detector positions are shown in Fig.2, and 3D views are in Figs. 3 and 4. The detail description of the beam line and the spectrometer will be shown in the following section.

§3. Status of the Experiment

Commissioning runs were carried out in Jan. Mar, Jun., and Sep. 2006. using a carbon target. During those runs, we studied the detector performance, data acquisition system, and trigger rate.

The run of January (17-20) was used to tune the tagging counter and hodoscopes. In the original schedule, the March run (Mar. 7-12) was planned to be used to check the detector system including CDC and hodoscopes. There, however, was an accident of breaking a Mylar window of CDC, therefore this run was used for the trigger study. The CDC was repaired after this beam time and became being ready before the next beam time. In June 6-15, we had two weeks data taking with a natural carbon target. About two third of the beam time was used for the final detector setup: tune of counter gain and

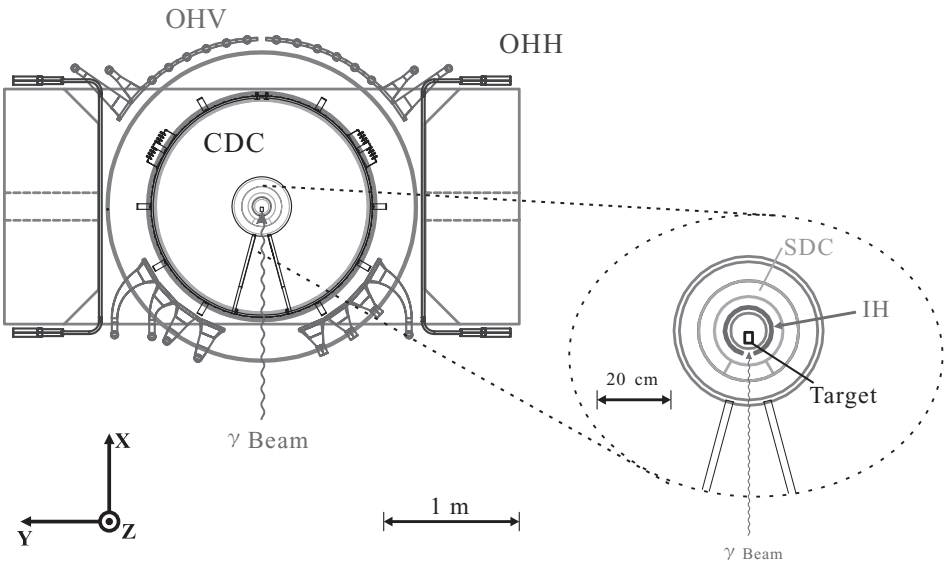

Fig.2. A schematic view of NKS2. The photon beam direction is from bottom to top in the figure. The target holder will be at center of magnet. The detectors are (the order is from center to outer): Inner Hodoscope (IH), Straw Drift Chamber (SDC), Cylindrical Drift Chamber (CDC), Outer Hodoscope (OH, Vertical (OHV) and Horizontal (OHH)), and Electron Veto counter (EV). Note that EV is placed at downstream of OHV but not shown in the figure.

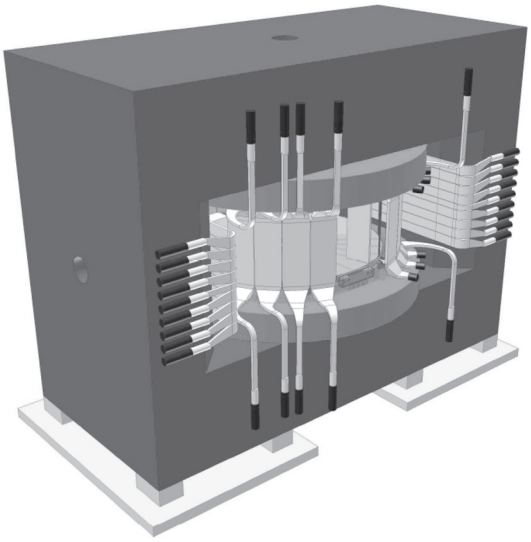

Fig.3. A 3D view of the spectrometer viewed from the upstream of the beam line. We can see a part of OHH on the magnet yoke and OHV around the magnet coil.

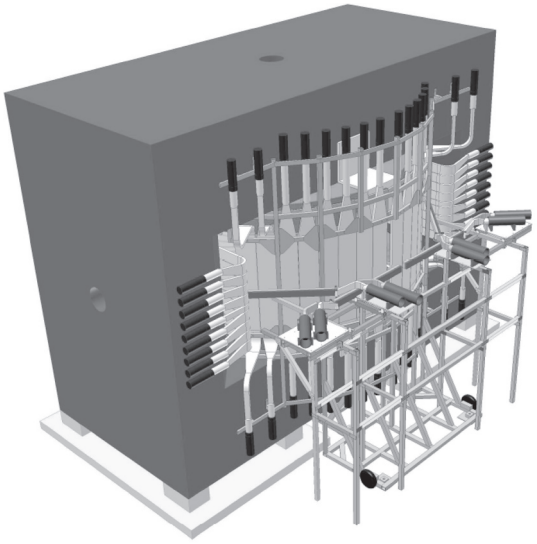

Fig.4. A 3D view of the spectrometer viewed from the downstream of the beam line. There are OHV around the magnet coil and OHH on the magnet yoke. The EV counters are placed following OHV. The OHV and EV counters are supported by aluminum chassis.

threshold of discriminator, noise reduction, fixing some troubles of DAQ, making chambers be ready. Trigger study and data taking were done in the rest of the beam time. The main purpose of the September run (Sep. 25-Oct. 2) was data taking with the carbon target. Additionally, the length of a vacuum pipe between the pair magnet and the target was extended to reject the background from photon conversion. Finally, we started data taking with a liquid deuteron target on November 2.

Construction of a Forward Electro-magnetic Calorimeter SCISSORS Ⅲ

T. Ishikawa, H. Fukasawa, R. Hashimoto, T. Ishida, J. Kasagi, S. Kuwasaki, F. Miyahara, K. Mochizuki, T. Nakabayashi, K. Nawa, Y. Okada, K. Okamura, Y. Onodera, Y. Saitoh, H. Shimizu, K. Suzuki, H. Yamazaki, and H. Yonemura

[1]*Laboratory of Nuclear Science, Tohoku University, Sendai, Miyagi 982-0826*

A new electro-magnetic calorimeter complex FOREST with a solid angle of about 4π in total is under construction. It consists of three calorimeters: a forward one with CsI crystals, a middle one with lead scintillating fiber modules, and a backward one with lead glass Čerenkov counters. Recently, the forward calorimeter SCISSORS Ⅲ takes shape.

§1. An Electro-magnetic Calorimeter Complex FOREST

Nucleon resonances were experimentally studied via π^0 and η photo-production by using an electro-magnetic calorimeter SCISSORS Ⅱ in the GeV-γ experimental hall. The π^0 and η mesons were identified in $\gamma\gamma$ invariant mass distributions. When more than one neutral mesons were produced and each of these decays into $\gamma\gamma$, the possible choice of two γ's is not unique. Thus the events were contaminated in these distributions that two γ's were detected which different neutral mesons decay into and the others were not detected. Since a solid angle of SCISSORS Ⅱ is only 12.6% of 4π, a fraction of these events was large.

To suppress the contamination, a large solid angle calorimeter is required so that a fraction of undetected γ should decrease. A new electro-magnetic calorimeter complex with a solid angle of about 4π in total has been planned [1]. The complex is called Four-pi Omnidirectional Response Extended Spectrometer Trio (FOREST). It consists of three calorimeters: a forward one with CsI crystals 'SCISSORS Ⅲ,' a middle one with lead scintillating fiber modules 'LEPS Backward Gamma,' and a backward one with lead glass Čerenkov counters. Figure 1 a) shows a slant view of FOREST.

The SCISSORS Ⅲ consists of pure CsI crystals which had composed SCISSORS Ⅱ. The shape of CsI crystal modules is a truncated regular hexagonal pyramid. Among these modules, thickness of 144 crystals is 300 mm (LNS type) and that of 48 ones are 250 mm (INS type). Central units of SCISSORS Ⅲ are the LNS type, and peripheral ones are the INS type. Figure 1 b) shows the arrangement of modules in SCISSORS Ⅲ [2,3].

§2. Arrangement of CsI Crystal Modules

Because an equilateral hexagon has an interior angle of 120°, it can be used to tile the plane without holes like a honeycomb. Neither front nor rear faces of a truncated hexagonal pyramid compose

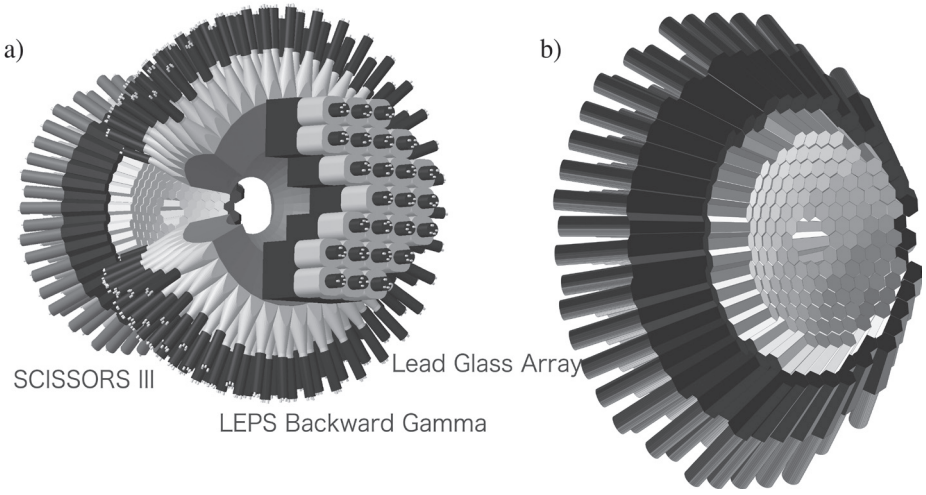

Fig.1. a) Slant view of the new electro-magnetic calorimeter complex FOREST. Polar angles of 4°-27°, 30°-100°, and 106°-170° are covered with CsI crystal array 'SCISSORS Ⅲ,' with lead scintillating fiber module array 'LEPS Backward Gamma,' and with lead glass Čerenkov counter array, respectively. b) Schematic view of the module arrangement in SCISSORS Ⅲ. Central units are the LNS type, and peripheral ones are the INS type.

a segment of a regular solid without overlap. It is required to array truncated regular hexagonal pyramids tight.

Let's consider a crystal is laid out adjacent to the central one. When two crystals are arranged so that the contact side face of the central one is identical with that of the adjacent one as shown in Fig.2(a), the volume of the adjacent one exceeds the angle formed by two vectors to the vertices of the front face of the central one sharing the center of the central one as an endpoint. Hence, another one cannot be laid out similarly adjacent to each of the two without overlap. If the adjacent one is slid rearward so that side faces contact, the adjacent one can be set that does not exceed the allowed region as shown in Fig.2 (b). Numerically, the step of rear LNS type crystal faces should be larger than 4 mm and that of two different type crystal faces should be larger than 40 mm [2].

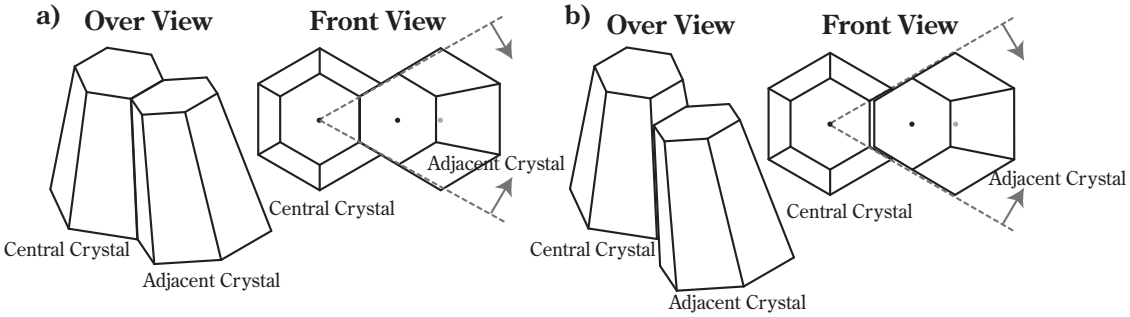

Fig.2. The arrangement of two CsI crystal modules. a) Two crystals are arranged so that the contact side face of the central one is identical with that of the adjacent one. b) The adjacent crystal is slid rearward. In the front view, the volume of the adjacent one should not exceed the angle formed by two vectors to the vertices of the front face of the central one sharing the center of the central one as an endpoint.

§3. Constructed SCISSORS Ⅲ

The crystal arrangement was made from 24th April to 13th May in 2006. Figure 3 shows the constructed SCISSORS Ⅲ. Since individual differences in the module shape exist, crystals are not laid out ideally. The step of rear LNS type crystal faces is about 10 mm at maximum. The front crystal faces cover from 60-460 mm in radius from z-axis. The position and direction of each crystal shall be measured in the near future.

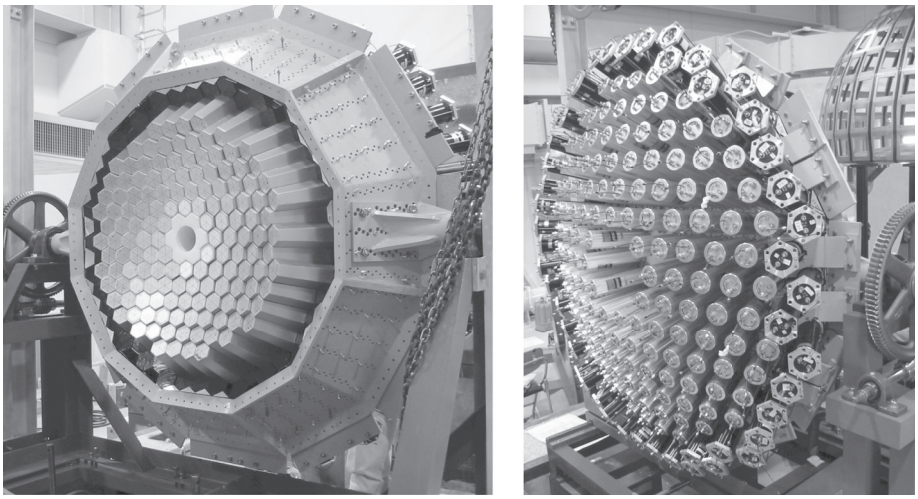

Fig.3. Constructed SCISSORS Ⅲ. The left panel shows a front view, and the right shows a rear one.

References

[1] T. Ishikawa: LNS Experiment #2536 (2005).

[2] T. Ishikawa: Internal GeV- γ analysis note No.37 (2006).

[3] H. Fukasawa: Internal GeV- γ analysis note No.09 (2005).

Installation of a Dipole Electromagnet *R*TAGX

T. Ishikawa[1], R. Hashimoto[1], T. Ishida[1], J. Kasagi[1],
S. Kuwasaki[1], F. Miyahara[1], K. Maeda[2], K. Mochizuki[1],
K. Nawa[1], Y. Okada[1], Y. Onodera[1], H. Shimizu[1], K. Suzuki[1], and H. Yamazaki[1]

[1] *Laboratory of Nuclear Science, Tohoku University, Sendai, Miyagi 982-0826*
[2] *Department of Physics, Tohoku University, Sendai, Miyagi 980-8578*

A dipole electromagnet *R*TAGX has been installed in the GeV-γ experimental hall. It sweeps out charged particles contaminated in the incident γ beam for meson photo-production experiments. It also supplies momentum-analyzed electrons or positrons in a newly constructed test beamline.

§1. *R*TAGX Magnet

A dipole electromagnet *R*TAGX was installed in the GeV-γ experimental hall from 13th to 15th December in 2005. This magnet was originally created as a 1/1.645 scale model for a sector focused cyclotron at Institution of Nuclear Study, University of Tokyo [1]. It had come to be used as a large acceptance spectrometer TAGX [2] for photon induced nuclear and hadron experiments, where the shims and pole tips were removed and the gap was expanded from 210 mm to 600 mm by inserting two iron blocks into vertical return yokes. It was moved to the second experimental hall in 2000 and was used as a Neutral Kaon Spectrometer (NKS). The NKS was replaced by a larger magnet, and it was preserved in a warehouse until SCISSORSII experiments finished.

The magnet was installed in the GeV-γ experimental hall. The inserted two iron blocks were removed and its gap became 210 mm again. We call it Return of the TAGX or Recycled TAGX (*R*TAGX). Figure 1 shows the installed *R*TAGX.

The pole faces are circle with a diameter of 1070 mm, and holes are drilled in the poles and yokes at the center of these with a diameter of 100 mm. The two hollow-conductor pancake-shaped coils are laid out, and the number of turns is 480 in total. It sweeps out charged particles contaminated in the incident γ beam for meson photo-production experiments. It also supplies momentum-analyzed electrons or positrons in a newly constructed test beamline.

§2. Magnetic Flux of *R*TAGX

The magnetic flux of *R*TAGX was calculated by a 3D magnetostatics computer code Radia [3], which is interfaced to Mathematica on Microsoft Windows XP. Figure 2 shows the magnetic flux B_y as a function of z position for the TAGX and *R*TAGX setups with a current of 500 A. The B_y at the center is 0.483 T and 1.183 T, and the $B\ell$ integration is 0.641 Tm and 1.549 Tm for the TAGX and *R*TAGX, respectively. The strong magnetic flux of about 1.2 T at maximum is achieved in the *R*TAGX by

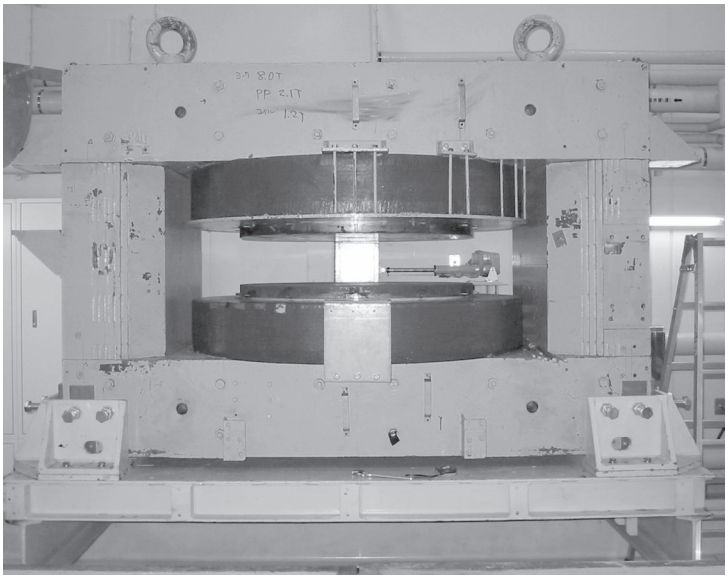

Fig.1. Installed *R*TAGX. The pole faces are circle with a diameter of 1070 mm, and the gap between them is 210 mm.

contracting the gap to 210 mm.

The magnetic fluxes at three points were measured by a calibrated Hall generator with different coil currents. Figure 3 shows the measured magnetic fluxes B_y at three points with various coil currents.

The realistic magnetic flux map was determined by normalizing calculated one for each coil current setup so that it reproduces the measured magnetic flux at the position (0,0,160) where the measured magnetic flux was not influenced by the precise position of the Hall generator.

§3. Electron and Positron Test Beamline

The *R*TAGX can be used to analyze momenta of charged particles with a high resolution since $B_x \simeq 0$ and $B_z \simeq 0$ in the horizontal plane. When the incident γ beam irradiates a target in front of the *R*TAGX, some photons convert into positron and electron pairs. The created positrons and electrons are bent by the magnetic flux, and a monochromatic electron or positron beam can be obtained at a specified angle [4]. Figure 4 shows the analyzed momentum as a function of *R*TAGX current at 30° with respect to z axis.

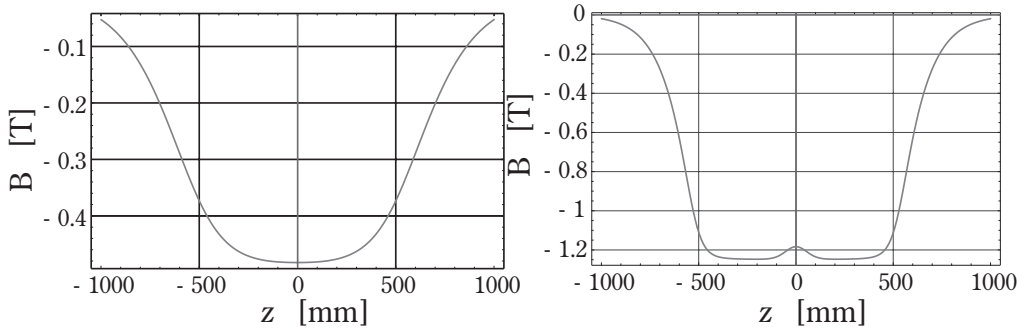

Fig.2. Magnetic flux B_y as a function of z position. The left panel shows that for the TAGX with a gap of 600 mm, and the right shows that for the *R*TAGX with a gap of 210 mm.

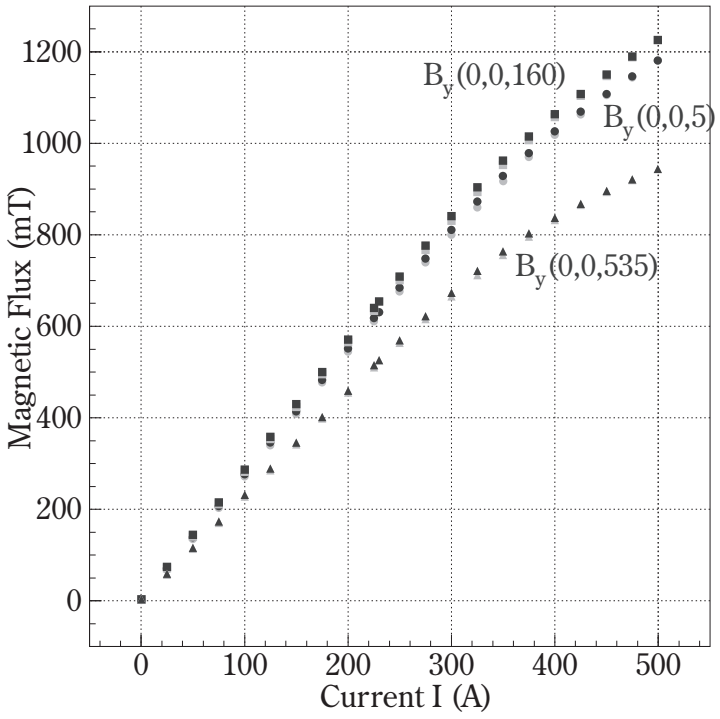

Fig.3. Measured magnetic fluxes B_y at three points with different coil currents. The deep gray circle, rectangle, and triangle markers show those at (0,0,0), at (0,0,160), and at (0,0,535), respectively, where the coil currents are set in the decreasing direction. The light gray circle, rectangle, and triangle ones show those at (0,0,0), at (0,0,160), and at (0,0,535), respectively, where the coil currents are set in the increasing direction.

A Au foil with a thickness of 20 μm is placed 878 mm upstream of the pole center, and a lead collimator with a diameter of 20 mm and with a thickness of 100 mm is laid out 2445 mm downstream at the -30 ° with respect to z axis. The momentum resolution of the obtained beam depends mainly on the energy loss and multiple scattering of the positrons or electrons during penetrating the Au foil and

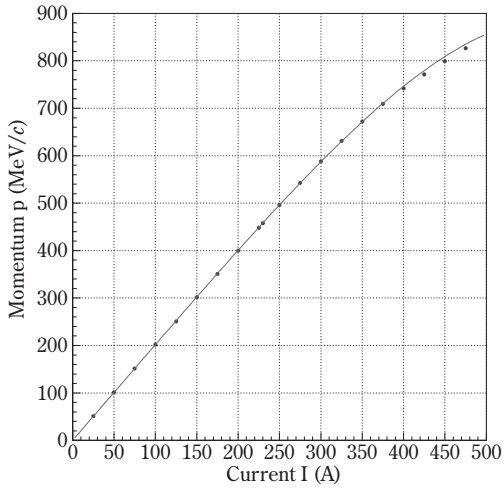

Fig.4. Analyzed momentum as a function of RTGX current at 30 ° with respect to z axis. The data points are compared with $p(I) = 2.0220\,I - 1.7947 \times 10^{-9}\,I^{4.0600}$ Mev/c.

the air on the way. It is roughly 2% although it should be estimated more precisely. The positron and electron beams are obtained with little contamination, and counting rates of these are about 3 kHz independently of the *R*TAGX current with a STB circulating current of 15 mA.

References

[1] T. Tanabe *et al*.: INS internal report INS-J-133 (1972).

[2] K. Maruyama *et al*.: Nucl. Inst. Meth. in Phys. Res. A **376** (1996) 335.

[3] P.Elleaume, O.Chubar, and J.Chavanne: Computing 3D Magnetic Fields from Insertion Devices, Proceedings of PAC97;
O.Chubar, P.Elleaume, and J.Chavanne: A 3D Magnetostatics Computer Code for Insertion Devices, Proceedings of SRI97;
http://www.esrf.fr/Accelerators/Groups/InsertionDevices/Software/Radia/.

[4] H.Shimizu: LNS Experiment #2563.

Ⅱ. Radiochemistry

(LNS Experiment：#2543, #2560)

高純度酸化ガドリニウム試薬中のカリウムの光量子放射化分析

大浦泰嗣，佐々木愛，海老原充

首都大学東京大学院理工学研究科（192-0397　東京都八王子市南大沢1-1）

Photoactivation Analysis of Potassium in High Purity Gadolinium Oxides

Y. Oura, A. Sasaki, and M. Ebihara

Graduate School of Science and Engineering, Tokyo Metropolitan University, 1-1 Minami-Ohsawa, Hachioji, Tokyo 192-0372

A potassium content in high purity gadolinium oxide reagents, which is a component of the detector for the neutrino in the "KASKA" project, was determined by photoactivation analysis. Applying radiochemical processing, 0.1 ppm of upper limit was obtained. The gadolinium oxide reagent determined in this study was confirmed to meet the request for materials in the detector.

§1．はじめに

現在世界的にニュートリノに関する大型研究プロジェクトがいくつか進行あるいは計画されている。その中の一つが，“KASKA”プロジェクトである[1]。このプロジェクトは，原子炉ニュートリノを用いてニュートリノ振動θ_{13}現象の解明を目指している。ニュートリノは物質との相互作用がまれなため，通常，非常に大きな検出器が用いられるが，KASKAでは，ガドリニウム(Gd)原子を含んだ液体シンチレータによるニュートリノの検出を計画している。このシンチレータにウラン系列核種，トリウム系列核種，^{40}K等の天然放射性核種が存在すると，これらのβ壊変によりニュートリノが放出され、原子炉ニュートリノ検出の大きな妨げとなる。従って、シンチレータ中の放射性不純物の特定とその低減は，プロジェクトを成功に導くための非常に重要な課題である。

液体シンチレータにはGdを含む化合物を溶解させるが，その化合物合成のための原料の一つは酸化ガドリニウムである。希土類元素であるこの試薬には，天然アクチノイド元素であるUとTh，ならびに環境中に多量に存在するK（^{40}K）が不純物として混入している恐れがある。これまでに，U濃度とTh濃度は高感度機器分析法の一つであるICP質量分析法により定量した。しかし，ICP質量分析法では，Kの定量は難しい。そこで，放射化分析法により酸化ガドリニウム中のK濃度の定量を行った。

高感度で高確度な定量値を得ることができる放射化分析法は、微量元素に対する有用な定量分析法である。一般に，中性子放射化分析法（NAA）がよく利用されるが，Gdは中性子捕獲断面積が非常に大きいため，照射中の中性子の自己吸収を無視することができず，正確な定量には比較標準試料の調製を注意深く行う必要がある。一方、試料に制動放射線を照射する光量子放射化分析法（PAA）で利用する（γ, n）反応の反

応断面積は標的核種の質量数により系統的に変化し，特定の核種（元素）で共鳴的に大きな断面積を示すことがない。そのため，試料による自己吸収は起こりにくく，本試料においてはNAAよりも正確な定量が可能だと考えられるため，PAAによるKの定量を行った。しかし，Kの定量に用いる^{38}Kの半減期が7.6分と短い点で分析上の制約を受ける。

§2．実　　験

純度99.999%のGd_2O_3約600mgをAl箔に包み，直径10mmの円板状に整形した。また，比較標準試料であるK_2CO_3も同様に調製した。この2種類の試料を交互に石英管につめ，最大エネルギー25 MeVの制動放射線を10分間照射した。

当初は，照射後，非破壊測定による定量を試みたが，^{160}Gd（γ, n）反応で生成した^{159}Gd（半減期18.5時間）の放射能が強く，検出器に近づけて測定できなかったため，Kの上限値しかえられなかった。そこで，次のような化学分離を迅速に行った。照射後，Al箔からGd_2O_3のみ取り出し，あらかじめ既知量のK^+担体（約10mgK）を加え加熱しておいた6M硝酸に溶解した。この溶液にアンモニア水を添加して水酸化ガドリニウムを沈殿させた。遠心分離により分離した上澄み液を，さらに，孔径0.2 μmのフィルターでろ過して，水酸化ガドリニウム沈殿を完全に除去した。この溶液を試薬瓶に移し，Ge半導体検出器にてガンマ線を測定した。K_2CO_3は水に溶解後，Gd_2O_3試料と同様な形状にそろえ，ガンマ線を測定した。Kの化学収率は再放射化法により求めた。測定対象であるK同位体を第１表にまとめた。

第１表　定量にもちいたK同位体の核データ。

核種	半減期	ガンマ線エネルギー	
^{38}K	7.6分	2167keV	^{39}K（γ, n）
^{42}K	12時間	1525keV	^{41}K（n, γ），再放射化法

§3．結果と考察

異なる照射で定量を２回（試料Aと試料B）行った。化学分離は約15分で終了し，化学収率はそれぞれ30%と51%であった。高い化学収率よりも短時間での化学分離を目指したため，水酸化ガドリニウムの精製を行わなかったのが低い化学収率の原因であろう。

第１図に試料Bでの照射終了23分後のガンマ線スペクトルを示す。化学分離操作によりガンマ線測定の妨害となる^{159}Gdはほとんど除去できた。また，^{38}Kが放出するガンマ線のエネルギーは，（γ, n）反応で生成する核種から放出されるガンマ線のエネルギーの中ではもっとも高エネルギーなものの一つであることも幸いし，そのエネルギー領域ではコンプトン散乱によるバックグラウンドがほとんど０の状態で測定を行うことができた。試料Aでも同様であった。

^{38}Kのガンマ線を検出できず，さらにバックグラウンドも０であったので，１カウント検出できた時の濃度を上限値として算出した。試料AとBでそれぞれ，0.6ppmと0.1ppmとなった。試料Bの方が分析条件がよかったので，Gd_2O_3試料中のK濃度は0.1ppm以下と決定した。よって，本研究で分析に供したGd_2O_3試薬はKASKA実験で要求されるK濃度（１ppm）を十分満たしていることが確認できた。

ここでは詳細を省略するが，NAAによる定量も行った。日本原子力研究開発機構JRR4の簡易照射筒にて６時間照射し，放射化学分離後ガンマ線を測定した。上限値として0.9ppmを得た。NAAでは試料の自己吸収により中性子束が見かけ上約1/10になることを別の実験より確認しており，これがPAAの方がNAAよ

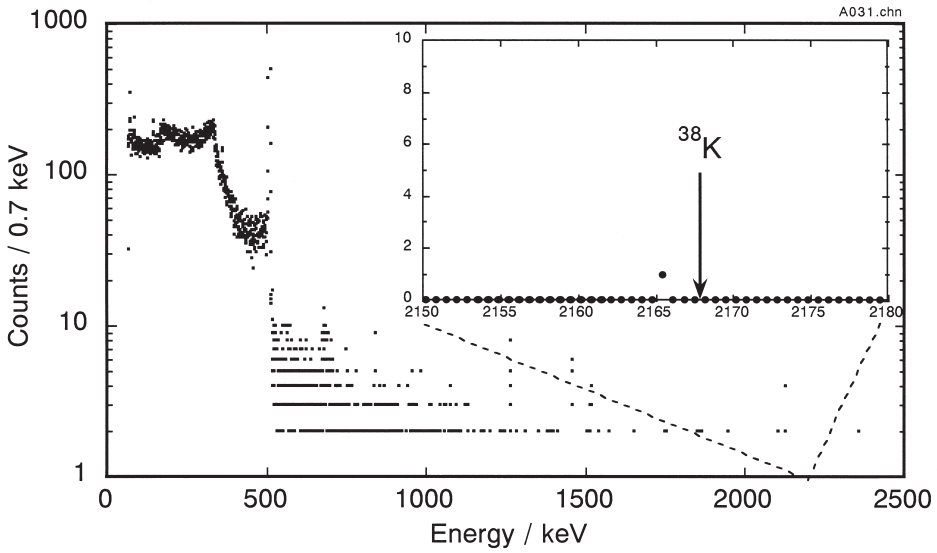

第１図　放射化学分離によるカリウムフラクションのガンマ線スペクトル。照射終了23分後から300秒間測定。

りも低い上限値を得ることができた理由と考えられる。中性子吸収断面積が大きな元素で構成されるマトリックスを持つ試料の場合は，PAAが非常に有効であることを示している。

§4．ま と め

高純度酸化ガドリニウム試薬中のカリウム濃度を光量子放射化分析法により調べた。カリウムの上限値として0.1ppmを得た。KASKAプロジェクトで要求される条件を十分満たしていることを確認できた。

謝　　辞

本研究を行うにあたり良質な電子ビームを供給していただいた東北大学原子核理学研究施設マシングループの方々と試料照射ならびに放射線測定でお世話になった大槻勤助教授と結城秀行博士に深く感謝する。

参　　考　　文　　献

[1]　M. Kuze and the KASKA Collabolation: Nucl. Phys. **B149** (2005) 160.

(LNS Experiment：#2517, #2529, #2545, #2559, #2573)

加熱回収法によるコンクリート試料中放射性炭素分離法の検討

泉雄一[1]，安藤佳明[1]，松村一博[1]，大槻勤[2]，結城秀行[2]，桝本和義[3]

[1]㈱日本環境調査研究所（342-0008　吉川市旭8-3）
[2]東北大学理学部附属原子核理学研究施設（982-0826　仙台市太白区三神峯1-12-1）
[3]高エネルギー加速器研究機構（305-0801　茨城県つくば市大穂1-1）

Separation Methods of Radioactive Carbon from Concrete Samples by Thermal Combustion Methods

Y. Izumi[1], Y. Ando[1], K. Matsumura[1], T. Ohtsuki[2], H. Yuki[2], K. Masumoto[3]

[1]*Japan Environment Research Co., Ltd, Asahi8-3, Ysoshikawa, Saitama, 342-0008*
[2]*Laboratory of Nuclear Science, Tohoku University, Mikamine, Taihaku-ku, Sendai, Miyagi, 982-0826*
[3]*High Energy Accelerator Research Organization, Oho1-1, Tukuba, Ibaraki, 305-0801*

In order to determine the activity of ^{14}C induced in the concrete obtained from various accelerator facilities, we studied the oxidative combustion method for extraction of ^{14}C from concrete samples quantitatively. Separation conditions, such as maximum heating temperature and time were examined using ^{11}C produced by the $^{12}C(\gamma,n)\ ^{11}C$ reaction as a radioactive tracer instead of ^{14}C. Samples were irradiated with 30MeV-bremsstrahlung at Laboratory of Nuclear Science, Tohoku University.

In this study, several types of standard rocks were combusted, because the thermal decomposition of such rocks contained in a concrete might be difficult. After irradiation, samples were heated in an IR-furnace under O_2 stream (flow rate ; 100ml/min). After the decomposition of sample, the gas was sequentially guided to another furnace (catalyst ; CuO, temperature ; 1073K) for oxidation of CO to CO_2. Radioactive carbon dioxide was collected in 2-amino-ethanol solution of an alkali trap.

As a result, the addition of oxidants was effective to improve ^{11}C yields and yields of ^{11}C from standard rock samples were over than 70% heated at 1373K for 20 minutes. It was concluded that the yields of ^{14}C from concrete samples were also more than 70%. In case of steel samples, yields of ^{11}C were about 100%.

It was concluded that the separation by the thermal combustion method was useful to separate radioactive carbon, such as ^{11}C and ^{14}C, from concrete samples.

§1．目　　的

加速器施設の遮蔽体として用いられているコンクリート中には微量ではあるが，加速器から二次的に発生する中性子による放射化によって様々な核種が生成することが知られている。これらのコンクリート中の放

射性核種の濃度を評価する方法を確立しておくことが，施設を廃止する際に発生する廃棄物のクリアランスレベルの検討にとって非常に重要である。筆者らは放射化によってコンクリート中に生成する核種のうち，測定が難しいとされている低エネルギーのβ線のみを放出する核種の放射能測定法を検討してきた。^{3}Hについては濃度を測定する手順について検討し，コンクリート試料を加熱した後，酸化銅を用いた酸化触媒を通して，ドライアイスとエタノールによるコールドトラップで回収する方法を採用し，試料を900℃程度に加熱することによって定量できることを報告した[1]。また，加熱温度と時間を正確に制御できる赤外線加熱炉により，コンクリート試料中のトリチウム濃度を効率的に測定できることを報告した[2]。一方，放射化コンクリート中の^{14}Cの放射能を測定するには^{14}Cの分離法の確立が不可欠であるが，これまで定量例はほとんど無かった[3]。最近，遠藤らは，コンクリート中の^{3}Hと^{14}Cの定量を行った結果を報告した[4]が，２核種を２-アミノエタノールに捕集して液体シンチレーションカウンタで同時に測定している。しかし，この同時測定では，^{3}Hの濃度が高い場合に^{14}Cの計数領域への^{3}Hのテール成分の流れ込みの影響がある可能性があることも想定される。

コンクリート中の^{14}Cの分離定量法を検討する際に，単に^{14}Cを含む溶液をコンクリート中に浸透させるなどして調製した試料を用いたとしても，浸透させた^{14}Cは放射化で生成した^{14}Cと同様の挙動を示す保証はない。親核の存在量や反応断面積を考慮すると，^{14}Cは主に^{14}Nの（n , p）反応によって生成すると予想される。このため，窒素濃度既知のコンクリートを中性子放射化すれば^{14}C濃度既知のコンクリート試料が調整できると考えられるが，窒素は大気中に多量に含まれることから，正確に一定量の窒素を含むコンクリート標準試料の調製は困難である。

炭素の放射性同位体としては^{14}Cの他に^{11}Cがある。そこで，コンクリートから^{14}Cを定量的に回収できたかどうかを評価するかわりに，炭素濃度既知の試料を放射化し，生成した^{11}Cをトレーサーとして用いることにより，放射性炭素の分離挙動を調べることができると考えられる。

すでに，非鉄金属や鉄鋼試料中の微量炭素の光量子放射化分析では，^{11}Cを酸素気流中で加熱分解し炭酸ガスとして分離捕集する方法を利用している[5]ことから，本研究では放射化した試料を用いて，赤外炉による加熱分離法での加熱温度や加熱時間等を変化させ，放射性炭素の分離条件を検討した。なお，ここでは比較的分解しにくいと思われる骨材として使用されている岩石試料を中心に検討することとした。

§２．試験方法

コンクリート試料を加熱し，^{14}Cを二酸化炭素として回収して^{14}C濃度を測定するためには，測定試料を加熱するときの温度，維持時間等の諸条件の設定及び^{14}Cの回収率の評価が必要である。

今回の試験では炭素濃度が既知の試料として地質調査所（現在，（独）産業技術総合研究所）より供給されている岩石試料（JA-１，JB-１a，JG-１a及びJR-１の４種）及び（社）日本鉄鋼連盟より入手した鉄鋼試料（炭素濃度39ppm及び1860ppmの２種）を東北大核理研電子ライナックで30MeVの制動放射線を照射し，^{12}C（γ, n）^{11}C反応により生成させた^{11}Cをトレーサーとして利用した。

2.1　試料の照射

岩石試料及び鉄鋼試料は秤量して高純度アルミ箔に包んだ後，直径約10mmのペレット状に整形した。さらに，試料の前後をCu箔で挟み，さらにアルミ箔で包み込んで照射試料とした。岩石等の試料重量は200mgから300mgとし，照射量補正のための標準物質（$CaCO_3$）は約30mgとした。試料の照射条件は加速エネルギー30MeV，加速電流100μA，パルス幅3μsec，繰り返し数300ppsとし，照射時間は原則とし

て20分とした。

2.2　γ線照射量の補正

照射位置や加速条件の変動による各照射試料の照射線量の補正は，試料の前後に取り付けたCu箔中に生成した^{61}Cuまたは^{64}Cuの放射能をGe検出器により測定して行った。

2.3　加熱回収装置

第１図に加熱回収装置の装置構成を示す。照射した試料から回収した岩石等の試料を秤量した後，石英製のガラスボートに乗せULVAC社製赤外炉により酸素気流中で加熱した。赤外炉による試料の加熱パターンの例を第２図に示す。このときの酸素流量は100ml／分である。試料は加熱開始後５分間で1000℃に，その後５分間で最大温度である1100℃に達するように設定した。最大温度保持時間を５分間とし，加熱開始後15分後に加熱を終了し，20分経過するまで回収した。

炭素の酸化を完全にするため，赤外炉の後段には800℃に設定した酸化銅を用いた酸化触媒用電気炉を接続し，ドライアイス・アルコールを用いたコールドトラップの後に，２-アミノエタノールによる^{11}C回収用のアルカリトラップを接続した。

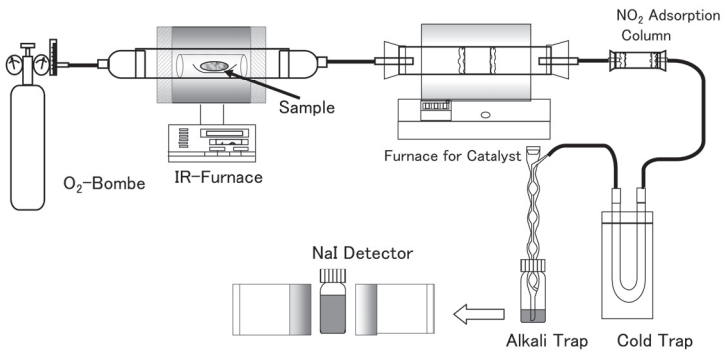

第１図　Apparatus for Heating Samples by IR-Furnace.

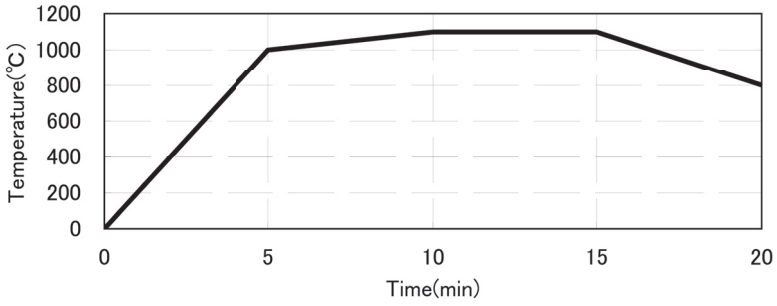

第２図　Heating Pattern of Samples by IR-Furnace.

2.4　酸化剤の添加

照射した試料の分解・酸化を促進するために，四三酸化鉛と酸化硼素の１：１混合物を１ｇまたはLECO社製Sn系の酸化剤を２ｇ添加した。

2.5　^{13}Nの分離

試料の照射によって^{11}Cと同時に生成する陽電子放出核種として半減期10分の^{13}Nがある。試料を加熱した際に，^{13}Nが窒素酸化物になると，炭酸ガスと同時に捕集されることになる。この両者を分離するには半減期の違いを用いることも可能であるが，ここでは，^{13}Nは酸化コバルトをシリカゲル中に分散させた吸着剤（以下，酸化コバルト－シリカゲル）を入れたカラムをアルカリトラップの前に挿入して捕集することにした。酸化コバルト－シリカゲルは硝酸コバルト飽和水溶液とオルトケイ酸エチルをかくはん，混合しゲル化させた後，電子レンジで加熱し，加水分解の結果生成したエタノールおよび水を蒸発させ，さらに電気炉中400℃で２時間乾燥したものを用いた。

2.6　^{11}Ｃ測定方法及び^{11}Ｃ回収率

２-アミノエタノール２mlを用いたアルカリトラップに回収した^{11}CはBGO検出器を用いた同時計数回路を用いて測定し，加熱終了後５分間計数率が上昇せず回収が終了したことを確認した。

回収が終了したアルカリトラップ中の２-アミノエタノールはメタノール16mlを用いてトラップ管を洗浄して回収した。洗浄液を含めて全量をバイアルに回収し，NaI（Tl）検出器を用いて同時計数率の時系列変化を測定した。得られた計数率は全て照射終了時点に減衰補正した。

^{11}C生成効率は標準物質として$CaCO_3$を照射したときの^{11}C生成量を基準として求めた。これにより求めた照射試料に生成した^{11}C量から岩石試料等の炭素濃度を算出し，各岩石試料等の標準炭素濃度と比較することにより，加熱回収法による^{11}C回収率を求めた。

§３．試験結果

3.1　酸化剤による分解

コンクリート試料に酸化剤を添加したときの^{11}Cの回収率を第１表に示す。これにより，酸化剤を添加しない場合は60％程度の回収率であったが，酸化剤特にSn系酸化剤を添加することにより^{11}Cの回収率が向上することが確認された。以下の測定では全てSn系酸化剤を用いた。

第１表　Effect of Oxdants Addition to ^{11}C Yields.

Sample	Oxidants	Yield of carbon (%)
JA-1	No Addition	57.8
	$Pb_3O_4 + B_2O_3$	71.9
	Sn Oxidants	111.6
JB-1a	No Addition	60.7
	$Pb_3O_4 + B_2O_3$	63.3
	Sn Oxidants	73.7

3.2　^{13}N の分離

第３図に^{11}Cを回収したアルカリトラップ試料と^{13}Nを吸着させたカラムから取り出した酸化コバルト－シリカゲルのNaI (Tl) 検出器による計数率の時間変化を示す。これにより，アルカリトラップ試料では半

減期20.4分のみの減衰が，酸化コバルトーシリカゲル試料では半減期9.97分のみの減衰が確認された。これにより，酸化コバルトーシリカゲルにより^{13}Nが回収されており，^{11}Cの測定に^{13}Nの影響を排除できることが分かった。

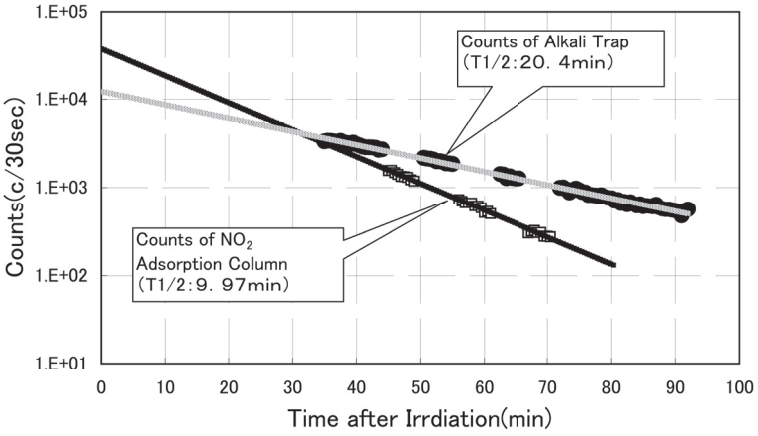

第 3 図　Separation of ^{13}N and ^{11}C by Adsorption Column.

3.3　アルカリトラップ段数

^{11}Cを回収するときに必要なアルカリトラップ段数を確認するため，複数のトラップを取り付けたときの回収率を求めた。この結果，2段目以降のアルカリトラップの計数率は，1段目に比較して1/1000以下であった。よって，アルカリトラップは1段で十分回収できることが分かった。なお，斉藤らは炭素量として約40mg程度までアルカリトラップによりほぼ定量的に回収できることを報告している[5]。これに対し，今回加熱回収した試料の炭素量は最大でも鉄鋼試料の0.6mgであり，十分低い炭素量となっている。

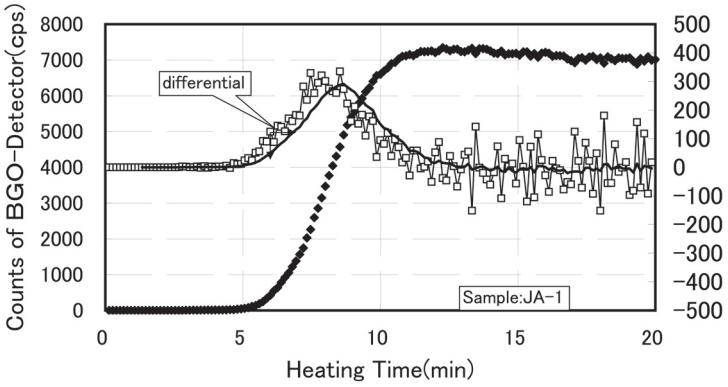

第 4 図　Counts of ^{11}C by BGO-Detector.

3.4　岩石試料等の^{11}C回収率

第４図に加熱経過時間とBGO検出器の計数率変化の例を岩石試料JA-１について示す。加熱開始後ほぼ５分経過した時点から計数率が上昇したのち，８分前後で急激に上昇し，約12分後に計数率の上昇は終了する。

加熱する試料の位置が加熱用ガラス管（内径30mm，長さ500mm）の中央にあるとし，試料からアルカ

リトラップまでの回収経路の体積を求めると約440cm^{3}である。^{11}Cが酸素供給でのみ移動すると仮定すれば，^{11}Cが試料から放出されてからアルカリトラップに到達するまでに約4分必要である。よって，最も^{11}Cが放出される温度は第２図に示す加熱パターンから赤外炉の設定温度は800℃前後と推定される。ただし，実際の試料温度は酸化剤の添加によりさらに高い温度となっている可能性がある。また，第４図に示した計数率の変化量によれば加熱開始後20分経過すれば^{11}Cは十分回収できているものと考えてよい。

第２表に各種の試料を用いて得られた^{11}Cの回収率を示す。この結果，炭素濃度が70.8ppmから312ppmの範囲の岩石試料では試料によって多少異なるものの^{11}Cの回収率はほぼ70％以上であった。また，鉄鋼試料ではほぼ定量的に回収できることが分かった。

第２表　Yields of Carbon.

Sample	Carbon Concentrations (ppm)	Maesured (ppm)	Yields of carbon (%)
JA-1	271.0	196.7	72.6
JB-1a	312.0	233.3	74.8
JG-1a	295.0	257.3	87.2
JR-1	70.8	51.7	73.0
Carbon Steel-1	39.0	42.7	109.5
Carbon Steel-2	1860.0	1822.4	98.0

前述のようにNaI（Tl）検出器による^{13}N吸着カラムの測定結果では^{11}Cは確認されなかった。また，標準物質を乗せた石英ガラスボートでも^{11}Cが残存していないことを確認した。しかし，岩石試料を加熱した石英ガラスボートの測定結果では計数率が高いものの，種々の核種が生成しているため，半減期を考慮した^{11}C成分の分離によってその残存量を定量することは困難であった。岩石試料で^{11}Cの回収率が低い理由は明らかではないが，加熱後の試料に残存している可能性もあると推定される。

以上のように岩石試料で若干回収率が低かったものの，今回用いた赤外炉による放射性炭素の加熱回収法では安全管理上は十分な回収率が得られた。

コンクリート中または空気中の窒素が中性子照射されることにより生成する^{14}CはCO_2を経由してコンクリート中に含まれると仮定すると，コンクリートの中性化により生じる$CaCO_3$は骨材としての岩石より熱分解が容易であることから，実際のコンクリート試料ではさらに回収率が高くなると思われる。

§4．ま と め

コンクリート試料中の^{14}C濃度評価のモデルとして，^{12}C（γ, n）により生成させた^{11}Cを用い，鉄鋼試料及びコンクリート組成のうち加熱分解しにくいと思われる骨材用の岩石試料について加熱回収法による回収率を求めた。この結果，最大加熱温度1100℃，加熱時間合計20分で70％以上の回収率が得られた。よって，^{14}Cについても岩石試料ではほぼ同様の回収率が得られるものと考えられる。実際のコンクリートでは骨材である岩石以外に，熱分解の容易な$CaCO_3$の成分があるため，^{14}Cの回収率はさらに高いものと考えてよい。

以上から，コンクリート試料中の放射性炭素濃度測定には加熱回収法による分離回収が有効であることが分かった。

参　考　文　献

[1] 泉雄一，松村一博，草野正彦: KEK Proceedings **2001-14** (2001) 53.

[2] Q. Wang, K. Masumoto, K. Bessho, H. Matsumura, T. Miura: J. Radioanal. Nucl. Chem. (2004) 262.

[3] 桝本和義，大槻勤，笠木治郎太，泉雄一，大和一朗: 保健物理，**34** (1999) 151.

[4] A. Endo, Y. Harada, K. Kawasaki, M. Kikuchi: Int. J. Appl. Radiat. and Isotopes **60** (2004) 955.

[5] K. Masumoto, K. Shikano, T. Ohtsuki, Y. Itoh: Anal. Sci. **17** (suppl.) (2001) 641.

[6] 斉藤智雄他: Radioisotopes **25** (1976) 36.

Ⅲ. Accelerator, Synchrotron Radiation, and Instrumentation

(LNS Experiment : #2537, #2553)

Properties of the Coherent Radiation Emitted from Photonic Crystal in the Millimeter Wave Region. Ⅰ

Y. Shibata[1], K. Ishi[1], T. Tsutaya[1], N. Horiuchi[2], Y. Segawa[2], Y. Kondo[3], H. Miyazaki[3], F. Hinode[4], T. Ochiai[5], and K. Ohtaka[6]

[1]*Institute of Multidisciplinary Research for Advanced Materials, Tohoku University, Katahira, Sendai 980-8577*
[2]*Photodynamics Research Center, The Institute of Physical and Chemical Research (RIKEN), Sendai 980-0845*
[3]*Graduate School of Engineering, Tohoku University, Aramaki, Sendai 980-8579*
[4]*Laboratory of Nuclear Science, Tohoku University, Mikamine, Sendai 982-0826*
[5]*Nanomaterials Laboratory, National Institute for Materials Science (NIMS), Tsukuba 305-0044*
[6]*Center for Frontier Science, Chiba University, Chiba 263-8522*

Using a short-bunched beam of electrons of a linear accelerator, sharp directionality of the coherent radiation emitted from a photonic crystal (PhC) was observed in the millimeter wave region. When the PhC was rotated around an axis perpendicular to the surface of the PhC, the radiation intensity decreased drastically. On the other hand, the dispersion relation of the radiation changed little with the rotation. The decrease of the intensity was conspicuous in the high frequency region, in comparison with that of the low frequency region.

§1. Introduction

When a short-bunched beam of electrons from a linear accelerator passes by near the surface of a photonic crystal (PhC), coherent radiation is emitted in the millimeter wavelength region [1]. In this paper we call it the photonic crystal radiation. The origin of the photonic crystal radiation is considered in essence to be the same as that of Smith-Purcell radiation (SPR), which was emitted from the electron passing by a metallic grating [2]. Contrary to the many researches on SPR, the experimental study on the photonic crystal radiation has been limited, and its optical properties have been not well studied. For example, the photonic crystal radiation is considered to satisfy the dispersion relation of SPR; the relation bases on a kinetic relation between the period of the radiation source, the frequency of the radiation and the velocity of the electron. In our experiment using an S-band linear accelerator, however, the observed dispersion relation of the photonic crystal radiation was composed of two groups: the one satisfied the dispersion relation of SPR and the other obeyed another relation clearly different from the SPR relation [1, 3]. The unexpected dispersion relation has excited a controversy over its origin.

To elucidate the properties of photonic crystal radiation, here, we report an experiment in which

PhC was rotated around an vertical axis. The experiment showed sharp directionality of the photonic crystal radiation.

§2. Brief Summary of Photonic Crystal Radiation

Let us summarize the mechanism of the photonic crystal radiation briefly [4, 5]. We used the coordinate system shown in Fig. 1, and let an electron move with constant velocity υ along the x axis. We take the coulomb field of the moving electron as a source of virtual radiation. The Fourier component of the radiation ω has a wave vector $(k_x, k_y, \pm\Gamma)$, with the x component given by $k_x = \omega / \upsilon$ and the y component k_y is arbitrary. By energy conservation, $\Gamma = \sqrt{(\omega / c)^2 - k_x^2 - k_y^2}$. Since $\upsilon < c$, Γ is pure imaginary, meaning that the radiation is evanescent and decays with constant $|\Gamma|$ with distance from the trajectory of the electron. In other words, the line $\omega = \upsilon k_x$, called the υ line, lies outside the light line $\omega = ck_x$.

When the evanescent wave reaches to a PhC, the photonic crystal radiation is emitted through the electromagnetic interaction between the incident radiation and the PhC. When we observe far-field radiation within the xz plane, k_y can be set to zero. The PhC having a period g in the x direction then produces the photonic crystal radiation by giving a Umklapp change of the integer multiple of $2\pi/g$ to the x component of the wave vector of incident light. Using the same symbol k_x to represent the x component of the photonic crystal radiation, we may say that the incident radiation on the υ line is Umklapp-shifted to the new υ lines of dispersion $\omega = \upsilon(k_x + n(2\pi/g))$, n being an arbitrary integer. We shall call these lines υ_n lines. The light on the υ_n line thus has the z component of the wave vector given by

$$\Gamma_n = \sqrt{\left(\frac{\omega}{c}\right)^2 - \left(\frac{\omega}{\upsilon}\right)^2 - n\left(\frac{2\pi}{g}\right)^2}. \tag{1}$$

It reaches a far-field observation point as the photonic crystal radiation when this Γ_n is real, *i.e.,* when the frequency ω of the radiation on the υ_n line is inside the light cone. This can always happen for a υ_n line with positive n.

In the PhC, photonic band modes have their band structure in (k_x, ω) space. When υ_n line crosses a photonic band dispersion curve, corresponding peaks appear in the spectrum of photonic crystal radiation [1, 4, 5]. The photonic crystal radiation hence is considered to be distributed along the υ_n lines in the (k_x, ω) diagram.

The υ_n line is equivalent to the dispersion relation of SPR given by

$$n\lambda = g\left(\frac{\omega}{\upsilon} - \cos\theta\right), \tag{2}$$

where λ stands for wavelength and θ for emission angle of the photonic crystal radiation.

§3. Experiment

The experimental setup is schematically shown in Fig.1. A short-bunched beam of electrons of a

linear accelerator of Laboratory of Nuclear Science (LNS), Tohoku University moved with constant velocity υ along the x axis above a PhC. The radiation emitted from the PhC was observed in the xz plane, and the emission angle θ was measured from the x direction.

The photonic crystal radiation was guided to a Martin-Puplett type Fourier-transform spectrometer and was detected with a low-temperature InSb detector. The resolution of the spectrometer was 0.125 cm^{-1} or 3.75 GHz. The plane mirror M1 was controlled with a stepping motor to cover the emission angle θ between 60° and 120°, keeping the optical axis unaltered. The acceptance angle of the measuring system depended a little on the angle θ and was $\pm 0.75^\circ$ in the xy plane and $\pm 1.2^\circ$ in the yz plane at $\theta = 90^\circ$. The impact parameter or the distance between the electron beam and the surface of the PhC was set to be 10 mm.

The beam condition was as followings. The energy of the electron was 150 MeV and its spread was less than 2.5 %, the macro and micro pulse widths were 1.5 μs and 0.67 ps, respectively. The repetition of the macro pulse was 50/3 Hz and the average beam current was 0.8 μA. The cross section of the beam was nearly circular and about 10 mm in diameter.

As the PhC we prepared two samples: a monolayer of spheres of polytetrafluoroethylene (PTFE) and that of cylinders of PTFE (see Fig.1 (b)). Every sphere was 3 mm in diameter, and 419 spheres were arrayed to a triangular lattice on a plane parallel to the xz plane; the size of the monolayer was about 48 mm × 71 mm in the $y \times x$ direction. The reciprocal lattice space of the triangular lattice is shown in Fig. 1 (b) of [1]. In the case of the cylinder, every cylinder had the size of ϕ 3 mm × 80 mm in diameter × length and was placed so that the cylinder axis was parallel to the y direction; the PhC was periodic in the x direction and the number of cylinders was 27.

The PhC was controlled with a stepping motor to rotate around the vertical axis (parallel to the z axis) at the geometric center of the monolayer. The rotation angle ϕ was measured counter-clockwise from the x direction.

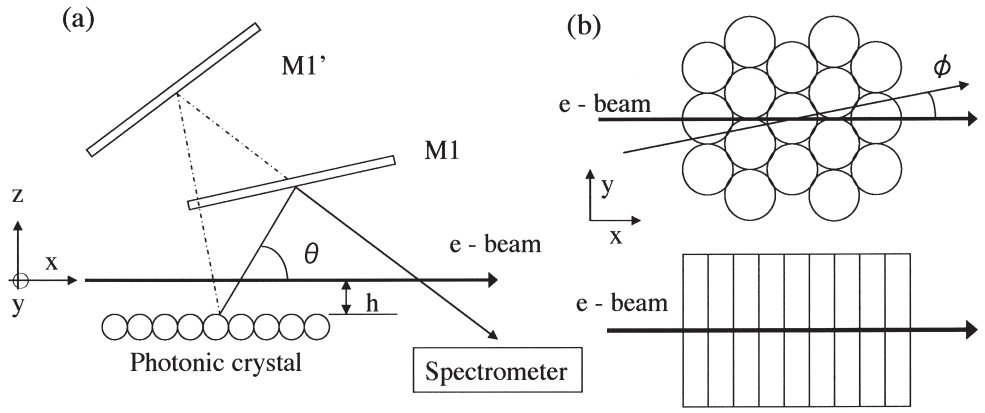

Fig.1. Schematic layout of the experiment (a) and of the drawing of the photonic crystals used (b). The electron orbit was shown by the thick solid line. The emission angle θ and the rotation angle ϕ of the PhC were measured from the x direction.

§4. Results and Discussion

4.1 Triangular lattice of PTFE spheres

At first to check the measuring system, we observed emission spectra of the photonic crystal radiation from the monolayer of the PTFE spheres by varying the rotation angle ϕ. Figure 2 shows the spectra observed at $\phi = 0^\circ$, $\pm 1^\circ$ and $\pm 3^\circ$, on the condition of the emission angle $\theta = 90^\circ$. Eevery spectrum was composed of several peaks, and its structure was nearly symmetric with respect to $\phi = 0^\circ$. The radiation intensity varied drastically with the rotation angle ϕ.

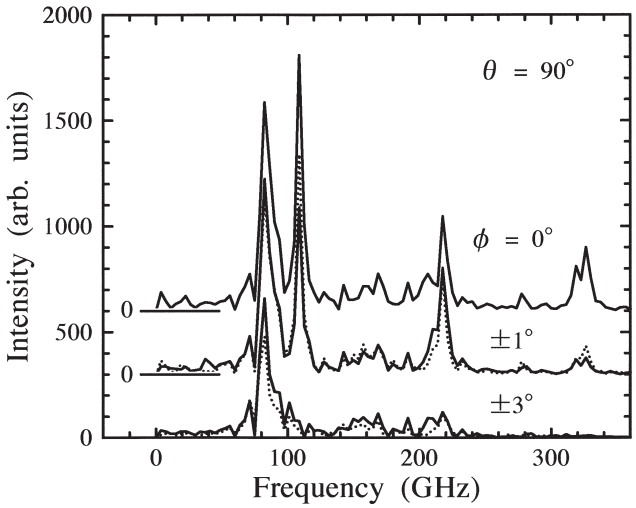

Fig.2. The spectra of the PTFE spheres observed with the rotation angle $\phi = 0^\circ$, $\pm 1^\circ$ and $\pm 3^\circ$ for the emission angle $\theta = 90^\circ$. The dotted curves show the spectra with the negative ϕ. The spectra at $\phi = 0^\circ$ and $\pm 1^\circ$ were shifted vertically to make the comparison clear.

Next the rotation angle ϕ was set to 0°, and the emission spectra were measured with the spectrometer, by controlling θ from 70° to 110° by 1° step. From the spectrum, using the relation $k_x = (\omega/c)\cos\theta$, we obtained the contour map of the intensity of the photonic crystal radiation in the (k_x, ω) space. The result is shown in Fig.3; the abscissa stands for the normalized wave vector $K_x = k_x g / (2\pi)$ and the ordinate for the frequency of photonic crystal radiation $\nu = \omega/(2\pi)$ in GHz. In Fig.3, using the relation $k = \omega / c = 2\pi / \lambda$ and $v = c\beta$, the dispersion relation of Eq. (2) is expressed by the following straight line;

$$\nu = \frac{c\beta}{g}(K_x + n). \qquad (3)$$

Since the energy of the electron was 150 MeV, the relativistic factor $\gamma = 297$ and $\beta = v/c = 0.999994$. We can safely put $\beta = 1$, and hence the dispersion line v_n is parallel to the light line in the (k_x, ω) diagram. The intensity map clearly showed two series of dispersion relation. One is the dispersion relation of SPR shown by the solid lines. The other is the unexpected one shown by the broken lines, whose gradient is 78 % of the solid line. We call hereafter its relation the secondary dispersion relation. The origin of the secondary relation has been clarified by Horiuchi *et al*. [3]. In both relations, the fundamental and the second higher harmonic relations were clearly seen in the figure.

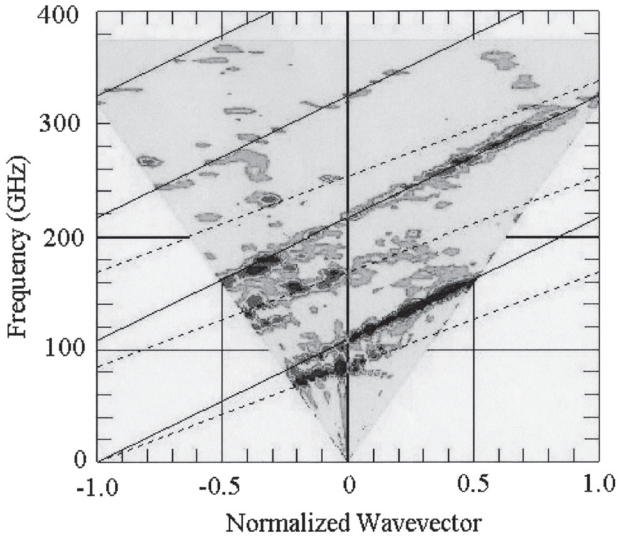

Fig.3. The contour map of the photonic crystal radiation from the PTFE spheres in the (k_x, ω) plane observed with the rotation angle $\phi = 0^\circ$. The x and y axes are the normalized wave vector K_x and the frequency of the radiation, respectively. The solid lines show the υ_1, υ_2, υ_3 and υ_4 lines from bottom to upward.

Using the period of the PhC of $g = \sqrt{3}\, d / 2$, we calculated the theoretical dispersion relation of SPR, *i.e,* the υ_n line,

$$\nu = \frac{c}{g}(K_x + n), \tag{4}$$

where ν is frequency, K_x is the normalized wave vector and n is integer, *i.e,* the order of the relation. However, the calculated relation with the diameter of the PTFE sphere d of 3.0 mm deviated a little from the experimental intensity map. To fit the experiment, we adopted the value d = 3.2 mm. The calculated relation is shown in the figure by the solid lines. The precision of the diameter of the PTFE sphere was better than 0.01 mm, and the reason of the deviation is not clear at present. In the figure, the broken lines show the eye-fitted mean of the secondary dispersion relation expressed by

$$\nu = \alpha \frac{c}{g}(K_x + n), \tag{5}$$

with d = 3.2 mm and α = 0.78. We call these lines the u_n lines.

On the υ_1 line, the distribution of the radiation intensity was plotted as a function of frequency by the solid curve in Fig.4, where the broken curve shows the distribution of the intensity along the u_1 line. Along each of these dispersion relations, the radiation intensity varied rapidly with frequency.

The emission spectra were also measured at the rotation angles $\phi = 2^\circ$, 4° and 8°, and Fig.5 shows the (k_x, ω) maps at $\phi = 2^\circ$ and 4°. In the figure the solid lines show the υ_n lines calculated on the condition of d = 3.2 mm and the gradient of the broken lines was 78 % of the υ_n line. At $\phi = 8^\circ$ the photonic crystal radiation was very weak and near to the noise level of the measuring system, so the

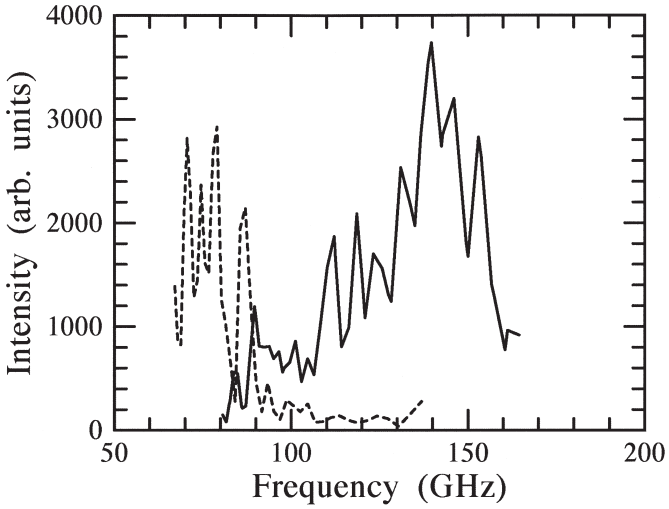

Fig.4. The spectral distribution along the dispersion relation of the first order. The solid and broken curves show the distribution following the SPR relation and the secondary one, respectively.

intensity map was not shown.

The comparison of Figs.3 and 5 shows the followings. The photonic crystal radiation was very sensitive to the rotation angle ϕ. The radiation intensity decreased drastically with $|\phi|$, and the decrease was conspicuous in the high frequency region. Though the intensity change was drastically, both the dispersion relations suffered little influence from the rotation.

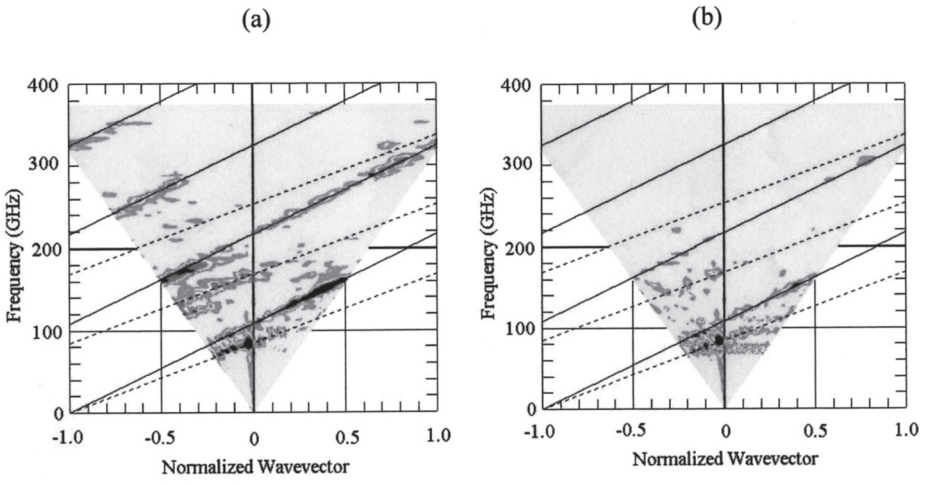

Fig.5. The contour maps of the photonic crystal radiation from the PTFE spheres in the (k_x, ω) plane at $\phi = 2^\circ$ (a) and $\phi = 4^\circ$ (b). The abscissa and ordinate show the normalized wave vector K_x and frequency of the radiation. The solid and broken lines show the υ_n and u_n lines, respectively.

4.2 1D-lattice of PTFE cylinder

After the experiment on the PTFE spheres, photonic crystal radiation of the monolayer of the PTFE cylinders was observed. However, the observed range of the emission angle θ was limited, because of lack of the experimental time.

Figure 6 shows the observed spectra at $\phi = 0^\circ$, $\pm 2^\circ$ and $\pm 4^\circ$ for the emission angle $\theta = 105^\circ$. The structure of the spectra resembled that of the PTFE spheres; the structure was symmetric with respect to the rotation angle $\phi = 0^\circ$. Figure 7 shows the spectra at $\phi = 0^\circ$ and 2° with $\theta = 78^\circ$. The radiation intensity decreased drastically with $|\phi|$, too.

The (k_x, ω) map was also derived from the observed spectra at the rotation angles $\phi = 0^\circ$, 1°, 2° and 4° as shown in Figs.8(a), (b), (c) and (d), respectively. In the experiment, however, the observed

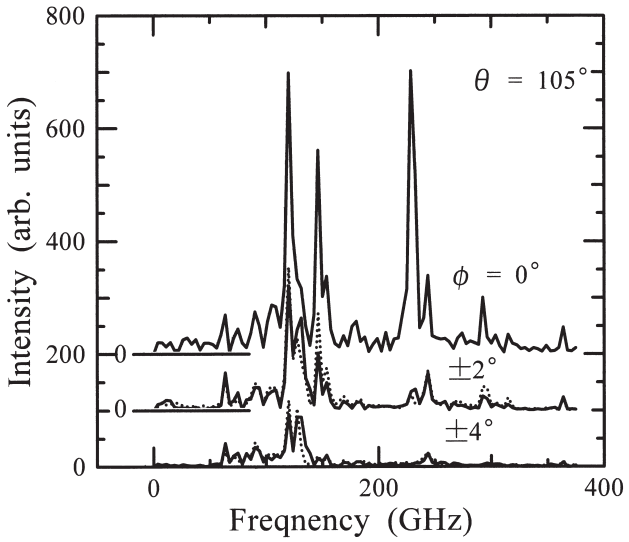

Fig.6. The spectra of the PTFE cylinders observed at the rotation angles $\phi = 0^\circ$, $\pm 2^\circ$ and $\pm 4^\circ$ for the emission angle $\theta = 105^\circ$. The dotted curves show the spectra with the negative ϕ.

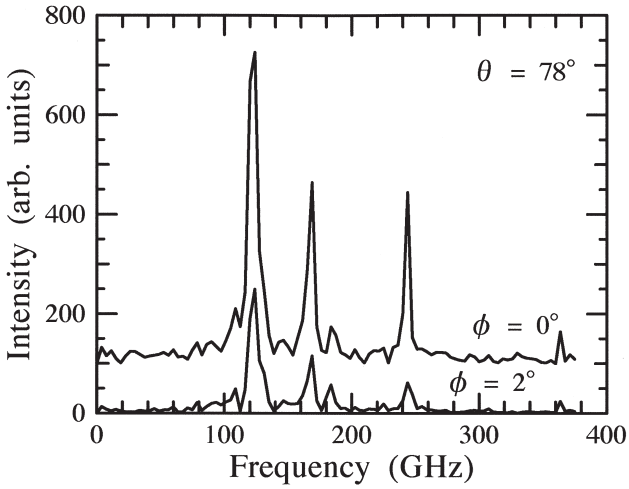

Fig.7. The spectra of the PTFE cylinders observed at the rotation angles $\phi = 0^\circ$ and 2° for $\theta = 78^\circ$.

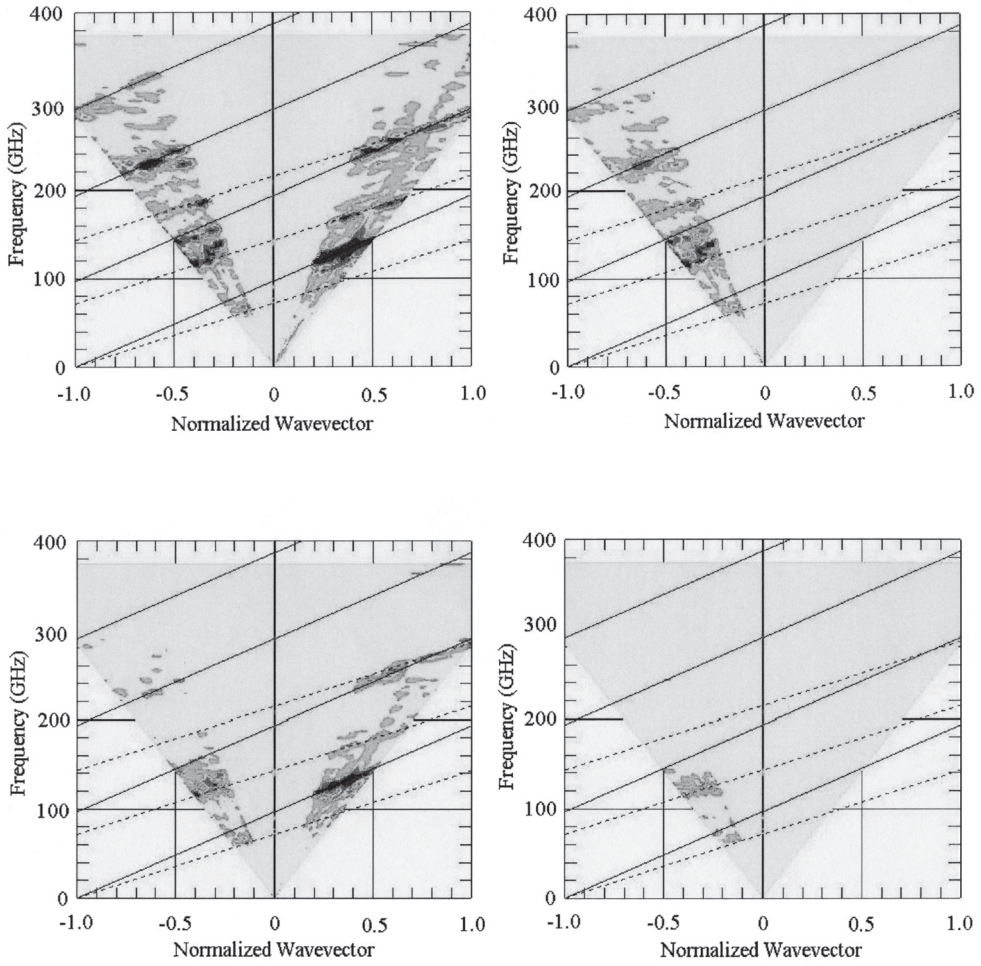

Fig.8. The contour maps of the photonic crystal radiation from the PTFE cylinders in the (k_x, ω) plane at $\phi = 0^\circ$ (a), 1° (b), 2° (c) and 4° (d). In each diagram, only the limited range of θ was observed. The abscissa is the normalized wave vector and ordinate is frequency of the radiation. The solid and broken lines show the υ_n and u_n lines, respectively, calculated on the condition of $g = 3.1$ mm.

range of θ was limited between 110° and 100° and/or between 80° and 70°. In these figures, the solid lines stand for the υ_n lines, calculated using the period of $g = 3.1$ mm. Since the precision of the diameter of the PTFE cylinder was much better than 0.1 mm, the reason of the difference between the diameter (3.0 mm) and the period (3.1 mm) is not clear. The difference may be partly caused from small errors in the straightness of the cylinder.

Though the measurement was limited to the narrow ranges of θ, the intensity map had the similar characteristics to that of the PTFE spheres. The photonic crystal radiation had two series of the dispersion relation; one is that of SPR corresponding to the solid lines and the other is a series of the secondary dispersion relation, corresponding to the broken lines whose gradient was 74 % of the υ_n line. The gradient was roughly equal to that of the PTFE spheres.

The radiation intensity decreased drastically with the rotation angle $|\phi|$ and the decrease was conspicuous in the high frequency region. Though the intensity decrease was drastic, it seemed that both the gradient of the υ_n and u_n lines suffered no influence from the rotation.

4.3 Simple discussion on dispersion relation

Here we simply consider the phase relation of the photonic crystal radiation emitted from neighboring two unit crystals of a PhC on the basis of Huygens' principle. Let an electron move with the constant velocity $\upsilon = c\,\beta$ along the x axis and the period of the PhC be g. Let's suppose that the Coulomb field of the moving electron or the evanescent wave excites radiation in every unit crystal and that at an observation point the superposition of the radiation from neighboring unit crystals should satisfy the constructive interference condition,

$$n\lambda = c\,\Delta t - g\cos\theta\,, \tag{6}$$

where λ is the wavelength of the radiation and $\Delta t = g / c\,\beta$ is the time interval of the electron to move the period of PhC. The dispersion relation of SPR, Eq.(2), is directly derived from the condition. The dispersion relation is caused from the kinetic relation of phase matching among the period, electron velocity, emission angle and wavelength of radiation. The relation is irrelevant to the dielectric constant of constituent of the PhC.

Next, let's suppose that part of radiation (say radiation "a") excited by the electron propagates to the downstream neighboring unit crystal and generates new radiation (radiation "b") which is emitted into free space. From the superposition of radiation "a", directly emitted into free space, and radiation "b", we can derive the similar interference condition,

$$n\lambda = c\,\delta t - g\cos\theta\,, \tag{7}$$

where δt is propagation time of radiation to the neighboring unit crystal. Using the effective dielectric constant ε of the PhC, we assume $\delta t = g\sqrt{\varepsilon}/c$. Then the condition becomes

$$n\lambda = g\,(\sqrt{\varepsilon} - \cos\theta\,). \tag{8}$$

In the (k_x, ω) diagram, the condition is expressed as

$$\nu = \frac{c}{g\sqrt{\varepsilon}}\,(K_x + n), \tag{9}$$

where K_x is the x component of the normalized wave vector. The condition is equal to the secondary dispersion relation of Eq.(5), on the condition that $\alpha = 1/\sqrt{\varepsilon}$. In the experiment, the value of α derived from the PTFE sphere was a little larger than that of cylinder; it is consistent with the above consideration.

The above discussion is based on that radiation emitted from the unit crystal is composed of radiation directly generated from the electron and of response to incident radiation generated in the upstream unit crystals. Since the incident radiation is composed of a pulse train of radiation generated in the nearest neighbor upstream unit crystal, radiation in the second nearest one and so on, at the observation point the radiation from the unit crystal may be formally written by

$$E_r = \{A + Be^{i\Delta\varphi}[1 + re^{i\Delta\varphi} + r^2e^{i2\Delta\varphi} + \cdots]\} \exp(i(\boldsymbol{kx} - \omega t)), \tag{10}$$

where A and B are the amplitude of radiation directly generated by the electron and that of the response to radiation generated in the nearest neighbor upstream unit crystal, respectively. The phase difference between radiation "a" and "b" is expressed by $\Delta\varphi$, using the propagation time δt,

$$\Delta\varphi = \boldsymbol{k}\,\Delta\boldsymbol{x} - \omega\delta t = g\left(k_x - \frac{\omega\sqrt{\varepsilon}}{c}\right), \tag{11}$$

and r is a damping factor of amplitude in propagation per unit crystal.

The total radiation from every unit crystal is written by

$$\begin{aligned} E_t &= \left(A + \frac{Be^{i\Delta\varphi}}{1 - re^{i\Delta\varphi}}\right)\exp(i(\boldsymbol{kx} - \omega t))\,(1 + e^{i\Delta\phi} + e^{i2\Delta\phi} + \cdots) \\ &= \left(A + \frac{Be^{i\Delta\varphi}}{1 - re^{i\Delta\varphi}}\right)\frac{\exp(i(\boldsymbol{kx} - \omega t))}{1 - e^{i\Delta\phi}}, \end{aligned} \tag{12}$$

where $\Delta\phi$ is the phase difference of radiation between neighboring crystals,

$$\Delta\phi = \boldsymbol{k}\,\Delta\boldsymbol{x} - \omega\Delta t = g\left(k_x - \frac{\omega}{\beta c}\right). \tag{13}$$

The intensity becomes

$$|E_t|^2 = \left(A^2 + \frac{B^2 + 2AB(\cos\Delta\varphi - r)}{1 + r^2 - 2r\cos\Delta\varphi}\right)\frac{1}{4\sin^2(\frac{\Delta\phi}{2})}. \tag{14}$$

The radiation peak appears when the following condition is satisfied:

$$\frac{\Delta\phi}{2} = n\pi. \tag{15}$$

The dispersion relation of SPR is directly reduced from this condition. In addition, the second term of Eq.(12) is similar to the radiation from a Fabry-Perot resonator and shows also oscillating characteristic. Its peaks appear under the condition,

$$\Delta\phi = 2n\pi. \tag{16}$$

The condition is corresponding to the secondary dispersion relation. Hence we can take the relation as the new resonant dispersion relation. When the peak condition of Eq.(16) is fulfilled, the intensity is given by

$$|E_t|^2 = \left(A^2 + \frac{2AB}{1+r} + \frac{B^2}{(1+r)^2}\right) \frac{1}{4\sin^2(\frac{\Delta\phi}{2})} \quad . \tag{17}$$

These equations show that the radiation intensity along the SPR dispersion relation defined by Eq. (15) will be much higher than the radiation emitted under the condition of Eq.(16). On the other hand, Eq.(16) is not sufficient condition for the secondary dispersion relation. When the damping factor r is small or far from unity, the radiation peak will be vague, supposing that the condition is fulfilled. However, if r is near to unity, the intensity will be high enough to show the new resonant dispersion relation.

The above consideration shows that the dispersion relation of SPR is caused from the constructive interference of radiation directly excited by the electron. On the other hand, the secondary dispersion relation seems to originate from the interference between radiation directly excited by the electron and radiation indirectly generated in the upstream crystals.

Acknowledgement

We appreciate Professors J. Kawamura and T. Arima of IMRAM, Tohoku University for their encouragement and support, and Professor emeritus K. Mizuno of Tohoku University for his kind support to utilize the low temperature InSb detector. We also thank Messrs. T. Tsutaya, Y. Chiba of IMRAM, the member of the optical group of Photodynamics Center, RIKEN, and the staff of LNS, Tohoku University, for their help in the experiment. This work was supported by the Special Coordination Funds for Promoting Science and Technology from the Ministry of Education, Culture, Sports, Science, and Technology of Japan.

References

[1] K. Yamamoto, R. Sakakibara, S. Yano, Y. Segawa, Y. Shibata, K. Ishi, T. Ohsaka, T. Hara, Y. Kondo, H. Miyazaki, F. Hinode, T. Matsuyama, S. Yamaguti, and K. Ohtaka: Phys. Rev. E **69** (2004) 045601.

[2] S. J. Smith and E. M. Purcell: Phys. Rev. **92** (1953) 1069.

[3] N. Horiuchi, T. Ochiai, J. Inoue, Y. Segawa, Y. Shibata, K. Ishi, Y. Kondo, M. Kanbe, H. Miyazaki, F. Hinode, S. Yamaguti, and K. Ohtaka: Phys. Rev. E **74** (2006) 056601.

[4] K. Ohtaka and S. Yamaguti: Opt. Spectrosc. **91** (2001) 477.

[5] S. Yamaguti, J. Inoue, O. Haeberl , and K. Ohtaka: Phys. Rev. B **66** (2002) 95202.

(LNS Experiment : #2537, #2553)

Properties of the Coherent Radiation Emitted from Photonic Crystal in the Millimeter Wave Region. Ⅱ

Y. Shibata[1], K. Ishi[1], T. Tsutaya[1], N. Horiuchi[2], Y. Segawa[2], Y. Kondo[3], H. Miyazaki[3], F. Hinode[4], T. Ochiai[5], and K. Ohtaka[6]

[1]*Institute of Multidisciplinary Research for Advanced Materials, Tohoku University, Katahira, Sendai 980-8577*

[2]*Photodynamics Research Center, The Institute of Physical and Chemical Research (RIKEN), Sendai 980-0845*

[3]*Graduate School of Engineering, Tohoku University, Aramaki, Sendai 980-8579*

[4]*Laboratory of Nuclear Science, Tohoku University, Mikamine, Sendai 982-0826*

[5]*Nanomaterials Laboratory, National Institute for Materials Science (NIMS), Tsukuba 305-0044*

[6]*Center for Frontier Science, Chiba University, Chiba 263-85226*

Properties of coherent radiation emitted from a Photonic crystal (PhC) is studied by experiments in the millimeter wave region, under various geometric arrangements of the PhC with respect to an electron beam, such as (1) reflective arrangement, (2) refractive arrangement and (3) longitudinal shift. In these arrangements, we observe not only the dispersion relation of Smith-Purcell radiation but also another relation or the secondary relation. The influence of the arrangement on the coherent radiation is mainly discussed in the (k_x, ω) diagram.

§1. Introduction

When a short-bunched beam of electrons of a linear accelerator passes by near the surface of a photonic crystal (PhC), coherent radiation is emitted in the millimeter wavelength region [1, 2]. In this paper we call it the photonic crystal radiation. The origin of the radiation is in essence considered to be the same as that of Smith-Purcell radiation (SPR), which is emitted from the electron passing by a metallic grating [3].

To elucidate the properties of photonic crystal radiation, we have made a series of experiments by changing the geometrical arrangement of PhC to the electron beam. Following the previous report (refered to as paper I [4]), here we report the experiments on (1) the reflective or refractive arrangement, (2) interference between photonic crystal radiation from the two arrangements and (3) longitudinal shift of PhC.

We adopted here the same technical terms in the paper I [4], where the background of the photonic crystal radiation was briefly described.

§2. Reflective or Refractive Arrangements

2.1 Experiment

The experimental setup is schematically shown in Fig.1. In the case of (a), a short-bunched beam of electrons from the linear accelerator at Laboratory of Nuclear Science (LNS), Tohoku University moved with constant velocity v along the x axis above a PhC. The photonic crystal radiation from the PhC was observed in the xz plane, and the emission angle θ was measured from the x direction. In the case (b) the PhC was placed above the trajectory of the electron beam; the position of the PhC was symmetric to that of (a) with respect to the xy plane. Hereafter we call the set up (a) the reflective arrangement, and (b) the refractive arrangement.

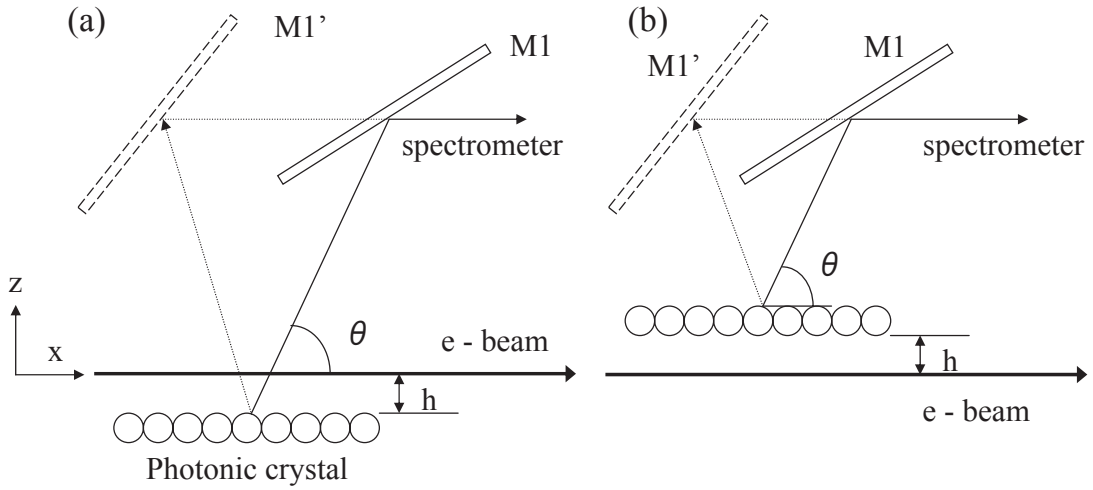

Fig.1. Schematic layout of the experiment of reflective arrangement (a) and refractive arrangement (b). The electron orbit was shown by the thick solid line. The emission angle θ was measured from the x direction.

In both arrangement, the photonic crystal radiation was guided to a Martin-Puplett type Fourier-transform spectrometer and was detected with a low-temperature InSb detector. The resolution of the spectrometer was 0.125 cm^{-1} or 3.75 GHz. The plane mirror M1 was controlled its position and directionality with a stepping motor to cover the emission angle θ between 60° and 120°, keeping the optical axis unaltered. The acceptance angle of the measuring system depended a little on the angle θ and was $\pm$ 0.75° in the xz plane and $\pm$ 1.2° in the yz plane at $\theta = 90°$. The impact parameter or the distance between the electron beam and the surface of the PhC was set to be 10 mm.

The beam condition was as followings. The energy of the electron was 150 MeV and its spread was less than 2.5 %, the macro and micro pulse widths were roughly 1.5 μs and 0.67 ps, respectively. The repetition of the macro pulse was 50/3 Hz and the average beam current was 0.9 μA. The cross section of the beam was nearly circular and about 10 mm in diameter. Since the energy of the electron was 150 MeV, the velocity of the electrons was $v = 0.999994\,c$.

As the PhC we prepared two samples used in paper I: a monolayer of polytetrafluoroethylene (PTFE) spheres and that of arrayed cylinders of PTFE.

In the experiment, the emission spectrum of photonic crystal radiation was measured with the spectrometer, by controlling θ from 60° to 115° by 1° step. From the spectrum, using the relation $k_x = (\omega / c) \cos\theta$, we obtained the contour map of the intensity of the photonic crystal radiation in the (k_x, ω) diagram.

In the series of experiments, the measuring system and PhC used was common, and the accelerator was carefully tuned to keep the same beam condition. Detail of the experiment including setup on the other arrangements is described in later.

2.2 Results and discussion

2.2.1 Radiation in reflecting arrangement

Using the reflective arrangement, we measured the photonic crystal radiation from the monolayer of the PTFE spheres with the spectrometer and derived the contour map of the intensity from the spectra. The result is shown in Fig. 2, where the abscissa is the x component of the normalized wavevector $K_x = g k_x / 2\pi = g \cos\theta / \lambda$ with the period g and the ordinate is the frequency of radiation $\nu = \omega / 2\pi$ in GHz.The solid lines show the theoretical dispersion relation of SPR calculated with the diameter of the sphere d of 3.2 mm, *i.e.,* the υ_n lines given by Eq. (4) of the paper I [4] .

The observed (k_x , ω) map had the same characteristics to those of paper I. The photonic crystal radiation holds two dispersion relations; one is the relation of SPR and the other is the secondary dispersion relation, not expected from a simple theory of the photonic crystal radiation. We can take the relation as the new resonant dispersion relation [4]. The new relation was calculated with Eq. (5) of the

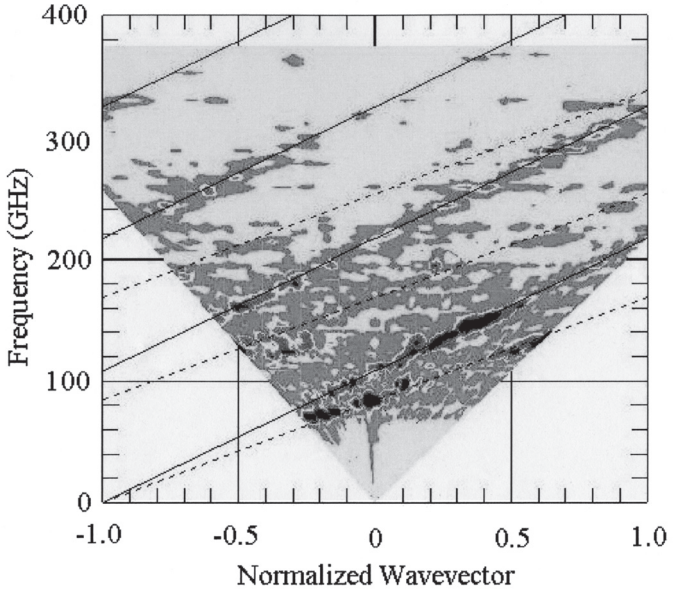

Fig.2. The contour map of the intensity of photonic crystal radiation from the PTFE spheres in the (k_x, ω) plane observed in the reflective arrangement. The abscissa and ordinate are the normalized wave vector K_x and the frequency of the radiation, respectively. The solid and broken lines show the v_n and u_n lines, respectively, calculated for the diameter of the sphere $d = 3.2$ mm.

paper I on the condition that $\alpha = 0.78$ and is shown by the broken lines in Fig.2. Along both the relations with $n = 1$, each radiation intensity varied sharply with the emission angle θ.

2.2.2 Radiation in refractive arrangement

The experimental setup was changed to the refractive arrangement, and the spectra of the photonic radiation from the monolayer of the PTFE spheres were measured for the emission angle θ from 60° to 115°. The obtained contour map is shown in Fig.3, where the υ_n and u_n lines are shown by the solid and broken lines, respectively, calculated on the condition that $d = 3.18$ mm and $\alpha = 0.78$. Ignoring the small difference in the fitting parameter d, we consider that the υ_n and u_n lines in Fig.3. are the same as those of Fig.2.

Figure 3 shows in general the same characteristics to those of the reflective arrangement shown in

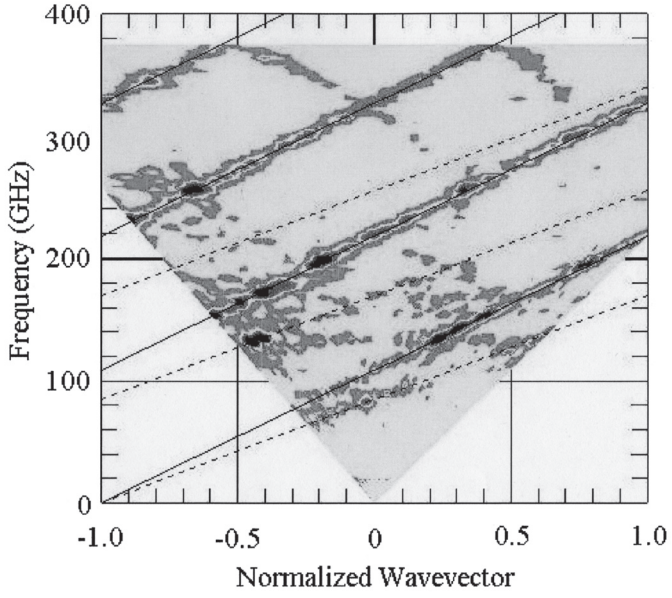

Fig.3. The contour map of the intensity of photonic crystal radiation from the PTFE spheres in the (k_x, ω) plane observed in the refractive arrangement. The solid and broken lines show the v_n and u_n lines, respectively, calculated for d = 3.18 mm.

Fig.2. The photonic crystal radiation in refractive arrangement also holds both the dispersion relations, the SPR one and the new resonant relation. New features such as the new dispersion relation did not appear in the (k_x, ω) diagram. However, the comparison of Figs.2 and 3 clearly shows a few differences as following. The higher order dispersion relation of SPR is conspicuous in Fig.3. On the other hand, the new resonant dispersion relation has no such feature. The photonic crystal radiation seems to be suppressed in the low frequency region, that is to say, less than about 120 GHz or 4 cm^{-1}. The suppression is common in both dispersion relations.

To confirm the features, we replaced the PhC from the monolayer of the PTFE spheres to the monolayer of the PTFE cylinders and measured its emission spectra. The contour map derived from the spectra is shown in Fig.4. The solid lines show the dispersion relation of SPR calculated for the diameter of the cylinder d of 3.1 mm, and the broken lines show two series of the new resonant relation

calculated with $\alpha = 0.78$ and 0.83.

In this experiment, to save our experimental time, we have not observed the photonic crystal radiation of the PTFE cylinders in the reflective arrangement. As reference we show Fig.5 obtained from the same PTFE cylinders in the later experiment on the longitudinal shift (reflective

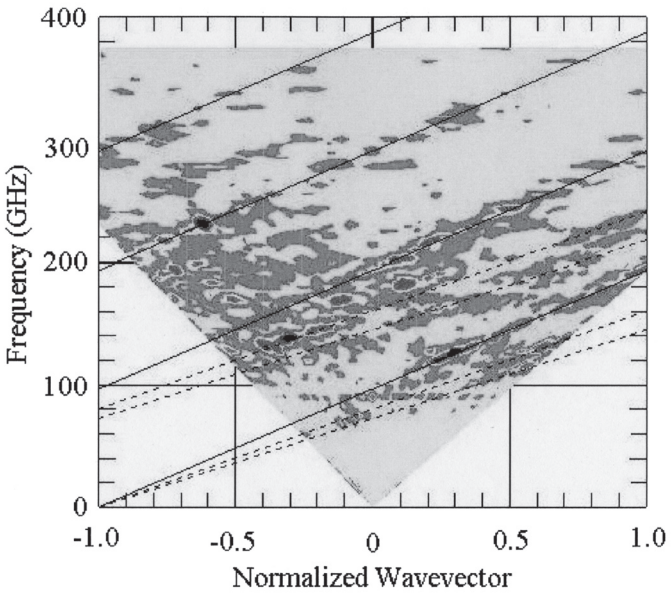

Fig.4. The contour map of the photonic crystal radiation from the PTFE cylinders in the (k_x, ω) plane observed in the refractive arrangement. The solid and broken lines show the v_n and u_n lines, respectively, calculated for d = 3.1 mm.

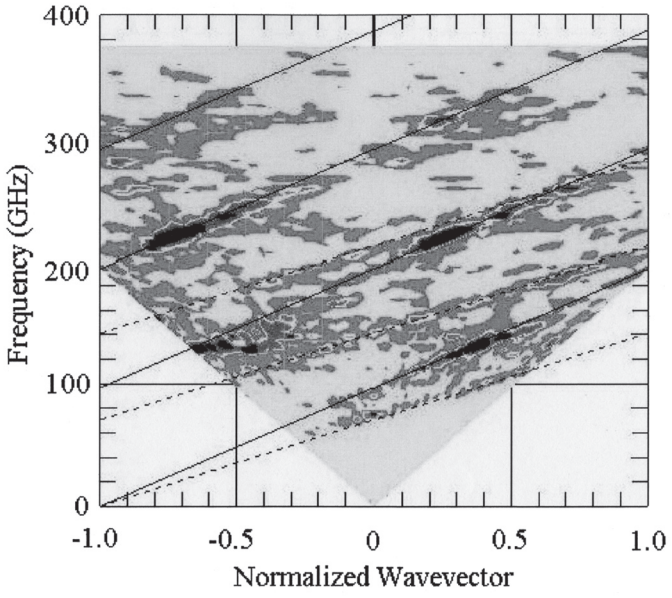

Fig.5. The contour map of the photonic crystal radiation from the PTFE cylinders of the reflective arrangement measured in later experimental time on the longitudinal shift. The solid and broken lines show the v_n and u_n lines, respectively, calculated for d = 3.1 mm.

arrangement). In the figure the contour map is obtained for the emission angle θ between 60° and 120°, so the observed range θ is a little different from Fig.4. The solid and broken lines are just the same to those in Fig.4.

During the experiment, the beam condition of the electrons fluctuated in various time scales. In addition the tune of the electron beam suffered a little variation from experiment to experiment. These effects resulted in various fluctuations in the experimental results, in particular to the absolute intensity. Hence the contour map of Fig.5 suffered influence from the fluctuation of the experimental conditions. Taking into account the influence, we considered that Fig.4 held the same features as the case of Fig.2; the second and third order dispersion relation of SPR was prominent and the photonic crystal radiation in the low frequency seemed to be suppressed.

In the case of the cylinder monolayer, as seen in Fig.4, the new resonant dispersion relation was not clear. We considered that the dispersion relation appeared vague because of the suppression of the photonic crystal radiation in the low frequency.

To derive much information from the experiment, we prepared double layers of the PTFE spheres; two monolayers of the triangular lattice of the spheres were stacked up just sphere on sphere in the refractive arrangement, as shown in Fig.6. The impact parameter was kept to 10 mm. The obtained (k_x, ω) map is shown in Fig.7, where the solid lines show the dispersion relation of SPR calculated for the diameter of the sphere d of 3.2 mm, and the broken lines show the u_n lines with $\alpha = 0.78$. In comparison with the contour map of the monolayer, relative intensity of the photonic crystal radiation in the low frequency between 60 GHz and 120 GHz is not vague and both the SPR relation and the new resonant relation are clearly seen.

Theoretical simulation of the photonic crystal radiation from the monolayer of the triangular lattice of the PTFE spheres has been carried out under the condition that the multipole scattering of the incident evanescent wave due to the sphere was fully taken into account [5]. The results are

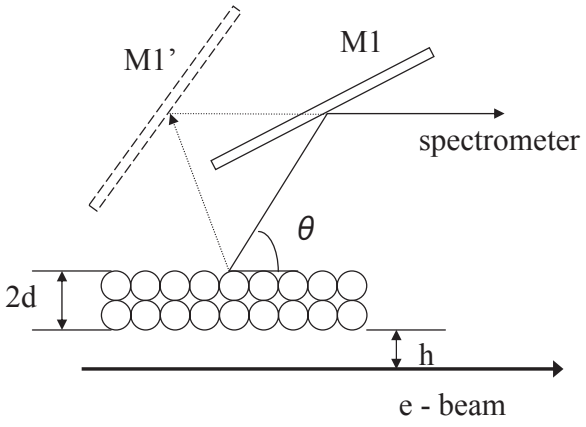

Fig.6. Schematic layout of the experiment used in the experiment of two layers of the PTFE spheres in refractive arrangement.

summarized as follows. The (k_x, ω) map of the photonic crystal radiation shows two dispersion relations; one was the relation of SPR and the other was corresponding to the new resonant relation, whose gradient was roughly 0.8 times that of the SPR relation. Furthermore the (k_x, ω) diagram of the photonic crystal radiation in refractive arrangement showed almost the same features to those of reflective arrangement. The theoretical dispersion relations are in accordance (or at least not conflict) with the experiment, though the intensity distribution along the dispersion relation was not compared in detail between the simulation and the experiment.

On the other hand, the observed difference of the (k_x, ω) maps between the two arrangements seems not to be in accordance with the simulation. Though the origin of the difference is not clear at present, we consider as follows. When a high-energy electron passes by near the PhC, Cherenkov radiation is generated in the PhC. The above theoretical formulation is fully taking into account the generation of Cherenkov radiation. However, in our experiment the size of the PTFE sphere was nearly the same to the formation length of Cherenkov radiation [6]. It means that Cherenkov radiation is partly suppressed in the low frequency region, $\lambda > (\sqrt{\varepsilon} - 1)\, d$, where ε stands for the dielectric constant of PTFE, *i.e.*, $\sqrt{\varepsilon} = 1.44$. Since Cherenkov radiation is an outgoing wave from the electron orbit, we consider that Cherenkov radiation is mainly observed through the refractive arrangement. Hence the suppression of photonic crystal radiation observed in the low frequency region is caused from suppression of Cherenkov radiation. Stacking of the monolayer of the PTFE spheres is considered to shift the effect of the formation length of Cherenkov radiation to the low frequency side. The low frequency part of the (k_x, ω) map of Fig.7 seems to support this explanation.

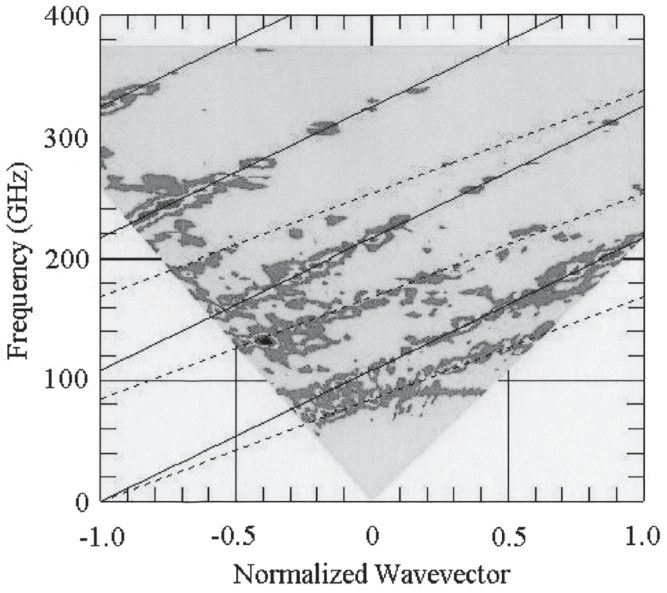

Fig.7. The contour map of the photonic crystal radiation in the (k_x, ω) plane observed with the setup shown in Fig.6. The solid and broken lines show the v_n and u_n lines, respectively, calculated for d = 3.2 mm.

§3. Superposition of Radiation from Reflective and Refractive Arrangements

To examine properties of the photonic crystal radiation, we changed the experimental setup to the one as shown in Fig.8. The two monolayers of the PTFE cylinders were separated by the distance $2h$ so that the electron beam passed through the center line of the two layers along the x axis. Separation between the two layers was controlled with a stepping motor; both the upper and lower layers were moved along the z axis, always keeping that the impact parameter h of the upper layer was the same to the lower one. To save the experimental time, limited number of spectra were observed and hence the contour map of the (k_x, ω) diagram was not derived.

In the experiment, we controlled the separation distance from 20.0 mm to 24.0 mm by 0.2 mm step and observed the spectra of the photonic crystal radiation from the two layers. The spectral structure showed complex variation with the distance and was hard to analyze. However, a few peaks of the spectrum in low frequency showed rather periodic variation. The open circles in Fig.9 show variation of the intensity of three peaks of 75 GHz, 97.5 GHz and 157.5 GHz, observed at the emission angle $\theta = 90^\circ$. Figure 10 also shows that of 127.5GHz at $\theta = 110^\circ$, The abscissa shows half of the separation or impact parameter h.

The photonic crystal radiation from the two layers can be taken as superposition of the photonic crystal radiation from the upper monolayer and that of the lower layer. Let the radiation field from the upper monolayer be expressed by

$$E_1 = \alpha_1 \exp\left(-\frac{2\pi h}{\beta\gamma\lambda}\right) \exp\left(-i\left(\boldsymbol{k}\boldsymbol{x}_1 - \omega t\right)\right), \tag{1}$$

where $\beta = v/c$ and γ is the relativistic factor. We suppose that the radiation field from the lower monolayer is expressed by the same equation. Since the radiation from the lower monolayer propagated

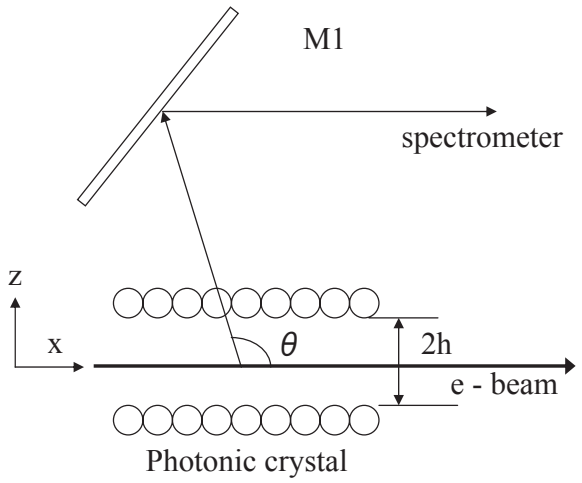

Fig.8. Schematic layout of the experiment on the superposition of photonic crystal radiation from reflective arrangement and from refractive one. The electron orbit was shown by the thick solid line.

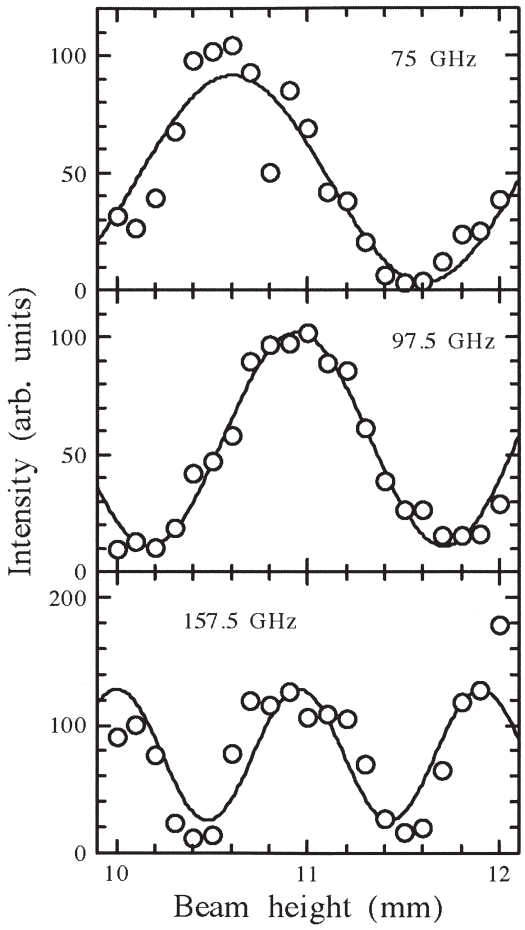

Fig.9. The variation of the peak intensity as a function of beam height h observed at θ=90°. In the figure the peak frequency was 75 GHz, 97.5 GHz and 157.5 GHz from top to bottom. The solid curves were fitted to the data by least square's method.

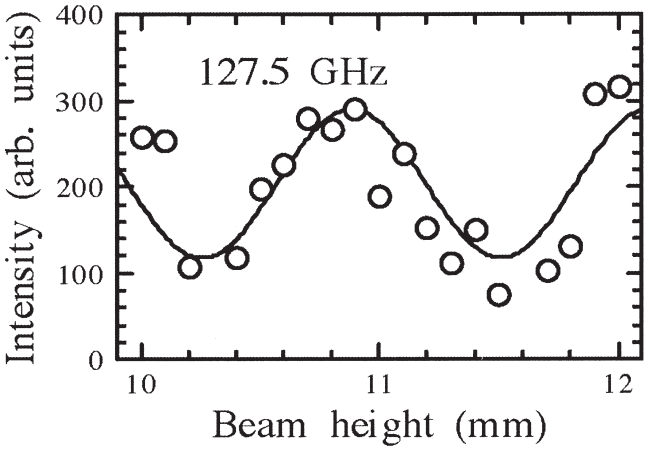

Fig.10. The variation of the intensity of 127.5 GHz peak as a function of beam height h observed at θ=110°. The solid curve was fitted to the data by least square's method.

to the observation point through the upper monolayer, we consider the radiation field from the lower monolayer is written by

$$E_2 = \alpha_2 \exp\left(-\frac{2\pi h}{\beta\gamma\lambda}\right) \exp\left(-i\left(\boldsymbol{k}\boldsymbol{x}_2 - \omega t - \Delta\phi\right)\right), \tag{2}$$

where $\Delta\phi$ shows phase difference between two waves E_2 and E_1. Hence the radiation intensity from the two monolayers is given by, supposing that $\boldsymbol{k}(\boldsymbol{x}_2 - \boldsymbol{x}_1) = 4\pi h \sin\theta/\lambda$,

$$I = |E_1 + E_2|^2 = \left(\alpha_1^2 + \alpha_2^2 + 2\alpha_1\alpha_2 \cos\left(\frac{4\pi h}{\lambda}\sin\theta + \Delta\phi\right)\right) \exp\left(-\frac{4\pi h}{\beta\gamma\lambda}\right). \tag{3}$$

Since, in our experiment, $\beta\gamma \sim 300$ and the variation of h was small, we can approximate Eq. [3] by

$$I = A + B\cos\left(\frac{4\pi h \sin\theta}{\lambda} + \Delta\phi\right). \tag{4}$$

The solid curves in Figs.9 and 10 show the equation fitted to the experiment by least square's method. The solid curve is roughly in agreement with the experiment. In Fig.9, the peaks of 97.5 GHz and 157.5 GHz belong to the radiation satisfying the dispersion relation of SPR and the 75 GHz peak belongs to the new resonant relation. The fitting parameters of these peaks resulted in A ~ B, which means that the experiment is consistent with the above assumption.

The peak of 127.5 GHz corresponds to the point (— 0.45, 127.5 GHz) in the (k_x, ω) diagram; the point is placed neither on the solid lines nor on the broken ones. We can take the point corresponds to another dispersion relation whose slope was 83% of the SPR relation. It may suggest that the photonic crystal radiation has a few series of the new dispersion relation.

§4. Longitudinal Shift

4.1 Experiment

To examine the influence of the edge of PhC, the experimental setup was changed as schematically shown in Fig.11. The optical system was fabricated to collect the plane wave passing through the aperture D of 76 mm in the xz plane. The optical axis was designed to pass through the centers of the aperture and of the surface area of PhC. This optical system was common to the series of the experiment of this report.

In this experiment, the prepared PhC was arrayed monolayer of the PTFE cylinders in reflective arrangement and its position was controlled with a stepping motor to move along the x axis. The x-shift of the PhC was measured from a fixed point A and was controllable from 0 mm to 50 mm. Since the number of cylinders used was 27, the length of the monolayer in the x direction was 81 mm, which was larger than the aperture D. In the case of the x-shift of 18mm, the optical axis of the measuring system just passed through the center of the surface of the PhC. The contour map in the (k_x, ω) diagram measured with the x-shift of 18mm was shown in Fig.5.

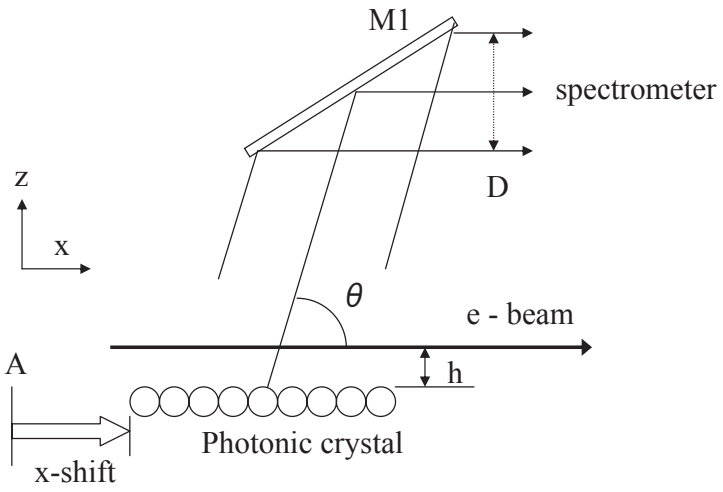

Fig.11. Schematic layout on the longitudinal shift or x-shift. The electron orbit was shown by the thick solid line. The PhC was moved horizontally along the x axis with a stepping motor.

4.2 Results and discussion

We measured the emission spectra for various positions of PhC in the x direction. The results are shown in Figs.12(a), 12(b), 13(a) and 13(b) for the emission angle θ = 78°, 85°, 90° and 106°, respectively. In these figures, spectra were shifted vertically to make the comparison clear, and the value of the x-shift was from 0 mm to 50 mm by 5 mm step from top to bottom. These figures in general showed that the spectral structure was a little affected by the x-shift, even though the peak intensity itself was varied systematically.

In Fig.12(a), the peak intensity around at 120 GHz was nearly constant and slowly decreased with the x-shift. On the other hand, the intensity at 240 GHz increased with the x-shift. The radiation of 120 GHz belonged to the dispersion relation of the first order SPR and that of 240 GHz to the second order of SPR. The small peak at 165 GHz, belonging to the second order of the new resonant dispersion relation, was nearly constant with the shift. Figure 12(b) showed that both the radiation peaks around at 210 GHz and 320 GHz, belonging to the 1st and 2nd order SPR, increased with the shift. The peak at 155 GHz, belonging to the 2nd order of the new resonant radiation, decreased with the shift. In Fig.13(a) the radiation peak of 75 GHz and 140 GHz, belonging to the 1st and 2nd order of the new resonant radiation, seemed to show periodic variation with the shift. The peak of 195 GHz, belonging to the 2nd order of SPR, gradually increased with the shift. Finally in Fig.13(b) the peak of 130 GHz decreased with the shift and that of 225 GHz belonging to the 2nd order of SPR increased with the shift. The radiation peak of 130 GHz belongs to neither SPR nor the new resonant radiation. The peak seemed to belong other dispersion relation whose slope was 83 % of the SPR relation in the (k_x, ω) diagram.

The case of the x-shift of 50 mm means that the PhC was placed at the most downstream position, and hence the upstream edge of the monolayer was near to the center of the field of view of the measuring system. On the other hand, in the case of x-shift of 0 mm, our system observed the radiation

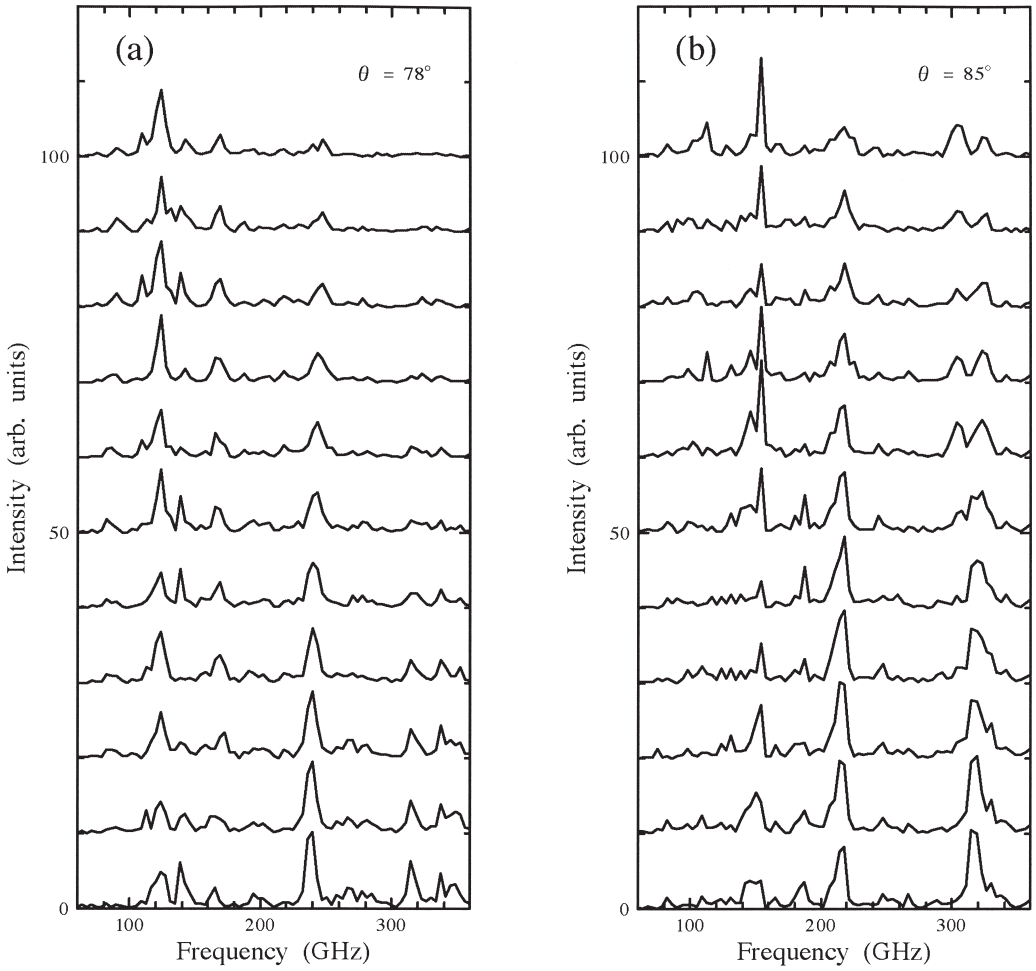

Fig.12. Variation of the spectra observed at θ=78° (a) and 85° (b). From top to bottom, the figures show the spectra of x-shift from 0 mm to 50 mm by 5 mm step.

emitted at the downstream edge of the monolayer. If radiation emitted from each of the cylinders was summed up coherently, the intensity should increase with the number of the cylinders. It means that such the radiation peak decreases with the shift. We therefore simply expected that the radiation peak belonging to the dispersion of SPR decreased with the shift. On the contrary, the experiment showed that the peaks of the SPR relation mildly increased with the shift. The reason of this contradiction is not clear at present.

On the other hand, many of peaks belonging to the new resonant dispersion relation decreased with the shift. It suggests whether the new resonant radiation is essential part of the photonic crystal radiation or the radiation is emitted from the downstream edge of the monolayer. The experiment showed implicitly that the upstream edge of the monolayer was irrelevant to the new resonant radiation.

Acknowledgement

We appreciate Professors J. Kawamura and T. Arima of IMRAM, Tohoku University, for their encouragement and support, and professor emeritus K. Mizuno of Tohoku University for his kind

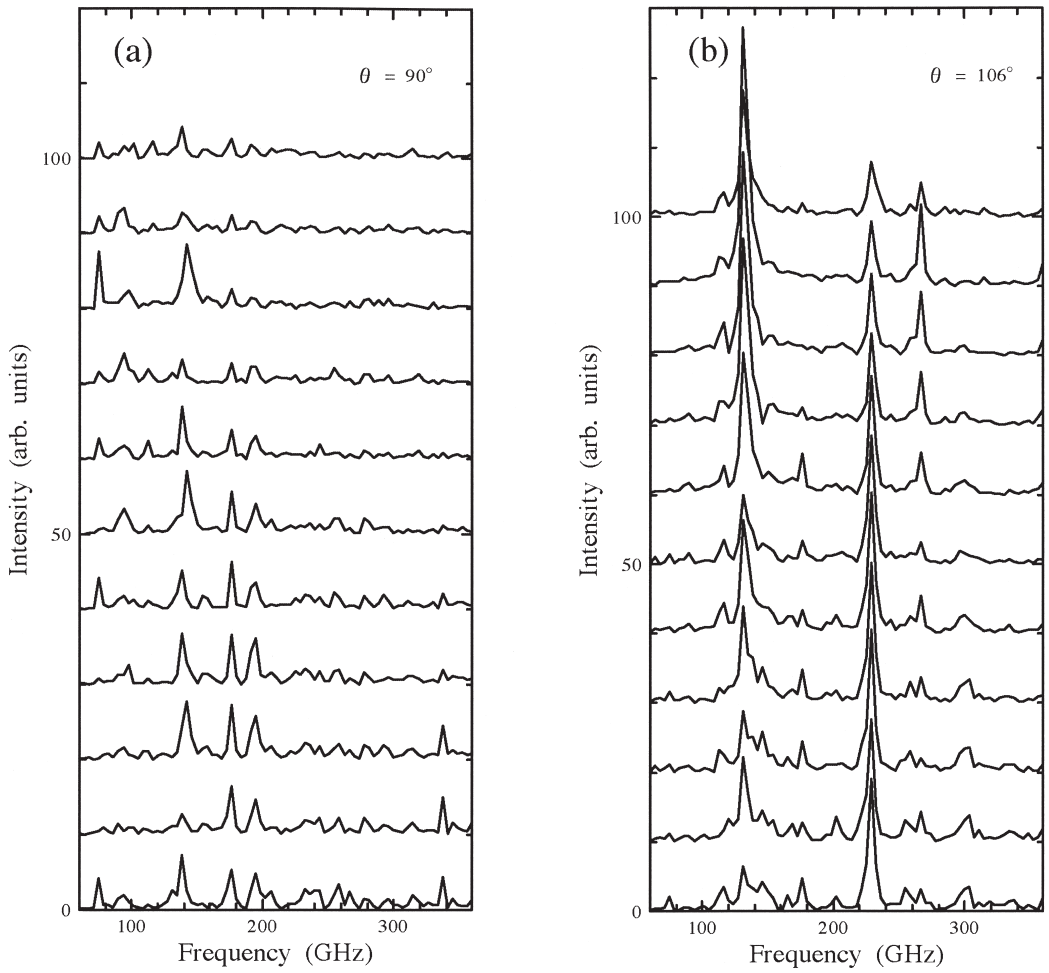

Fig.13. Variation of the spectra observed at θ=90° (a) and 106° (b). From top to bottom, the figures show the spectra of x-shift from 0 mm to 50 mm by 5 mm step.

support to utilize the low temperature InSb detector. We also thank Messrs. T. Tsutaya, Y. Chiba of IMRAM, the member of the optical group of Photodynamics Center, RIKEN, and the staff of LNS, Tohoku University, for their help in the experiment.

References

[1] K. Yamamoto, R. Sakakibara, S. Yano, Y. Segawa, Y. Shibata, K. Ishi, T. Ohsaka, T. Hara, Y. Kondo, H. Miyazaki, F. Hinode, T. Matsuyama, S. Yamaguti, and K. Ohtaka: Phys. Rev. E **69** (2004) 045601.

[2] N. Horiuchi, T. Ochiai, J. Inoue, Y. Segawa, Y. Shibata, K. Ishi, Y. Kondo, M. Kanbe, H. Miyazaki, F. Hinode, S. Yamaguti, and K. Ohtaka: Phys. Rev. E **74** (2006) 056601.

[3] S.J. Smith and E.M. Purcell: Phys. Rev. **92** (1953) 1069.

[4] Y. Shibata, K. Ishi, T. Tsutaya, N. Horiuchi, Y. Segawa, Y. Kondo, H. Miyazaki, F. Hinode, T. Ochiai, and K. Ohtaka: Research Report of LNS, Tohoku Univ., **39** (2006) 55.

[5] H. Miyazaki: private communications (2006).

[6] T. Takahashi, Y.Shibata, K.Ishi, M.Ikezawa, M.Oyamada, and Y. kondo: Phys. Rev. E **62** (2006) 8606.

(LNS Experiment : #2537, #2553)

Properties of the Coherent Radiation Emitted from Photonic Crystal in the Millimeter Wave Region. Ⅲ

Y. Shibata[1], K. Ishi[1], T. Tsutaya[1], N. Horiuchi[2], Y. Segawa[2], Y. Kondo[3], H. Miyazaki[3], and F. Hinode[4]

[1]*Institute of Multidisciplinary Research for Advanced Materials, Tohoku University, Katahira, Sendai 980-8577*
[2]*Photodynamics Research Center, The Institute of Physical and Chemical Research (RIKEN), Sendai 980-0845*
[3]*Graduate School of Engineering, Tohoku University, Aramaki, Sendai 980-8579*
[4]*Laboratory of Nuclear Science, Tohoku University, Mikamine, Sendai 982-0826*

Coherent radiation emitted from a Photonic crystal of a cylindrical tube of Teflon with periodic grooves is observed in the millimeter wave region. The observed spectra show a sharp peak at frequency of 4.625 cm^{-1}. The inter-bunch coherence of the radiation is confirmed with an interferometer.

§1. Introduction

When a short-bunched beam of electrons of a linear accelerator passes by near the surface of a photonic crystal (PhC), coherent photonic crystal radiation is emitted in the millimeter wavelength region [1-4].

In this report, to examine possibility of application to beam diagnostics, we have tentatively observed photonic crystal radiation generated from high-energy electrons passing through the center of a tube of Teflon, whose outer surface has periodic grooves.

§2. Experiment

The experimental setup is schematically shown in Fig.1. A short-bunched beam of electrons from the linear accelerator at Laboratory of Nuclear Science (LNS) , Tohoku University moved with a constant velocity v along the center line of a cylindrical tube of a PhC. Let suppose that the center line is x axis and horizontal plane is parallel to the xy plane. The photonic radiation from the PhC was guided by a mirror system to a Martin-Puplett type Fourier transform spectrometer and was detected with a low temperature hot-electron bolometer. The emission angle θ was measured from the x direction.

The beam condition was as followings. The energy of the electron was 150 MeV and its spread was less than 2.5%, the macro and micro pulse widths were roughly 1.5 μs and 0.67 ps, respectively. The repetition of the macro pulse was 50/3 Hz and the average beam current was 0.9 μA. The cross section of the beam was nearly circular and about 10 mm in diameter.

The PhC was fabricated from a cylindrical tube of polytetrafluoroethylene (PTFE : Teflon) having the size of 100 × ϕ60 × ϕ30 mm in total length × outer diameter × inner diameter. The outer surface of the tube had periodic grooves with cylindrical symmetry. The cross section of the groove is shown in the

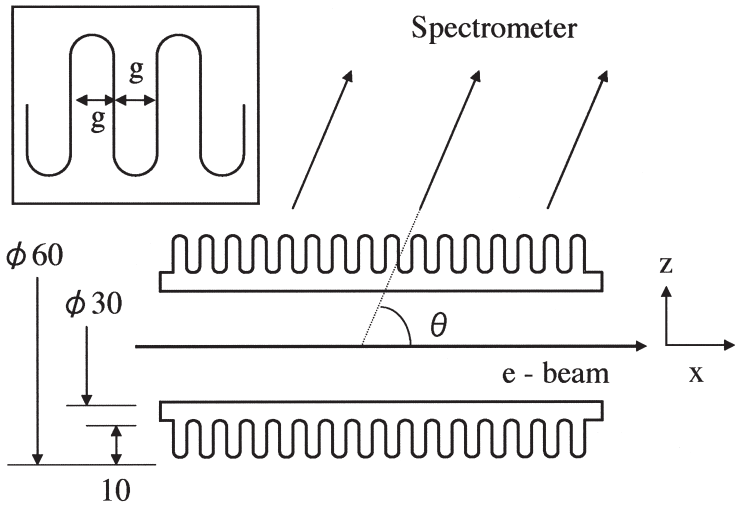

Fig.1. Schematic layout of the experiment. The electron orbit is shown by the thick solid line. The emission angle θ was measured from the x direction. The inset shows the shape of groove.

inset of Fig.1; the top and bottom of the grooves were semi-circle with the size of 3 mm in diameter, and the period of the grooves was 6 mm (g = 3 mm) in the x direction.

§3. Results and Discussion

The spectra of photonic crystal radiation were observed for the emission angles θ of 110°, 100°, 90°, 80° and 70°, and were shown in Fig.2. Each of the observed spectra was composed of several peaks. Every spectrum has the main peak at frequency ν of 4.625 cm^{-1} or wavelength of λ = 2.16 mm and its overtone at 9.25 cm^{-1} though the intensity was weak.

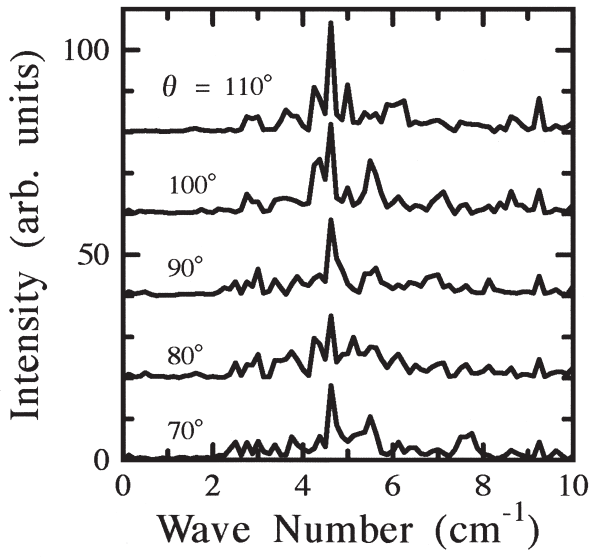

Fig.2. The spectra observed at θ = 110°, 100°, 90°, 80° and 70°. The spectra are vertically shifted to make comparison clear.

When we observed the photonic crystal radiation from the arrayed PTFE spheres or the arrayed PTFE cylinders, the observed peaks satisfied the dispersion relation of Smith-Purcell radiation and/or the new resonant dispersion relation [2-4]. The peak frequency therefore depended on the emission angle θ. On the contrary, the peak frequency in Fig. 2 did not depend on the emission angle. The reason of the difference is not clear at present.

The outer grooves of the Teflon cylinder had the period of 6 mm. Hence, the spectrum observed at θ = 90° was expected to have an intense peak at ν = 1.67 cm^{-1} or at λ = 6 mm. Taking into account the sensitivity of our measuring system, the peak of 1.67 cm^{-1} may be difficult to observe. Even so, the higher harmonics should be observed. However, the peak or one of its overtones was not observed. The reason is not clear.

If we assume that the radiation generated in the Teflon cylinder is confined in the grooves, the radiation having a periodic condition of $g\sqrt{\varepsilon} = \lambda$ will survive, where $g\sqrt{\varepsilon}$ stands for the optical length of one groove. It is interesting that, since $\sqrt{\varepsilon}$ = 1.44 for Teflon, the wavelength with $m = 2$ becomes to λ = 2.16 mm which corresponds to the peak wavelength. It is not clear whether the correspondence was fortuitous or not.

The interferogram of the photonic crystal radiation was observed at θ = 90°, and is shown in Fig.3. The interference pattern around at 0 mm in the optical path difference was repeated at around 105 mm. The result clearly showed the inter-bunch coherence of radiation generated from the S-band linac.

The experimental result showed that the observed radiation will be applicable to beam diagnostics. However, theoretical simulation of the photonic crystal radiation is necessary to forward the application. In the experiment, we fabricated a similar cylindrical photonic crystal of Teflon with rectangular grooves with the same period. But the radiation was scattered over wide emission angle and weak at around θ = 90°. It suggests that the cross section of the groove is important in the application.

Acknowledgement

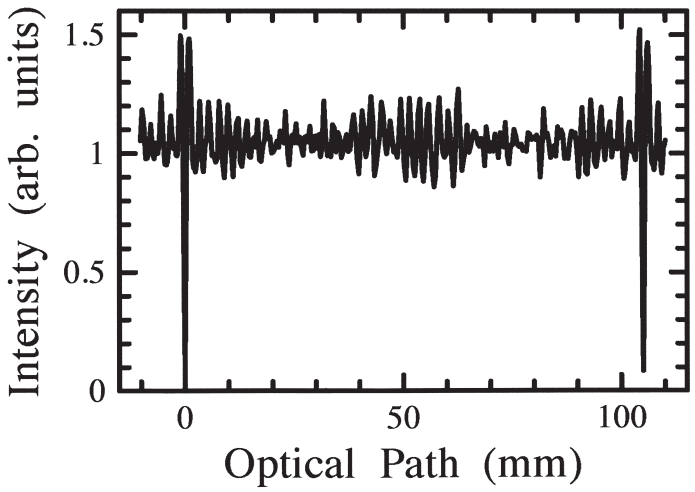

Fig.3. The interferogram observed at θ= 90°.

We appreciate Professors J. Kawamura and T. Arima of IMRAM, Tohoku University, for their encouragement and support, and professor emeritus K. Mizuno of Tohoku University for his kind support to utilize the low temperature InSb detector. We also thank Messrs. T. Tsutaya, Y. Chiba of IMRAM, the member of the optical group of Photodynamics Center, RIKEN, and the staff of LNS, Tohoku University, for their help in the experiment.

References

[1] K. Yamamoto, R. Sakakibara, S. Yano, Y. Segawa, Y. Shibata, K. Ishi, T. Ohsaka, T. Hara, Y. Kondo, H. Miyazaki, F. Hinode, T. Matsuyama, S. Yamaguti, and K. Ohtaka: Phys. Rev. E **69** (2004) 045601.

[2] N. Horiuchi, T. Ochiai, J. Inoue, Y. Segawa, Y. Shibata, K. Ishi, Y. Kondo, M. Kanbe, H. Miyazaki, F. Hinode, S. Yamaguti, and K. Ohtaka: Phys. Rev. E **74** (2006) 056601.

[3] Y. Shibata, K. Ishi, T. Tsutaya, N. Horiuchi, Y. Segawa, Y. Kondo, H. Miyazaki, F. Hinode, T. Ochiai, and K. Ohtaka: Research Report of LNS, Tohoku Univ., **39** (2006) 55.

[4] Y. Shibata, K. Ishi, T. Tsutaya, N. Horiuchi, Y. Segawa, Y. Kondo, H. Miyazaki, F. Hinode, T. Ochiai, and K. Ohtaka: Research Report of LNS, Tohoku Univ., **39** (2006) 67.

新しい管理区域入退管理システム

柴崎義信，菅原由美，結城秀行，山崎寛仁，大槻勤

東北大学院理学研究科附属原子核理学研究施設（982-0826 仙台市太白区三神峯 1-2-1）

§1．はじめに

東北大学理学研究科附属原子核理学研究施設では，放射線管理区域への入室者管理のため1998年に入退室管理システム［1］を独自開発し運用してきた。当初は比較的安定した動作を行っていたが，運用から間もなく10年となる現在，いくつかの問題が出てきている。ひとつは，管理に使用しているコンピュータのオペレーティングシステム（OS）の問題である。OSは，WindowsNT4.0を使用しているが，その後バージョンが改訂され，現在はWindows2003およびWindowsXPとなっている。しかし，管理システムは，OSのバージョンに依存したコードを使用していることや，使っているコンピュータ（PC）の制約で簡単にバージョンアップすることができない。現在，WindowsNT4.0のサポートは打ち切られており早急な対策が必要となっていた。

次の問題は，管理システムに使用しているデータベースソフトの問題が挙げられる。データベースには，マイクロソフトのアクセスを使用していた。このソフトは軽量であり開発も比較的簡単に行うことができるがデータ数が多くなったときにパフォーマンスが低下し，入退室処理に時間がかかったりシステムが停止するなどの現象が現れてきた。

また，もうひとつ問題をあげることができる。入室登録と入室のための扉の電子錠管理は，それぞれ異なるPLCにより行っている。電子錠管理では入室登録の情報が必要だが，この情報共有をPLCとネットワークで接続しているPCを中心としたOMRONのデータリンク機能を使って行っている。これは，設定のみで情報共有を行うことができ便利であるが，複数のPLCがお互いのデータに依存する関係となるため，ある箇所の障害が別の箇所に波及しシステム全体を不安定にする要因になっている。

放射線管理区域への入退室管理は，放射線取り扱い施設として重要な業務のひとつであり，システム停止の状態に陥ることは許されないことである。そのため，2006年にシステム更新のための予算化がなされ再構築をおこなった。

§2．新しいシステムの開発方針

これらの問題点を改善し，また将来の拡張や変更にも対処できるようにするためには，汎用的な技術を取り入れ，独自開発的な部分はどうしても必要な箇所に限定することが重要である。また，それぞれの機能を密に結合させないことでひとつの変更が他をも変更しなければならない状況を作り出さないことも重要である。

最近の情報技術の進歩によって，インターネットを中心とした情報伝達システムが標準的に使われるようになってきた。この技術を今回のシステムに応用することで将来への拡張性や保守性を確保できる。この中心となる技術がデータベースを中心としたWebサービスとWebアプリケーションである。

アプリケーションを作成する上では，プログラミング開発環境とプログラム言語に何を選択するかが開発効率に影響する。Webを中心とした開発では，Webブラウザが解釈できるHTMLや，スクリプトとしての

javaが一般的に使われている。これらの言語を用いて直接開発することもできるが，効率や今後の管理という側面からは必ずしも適当であるとはいえない。核理研では加速器の制御プログラム[2]の開発にはMicroSoftのVisualBasicを用いているが，今回のシステム開発に同じ環境を用いることで迅速な開発を行うことができる。

以上のことを考慮し今回のシステム更新では次のような基本方針を立てた。

1．SQL Server 2005の採用
2．Webサービスによる情報共有
3．Webブラウザによる各種情報の表示と取り出し
4．PLCのローカル化

§2．システムの構成

これまでのシステムは，ひとつのPCに多くの機能を持たせていた。それがOSのバージョンアップを阻害していたひとつの原因ともなっていた。そこで，PC毎に機能を分散させ，使い方を限定することでこの問題へ対処した。また，PCの故障時に問題が波及することを最小限にすることもできる。このためには，まずシステムが必要としている機能を整理する必要がある。機能を整理すると以下のとおりとなる。

1．データベース
2．入退室登録
3．入室ゲート管理
4．入室者一覧表示
5．入室者都度印刷
6．管理ユーザー登録
7．IDカード作成
8．月報取り出し

データベースは，ユーザー情報や入室退室の状況，ゲート通過記録などの情報を保存する機能で，これまでアクセスによって行われていたものである。保存するデータの項目は以前とそれほど変わらないが，検索速度を上げるためテーブル構造とトランザクションの方法を変えている。また，データベース管理ソフトとしてマイクロソフトが最近提供を開始したSQL2005を採用した。

入退室登録は，作業や他の目的で管理区域に入室しようとする人がまず行う作業で，入室先などの情報をデータベースへ登録する。ここでは，登録者のIDカードを読み込むためのIDセンサと，登録情報を入力するためのタッチパネルを必要とする。

入室ゲート管理は，入室登録を済ませたユーザーが入室扉を通過することを管理する機能で，通過者の情報をデータベースに記録する。ここには，電子錠制御とIDセンサ読み取りを行うためのPLCがある。

入室者一覧表示は，入室登録を済ませたユーザーとその人がゲートを通過したかどうかを表示する。

入室者都度印刷は，入退室登録を行ったユーザーをその都度印刷し記録する。

管理ユーザー登録は，新入生や新採用，転勤などで新たに核理研の管理区域に入室する必要が出てきた人をデータベースに登録する機能である。

IDカード作成は，ユーザー登録により必要となるIDカードの作成をおこなう。

月報取り出しは，月毎の管理区域入室と退室のログを取り出す機能で，個人毎及び時系列で印刷し保存する。

これらの機能で，直接PLCなどのハードウエアを制御するものについては，プログラミングの必要があることからWebサービスを利用してデータベースと通信を行う。それ以外については，Webアプリケーションとし，Webブラウザを使って表示や入力を行うことができるようにした。Webブラウザを使うことでPCの機種を限定する必要がなくなり，特定のPCを管理するわずらわしさをなくすることができる。

今回の更新では，これまでのIDカードをそのまま使うこととし，ゲートを制御しているPLCへの変更を行っていない。PLCは，専用のPCを介して制御し，ネットワークから切り離した。それぞれのPCは，専用のネットワークから所内のローカルネットワークへ接続を切り替え，これまで専用のネットワークと，所内ネットワークへ混在した接続を整理した。新しいシステムの構成とネットワーク接続を第1図に示す。

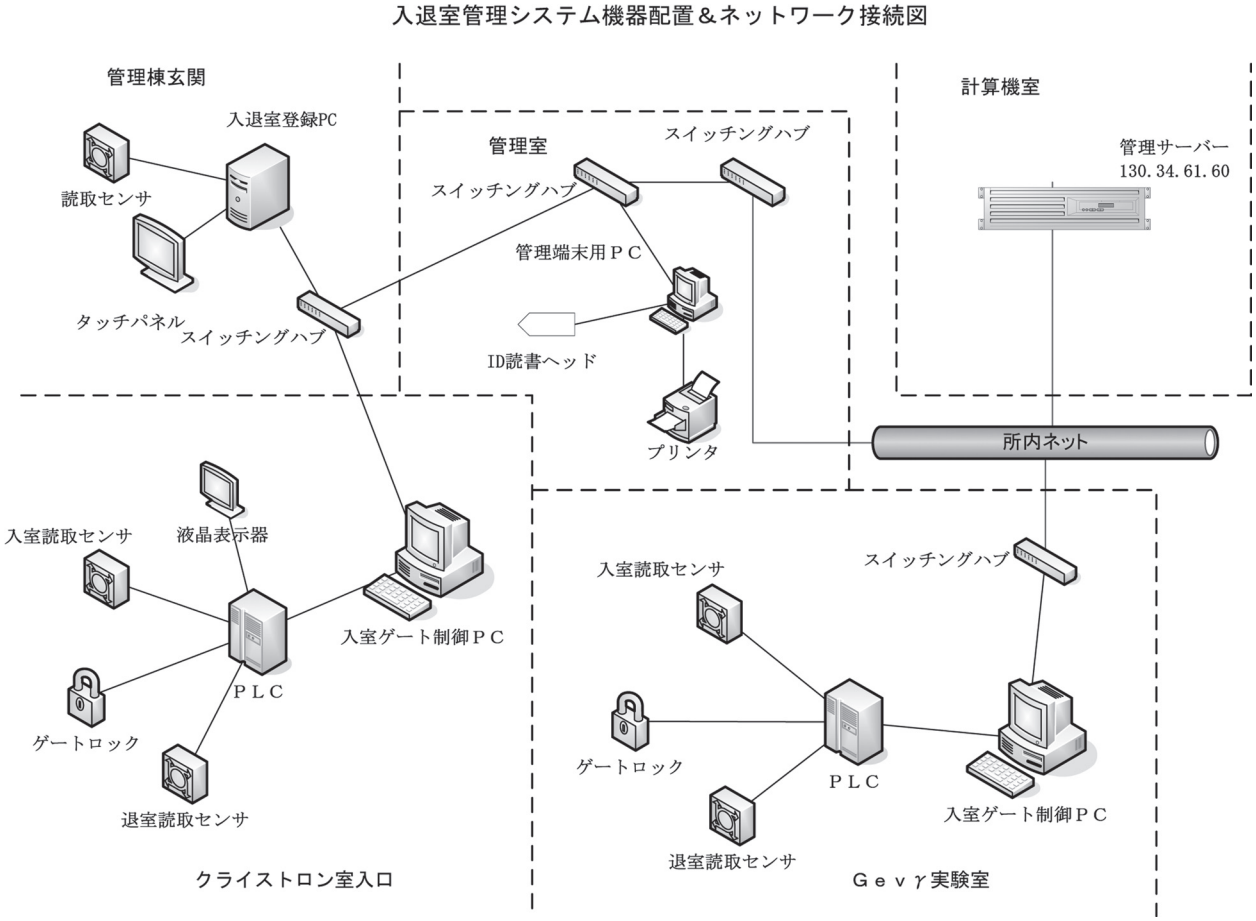

第1図　システム構成図。

(1) データベース

データベースは，このシステムの中心となるためテーブル構造が使い勝手やパフォーマンスを決める要因となる。また，これまで使っていたデータベースのテーブル構造も必要に応じて継承する必要がある。ただし最初に作られたテーブルは不必要と思われるフィールドもあるため，再度必要項目について分析を行った。

テーブルは大きく分けて次の3種類に分類した。

・共通情報　・一時情報　・記録情報

共通情報は，ユーザー情報や実験室名などの頻繁に更新されることのない情報を格納するテーブルで管理者によって登録や削除などの管理を行う。

一時情報は，ユーザーが入室している時の状態を管理するテーブルで，このシステムの動作の要となるテー

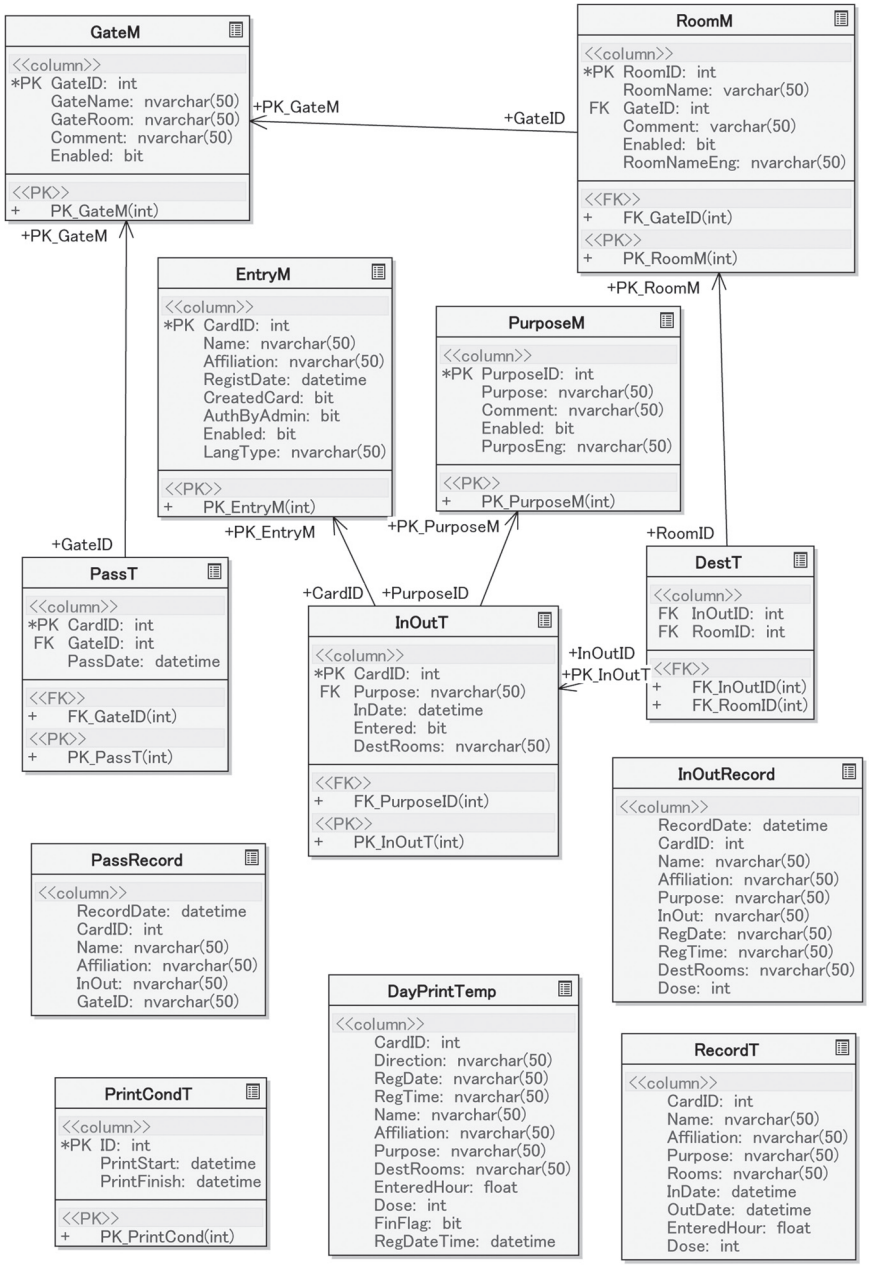

第 2 図　データベースモデル図。

ブル群である。このテーブルには，入室登録時にゲート通過や表示に必要な情報が書き込まれ，退室手続時に削除されるため頻繁にトランザクションが発生する。そのためこのテーブルの設計が全体のパフォーマンスに影響する。

記録情報は，最終的に記録として残すべきデータを格納するテーブルで，ユーザーごとに集計し入室時間や被曝線量などを管理する。

また，これ以外にユーザーインターフェースとして表示する内容を動的に変更するための情報を管理するテーブルを作成した。たとえば，日本語圏以外のユーザーには英語で表示するとか，入室目的や入室先の名前を変更したい場合などがこれにあたる。アプリケーションは表示するときにこのテーブルを参照し表示方法を変えることができるためプログラムの変更が必要なくなる。

今回の構築で作成したデータベースのテーブル構造をデータベースモデル図として第 2 図に示す。

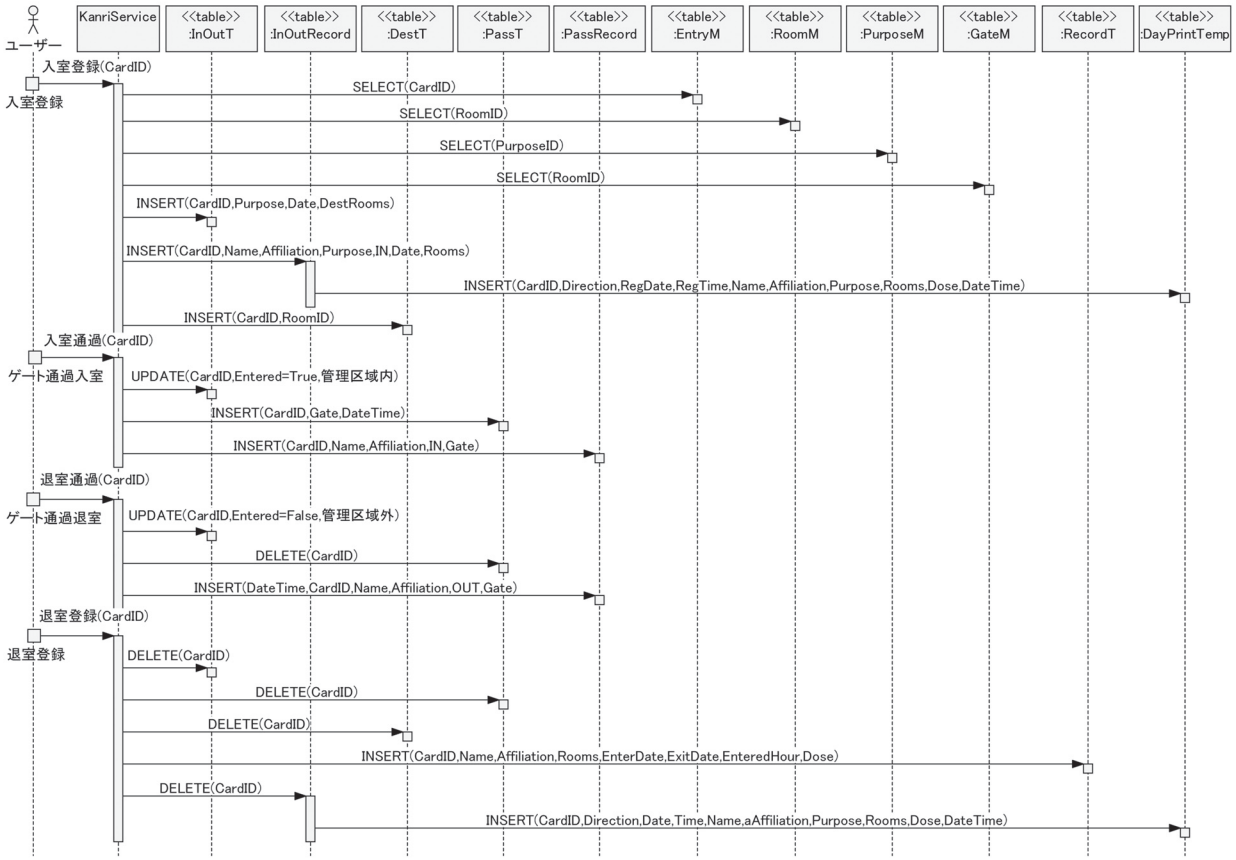

第３図　テーブルアクセスシーケンス。

これらのテーブル構造と種類は，あらかじめユーザーが入退室するためにはどのようにするか，またそのときにどのような情報が必要かを登録から退室手続までのシナリオを作成し，そこからテーブルへアクセスする手順を視覚化した。この作業を繰り返し，必要なものと不必要なものを切り分け作成するテーブルの確定とテーブルから情報を取り出すシーケンスを決定した。この作業は，このシステムを管理する管理者側からの分析も行い，より洗練させている。第３図にユーザーが入退室する手順による各テーブルへのアクセスシーケンスを示す。

（2）　Webサービスと分散オブジェクト

入退室登録端末やゲートを管理している機器などのクライアントからデータベースへのアクセスは，直接には行わず，Webサービスを使って入退室情報をカプセル化したオブジェクト（第４図参照）の交換で実現している。それによって，クライアント側ではデータベースの構造を気にする必要がなくなりオブジェクトに処理を依頼するだけですむ。また，テーブル構造などを何らかの理由で変更する場合にもクライアントのプログラムを変える必要がなくなり管理作業を単純にすることが可能となった。

（3）　インターフェースプログラムと開発環境

このシステムは，実際に入退室を行うユーザーや，ユーザー及び記録情報を管理する管理者との対話を行うため必要な情報の表示および入力のためのインターフェースが必要である。これを入退室登録者の流れに沿ってまとめると第５図のようなアプリケーションが必要となる。

これらのプログラムを作るにあたっては，先に述べた方針に従って，可能なものはWebアプリケーションとしWebブラウザで対応できるようにした。そのため特別のハードウエアを動作させる必要のないものは，

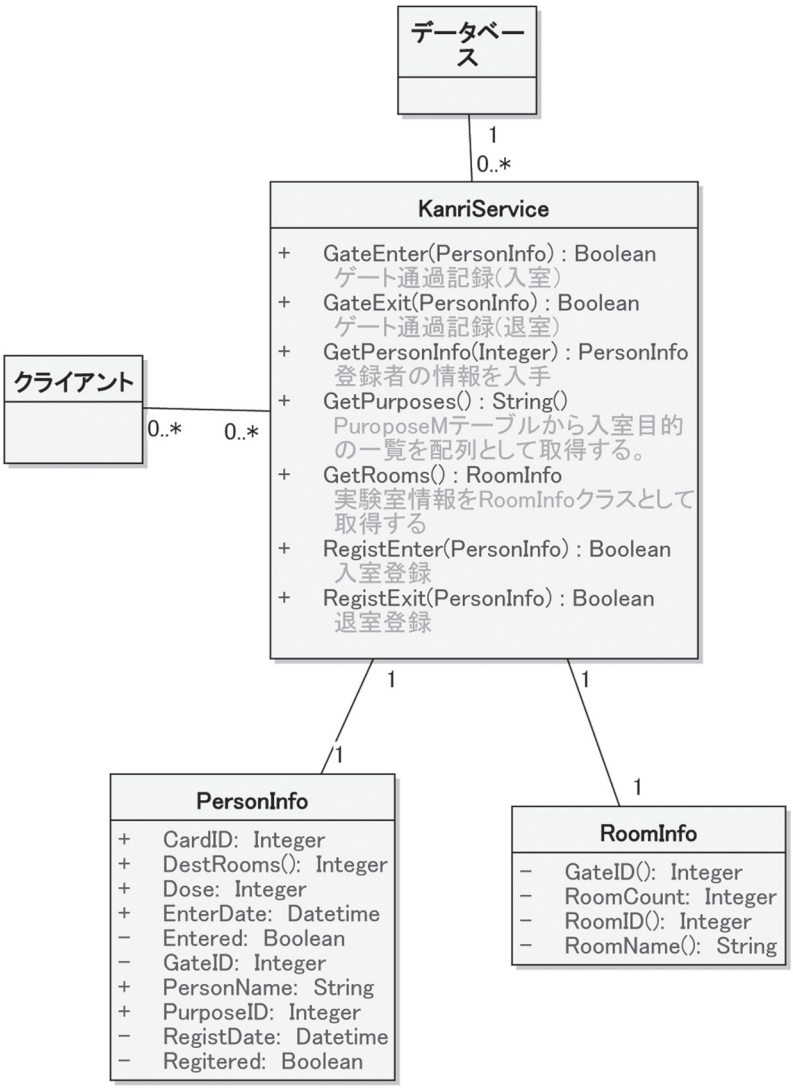

第4図　Webサービスのクラス図。

Webサーバーを中心としたWebアプリケーションとして構成している。

Webアプリケーションの作成は，HTMLを使ってページを作成し，動的に動作する機能はスクリプトとしてページに埋め込む。ユーザーからのアクションによってポストバックされた情報は，その種類に応じてザーバー側で処理されその結果を新しいWebページとして構築しブラウザに表示する。この一連の流れをプログラムする方法としてASP.NETを使った。これは，コードビハインドという技術を使って，表示する部分と動作の部分を分割してプログラムする方法で，表示部分にプログラムが入り込まないのでそれぞれに専念した開発を行うことができるのが特徴である。また，動作コードについてはVisualBasicで記述することができるためこれまでのプログラミング技術をそのまま使うことが可能であり開発時間の短縮を図ることができる。

このシステムでは，入退室時に登録したデータを個人ごとや日付ごとに入室時間とそのときの被曝線量の累計を月単位で記録し保管する。そのためには，記録しているデータを加工し並べ替えを行いそれらの閲覧と印刷あるいはエクセルなどの別の汎用アプリケーションへのエキスポートなどの機能を必要とする。これらの機能をWebアプリケーションとして作成することも可能であるが，今回採用したSQLサーバー2005には，レポーティングサービスとしてこれらを実現する方法を備えている。開発は，Webアプリケーション

を開発する場合と同じ開発環境を使い，表示するために必要な表をフォーム上に配置し，データベースからどのようにデータを取り出すかのクエリを設定するだけで実現できる。クエリコマンドの作成もウィザードが準備されており，その指示に従って入力するだけで高度なクエリ文の作成ができる。第6図に開発中の様子と実際にＷｅｂブラウザで表示したページを示す。

今回の開発に用いた環境およびハードウエアの仕様を次に示す。

サーバー：Dell PowerEdge SC1425

CPU: Xeon64bit 3GHz

メモリ：2GB

OS: WindowsServer2003x64

データベース：SQL2005

開発環境：VisualStudio2005

開発言語：VisualBasic.NET

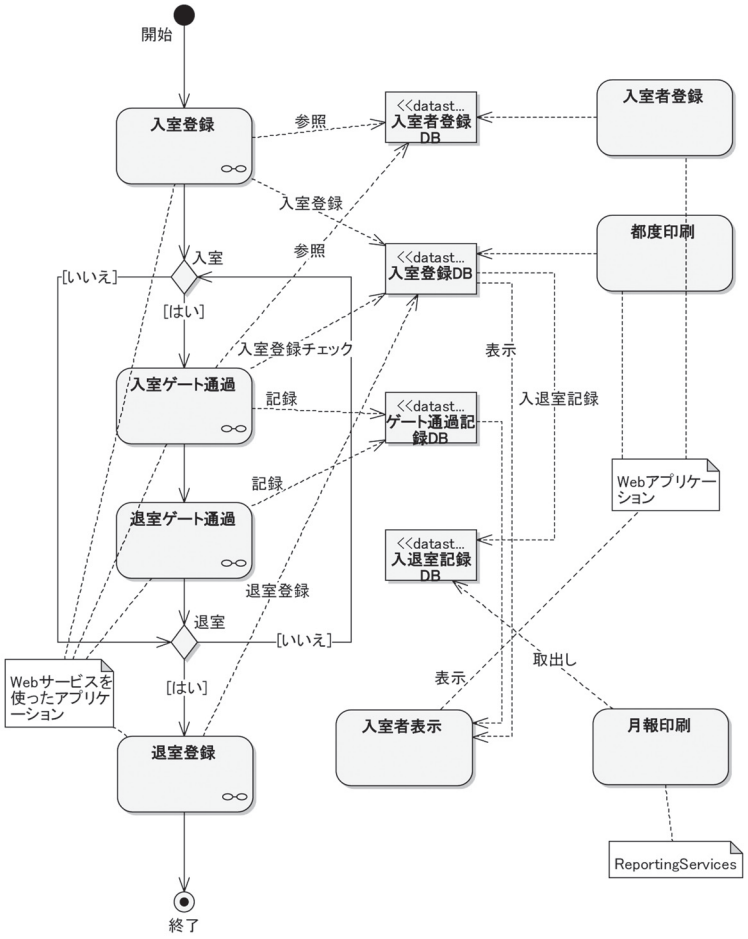

第5図　入退室登録の流れとアプリケーション。

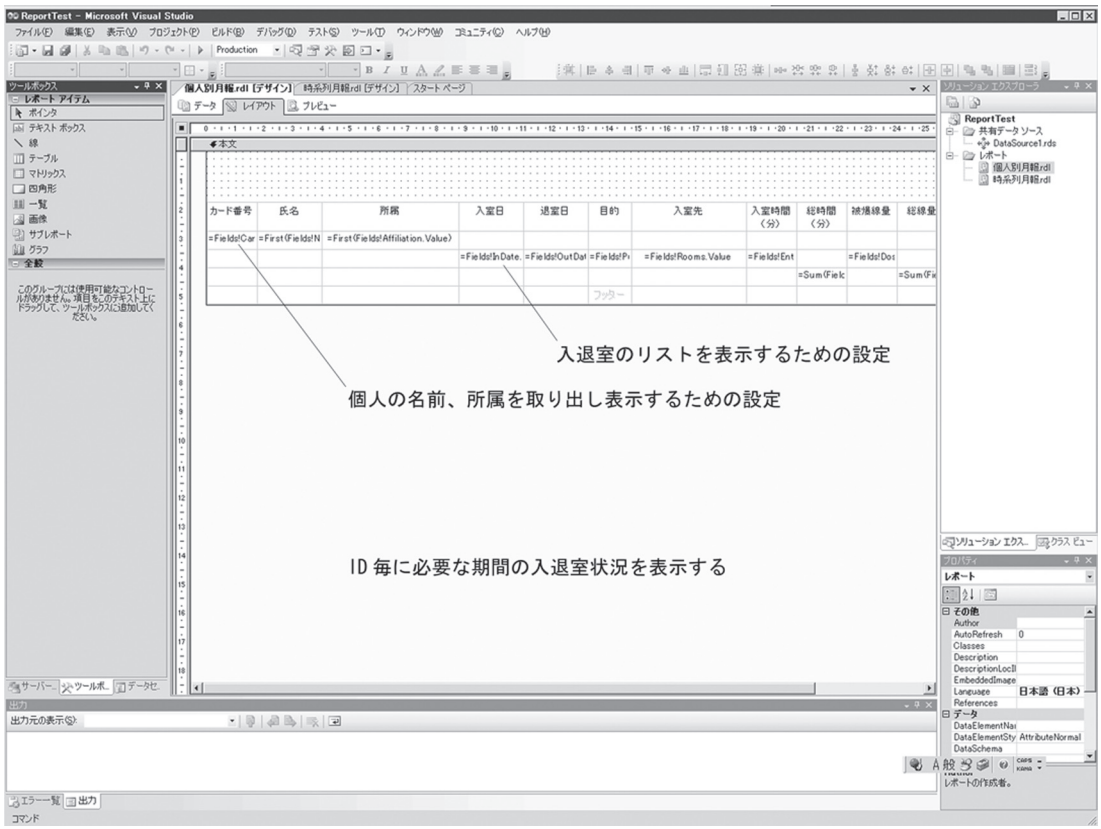

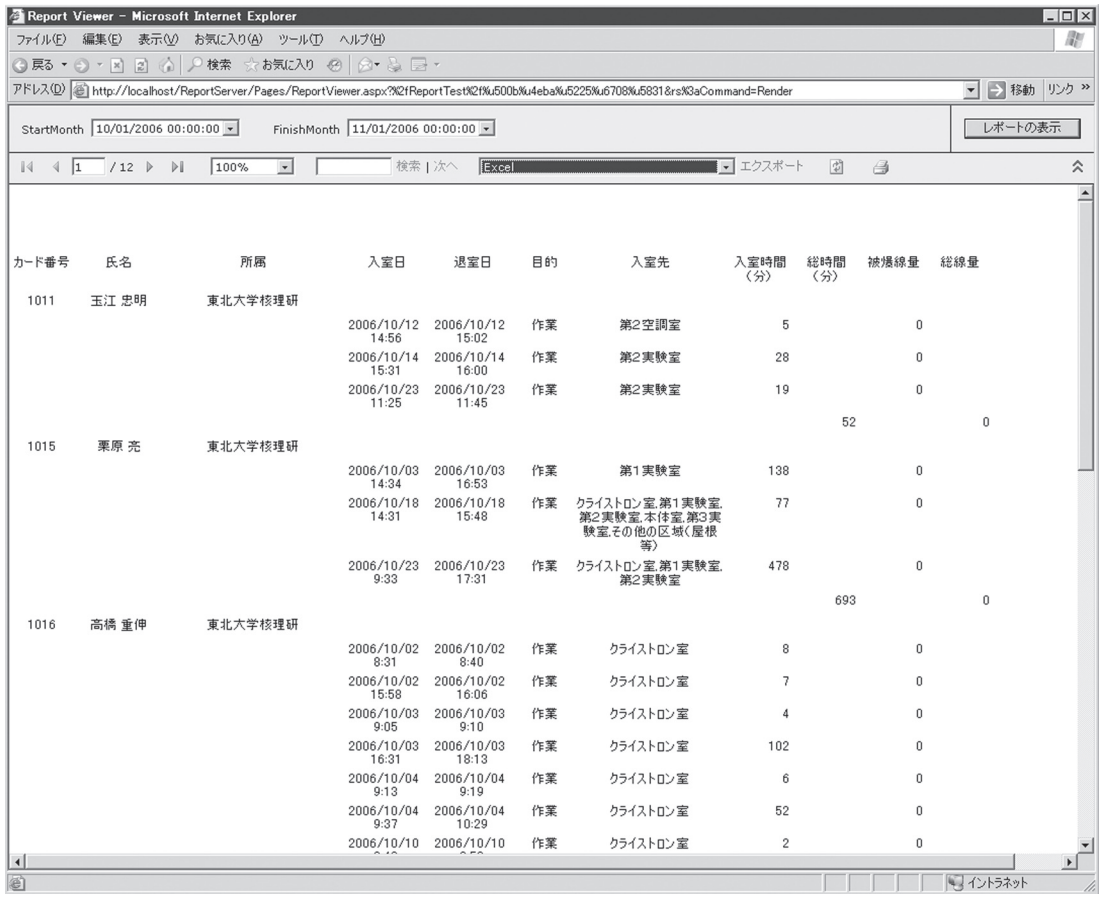

第 6 図　VisualStudio によるレポート開発（上）と開発したレポートの表示（下）。

§3．運用状況

このシステムは，2006年3月より開発に着手し，8月上旬に旧環境との入れ替えを行い運用を開始した。運用前の試験については，かなり限定された環境のみでしか行うことができなかったが，運用を開始した8月からこれまでのシステム動作の中で若干のプログラムのバグによる問題以外は大きく仕様を見直すような不具合はなく順調に稼働している。一部，IDカード読み取り部で読み取りができない不具合が発生するという以前からの問題は残っている。これについては，PLCの読み取りプログラムを変更する必要がある。

システムのパフォーマンスは，PCの性能の問題もあるが，旧システムより体感的に速く感じられ入退室時のストレス軽減につながっている。また，入室状況はWebアプリケーションとして提供しており，どこからでも確認することが可能となっている。

§4．ま と め

今回の目的である新しい放射線管理区域への管理区域入退管理システム構築は完了した。これにより，懸案となっていたコンピュータの更新と最新のOSへの対応が可能となった。また，パフォーマンスも向上し登録作業も迅速に行えるようになった。ただ，一部従来の機器がそのまま残っており更新等の作業は必要である。

システム構築にあたっては，まず入退室管理システムとしての機能の分析を行い次に開発をVisualStudio2005およびASP.NETを使って機能の部品化を図った。それにより短い開発期間によって完成することができた。

参　考　文　献

[1]　宮本篤他：“管理区域入退管理システムの開発”，RADIOISOTOPES, Vol.52, No.12（2003）.

[2]　Y. Shibasaki *et al*.: New Control System for the LNS Linac, PCaPAC2002 MO-P20（2002）.

Ⅳ. List of Publication

List of Publication（論文リスト）（2005.1～2005.12）

Papers Published in Refereed Journals

K^0 Photoproduction on ^{12}C in the Threshold Region.

T. Watanabe, S. Endo, Y. Fujii, O. Hashimoto, K. Hirose, T. Ishikawa, K. Ito, H. Kanda, M. Katoh, T. Kinoshita, O. Konno, K. Maeda, A. Matsumura, Y. Miura, F. Miyahara, H. Miyase, K. Mizunuma, T. Nakabayashi, S.N. Nakamura, H. Nomura, Y. Okayasu, T. Osaka, A. Otani, M. Oyamada, A. Sasaki, T. Sato, H. Shimizu, T. Takahashi, T. Tamae, H. Tamura, T. Terasawa, H. Tsubota, K. Tsukada, M. Ukai, M. Utoyama, M. Wakamatsu, H. Yamauchi, Y. Yamaguchi, Y. Yamamoto, and H. Yamazaki

Nuclear Physics **A754** (2005) 327-331.

Direct Evidence of Core Excitation in the Giant Resonance through the (e,e'n) Reaction.

T. Saito, K. Yoshida, M. Oikawa, Y. Suga, T. Nakagawa, T. Tohei, K. Abe, and H. Ueno

Phys. Rev. **C71** (2005) 064313 (1-5).

The 1.2 GeV Photon Tagging System at LNS-Tohoku.

H. Yamazaki, T. Kinoshita, K. Hirota, T. Katsuyama, T. Itoh, A. Katoh, T. Nakabayashi, O. Konno, T. Takahashi, K. Maeda, J. Kasagi

Nucl. Instr. Meth. **A536** (2005) 70-78.

ϕ Photo-production from Li, C, Al and Cu nuclei at $E\gamma$ =1.5-2.4 GeV.

T. Ishikawa, D.S. Ahn, J.K. Ahn, H. Akimune, W.C. Chang, S. Date, H. Fujimura, M. Fujiwara, K. Hicks, T. Hotta, K. Imai, H. Kawai, K. Kino, H. Kohri, T. Matsumura, T. Mibe, K. Miwa, M. Miyabe, M. Morita, T. Murakami, N. Muramatsu, H. Nakamura, M. Nakamura, T. Nakano, M. Niiyama, M. Nomachi, Y. Ohashi, T. Ooba, D.S. Oshuev, C. Rangacharyulu, A. Sakaguchi, Y. Shiino, Y. Sakemi, H. Shimizu, Y. Sugaya, M. Sumihama, Y. Toi, H. Toyokawa, C.W. Wang, T. Yorita, M. Yosoi, and R.G.T. Zegers

Phys. Lett. **B608** (2005) 215-222.

Near-Threshold Diffractive ϕ Meson Photoproduction from the Proton.

T. Mibe, W.C. Chang, T. Nakano, D.S. Ahn, J.K. Ahn, H. Akimune, Y. Asano, S. Daté, H. Ejiri, H. Fujimura, M. Fujiwara, K. Hicks, T. Hotta, K. Imai, T. Ishikawa, T. Iwata, H. Kawai, Z.Y. Kim, K. Kino, H. Kohri, N. Kumagai, S. Makino, T. Matsuda, T. Matsumura, N. Matsuoka, K. Miwa, M. Miyabe, Y. Miyachi, M. Morita, N. Muramatsu, M. Niiyama, M. Nomachi, Y. Ohashi, T. Ooba, H. Ohkuma, D.S. Oshuev, C. Rangacharyulu, A. Sakaguchi, T. Sasaki, P.M. Shagin, Y. Shiino, H. Shimizu, Y. Sugaya, M. Sumihama, A.I. Titov, Y. Toi, H. Toyokawa, A. Wakai, C.W. Wang, S.C. Wang, K. Yonehara, T. Yorita, M. Yoshimura, M. Yosoi, and R.G.T. Zegers

Phys. Rev. Lett. **95** (2005) 182001 (1-5).

Investigation of the Conjectured Nucleon Deformation at Low Momentum Transfer.

N.F. Sparveris, R. Alarcon, A.M. Berstein, W. Bertozzi, T. Botto, P. Bourgeois, J. Calarco, F.

Casagrande, M.O. Distler, K. Dow, M. Farkondeh, S. Georgakopoulos, S. Gilad, R. Hicks, M. Holtrop, A. Hotta, X. Jiang, A. Karabarounis, J. Kirkpatrick, S. Kowalski, R. Milner, R. Miskimen, I. Nakagawa, C.N. Papanicolas, A.J. Sarty, Y. Sato, S. Širca, J. Shaw, E. Six, S. Stave, E. Stilaris, T. Tamae, G. Tsetalovich, C. Tschalaer, W. Turchinetz, Z.-L. Zhou, and T. Zwart

Phys. Rev. Lett. **94** (2005) 022003 (1-4).

Measurement of the ^{3}He(e,e'p)pn Reaction at High Missing Energies and Momenta.

Benmokhtar, M.M. Rvachev, E. Penel-Nottaris, K.A. Aniol, W. Bertozzi, W.U. Boeglin, F. Butaru, J.R. Calarco, Z. Chai, C.C. Chang, J.-P. Chen, E. Chudakov, E. Cisbani, A. Cochran, J. cornejo, S. Dieterich, P. Djawotho, W. Duran, M.B. Epstein, J.M. Finn, K.G. Fissum, A. Frahi-Amoroun, S. Frullani, C. Furget, F. Garibaldi, O. Gayou, S. Girad, R. Gilman, C. Glashausser, J.-O. Hansen, D.W. Higinbotham, A. Hotta, B. Hu, M. Iodice, R. Iomni, C.W. de Jager, X. Jiang, M.K. Jones, J.J. Kelly, S. Kox, M. Kuss, J.M. Laget, R. De Leo, J.J. LeRose, E. Liatard, R. Lindgren, N. Liyanage, R.W. Lourie, S. Malov, D.J. Margaziotis, P. Markowitz, F. Merchez, R. Michaels, J. Mitchell, J. Mougey, C.F. Perdrisat, V.A. Punjabi, G. Quéméner, R.D. Ransome, J.-S. Réal, R. Roché, F. Sabatié, A. Saha, D. Simon, S. Strauch, R. Suleiman, T. Tamae, J.A. Templon, R. Tieulent, H. Ueno, P.E. Ulmer, G.M. Urciuoli, E. Voutiner, K. Wijesooriya, and B. Wojtsekhowski

Phys. Rev. Lett. **94** (2005) 082305 (1-5).

Quasielastic ^{3}He(e,e'p)^{2}H Reaction at Q^2 = 1.5 GeV^2 for Recoil Momenta up to 1 GeV/c.

M.M. Rvachev, F. Benmokhtar, E. Penel-Nottaris, K.A. Aniol, W. Bertozzi, W.U. Boeglin, F. Butaru, J.R. Calarco, Z. Chai. C.C. Chang, J.-P. Chen, F. Chudakov, E. Cisbani, A. Cochran, J. Cornejo, S. Dieterich, P. Djawotho, W. Duran, M.B. Epstein, J.M. Finn, K.G. Fissum, A. Frahi-Amroun, S. Furullani, C. Furget, F. Garibaldi, O. Gayou, S. Gilad, R. Gilman, C. Glashausser, J.-O. Hansen, D.W. Higinbotham, A. Hotta, B. Hu, M. Iodice, R. Iomni, C.W. de Jager, X. Jiang, M.K. Jones, J.J. Kelly, S. Kox, M. Kuss, J.M. Laget, R. De Leo, J.J. LeRose, E. Liatard, R. Lindgren, N. Liyanage, R.W. Lourie, S. Malov, D.J. Marganziotis, P. Markowitz, F. Merchez, R. Micaels, J. Mithcell, J. Mougey, C.F. Perdrisat, V.A. Punjabi, G. Quéméner, R.D. Ransome, J.-S. Réal, R. Roché, F. Sabatié, A. Saha, D. Simon, S. Strauch, R. Suleiman, T. Tamae, J.A. Templon, R. Tieulent, H. Ueno, P.E. Ulmer, G.M. Yriuoli, E. Voutier, K. Wijesooriya, and B. Wojtsekhowski

Phys. Rev. Lett. **94** (2005) 192302 (1-5).

First Beam Test on a BSO Electromagnetic Calorimeter.

H. Shimizu, F. Miyahara, H. Hariu, T. Hayakawa, T. Ishikawa, M. Itaya, T. Iwata, T. Kinoshita, M. Moriya, T. Nakabayashi, T. Sasaki, Y. Tajima, S. Takita, M. Yamamoto, H. Yamazaki, H.Y. Yoshida, and Y. Yoshida

Nucl. Instr. and Meth. Phys. Res. **A550** (2005) 258-266.

不安定核電子散乱実験のための自己閉じ込め型不安定核標的(SCRIT).

若杉昌徳，伊藤祥子，江本隆，大西哲哉，栗田和好，小関忠，白井敏之，須田利美，竹田浩之，

玉江忠明，頓宮拓，中村仁音，野田章，古川幸弘，増田鉄也，森川斉，矢野安重，王頌
加速器，**2** (2005) 337-347.

Production of Th-229m in Nuclear Reaction and its Identification by Alpha-spectrometry.

H. Kikunaga, Y. Kasamatsu, K. Takamiya, T. Mitsugashira, M. Hara, T. Ohtsuki, H. Yuki, A. Shinohara, S. Shibata, N. Kinoshita, A. Yokoyama, and T. Nakanishi

Radiochimica Acta **93** (2005) 507-510.

Photon Activation Analysis of Carbon in Glasses for Fiber Amplifiers by using the Flow Method for the Rapid Separation of ^{11}C.

K. Shikano, A. Mori, M. Shimizu, T. Ohtsuki, H. Yuki, K. Masumoto

J. Radioanal. Nucl. Chem. **266** (2005) 211-216.

Formation of ^{210}Po @C60.

T. Ohtsuki and K. Ohno

Phys. Rev. **B72** (2005) 153411 (1-3).

Investigation of the Decay Property of ^{229m}Th by Photon Detection.

Y. Kasamatsu, H. Kikunaga, K. Takamiya, T. Mitsugashira, T. Nakanishi, Y. Ohkubo, T. Ohtsuki, W. Sato, and A. Shinohara

Radiochim. Acta, **93** (2005) 511-514.

Papers Published in International Conference Proceedings

ϕ Photo-Production from Nuclei at SPring-8/LEPS.

T. Ishikawa

Proceedings of the International Workshop on Quark Nuclear Physics 2005 (2005).

Detection of Nuclear De-excitation Gamma-rays in Water Cherenkov Detector.

K. Kobayashi, Y. Itow, M. Shiozawa, M. Yosoi, H. Toyokawa, H. Akimune, H. Ejiri, H. Fujimura, M. Fujiwara, K. Hara, K.Y. Hara, T. Ishikawa, M. Itoh, T. Kawabata, M. Nakamura, H. Sakaguchi, Y. Sakemi, H. Takeda, M. Uchida, T. Yamada, Y. Yasuda, H.P. Yoshida, and R.G.T. Zegers

Nuclear Physics B - Proceedings Supplements, **139** (2005) 72-76.

Lattice Modification of a 1.2 GeV STB Ring for Generation of High Energy Gamma-rays using Internal Target Wire.

F. Hinode, H. Hama, M. Kawai, A. Kurihara, A. Miyamoto#, M. Mutoh, M. Nanao, Y. Shibasaki, K. Shinto, S. Takahashi, and T. Tanaka

Proceedings of 2005 Particle Accelerator Conference, Knoxville, Tennessee, (2005) 2458-2460.

Study of Slow Beam Extraction through the Third Order Resonance with Transverse Phase Space Manipulation by a Mono-frequency RFOK.

A. Miyamoto, F. Hinode, M. Kawai, K. Shinto, T. Tanaka, and H. Hama

Proceedings of 2005 Particle Accelerator Conference, Knoxville, Tennessee, (2005) 1892-1894.

Simulation Study of a Thermionic RF Gun for High Brightness and Short Pulse Beam.

T. Tanaka, F. Hinode, M. Kawai, A. Miyamoto, K. Shinto, and H. Hama

Proceedings of 2005 Particle Accelerator Conference, Knoxville, Tennessee, (2005) 3499-3501.

An Independently Tunable Cells Thermionic RF Gun (ITC-RF GUN) for Sub-picosecond Short Pulse.

T. Tanaka, F. Hinode, M Kawai, and H. Hama

Proceedings of the 27th International Free Electron Laser Conference, FEL2005, Stanford, CA, USA (2005) 142-145.

Review

Is the Property of Mesons Modified in the Nuclear Medium? " ϕ Meson Photoproduction from Nuclei".

T. Ishikawa and M. Fujiwara

ROKKO Publishing & Sale Co. SPring-8 Research Frontiers 2004 (2005) 149-150.

フラーレンに内包された軌道電子捕獲崩壊核種^{7}Beの半減期.

大槻勤

アイソトープニュース（日本アイソトープ協会）**5** (2005)14-17.

放射性同位元素の半減期は変化するか？：C60内に^{7}Beが内包された場合.

大槻勤

日本物理学会誌（最近の研究から）**7** (2005) 551-554.

フラーレン中の放射性同位元素Be-7の半減期.

大槻勤

放射線化学 **80** (2005) 41-46.

C60中のEC崩壊核種（ベリリウム-7）の半減期絶対測定.

大槻勤

JAERI-Conf **2005-011** (2005) 126-130.

V. Approved Experiments

平成17年度前期採択課題一覧表

課題番号	課　　題　　名	申込責任者	採　択 シフト数
原子核関連分野			
2534	D(γ, η) 反応における Eγ～1.02 GeV の新共鳴状態の確定	山崎　寛仁	39
2535	A(γ, η) 反応による核子共鳴 D13 (1520) の研究	笠木治郎太	20
2536	４π立体角　多重ガンマ線検出器群 FOREST（仮称）の建設	石川　貴嗣	施設実施
放射光関連分野			
2537	フォトニック結晶からのコヒーレントな放射の研究(5) －フォトニック結晶配置方位依存性の測定－	柴田　行男	8
放射化学・物性関連分野			
2538	長寿命放射性核種の環境中移行における基礎化学反応研究	関根　　勉	2
2539	光量子放射化分析法による光通信用材料中の不純物評価	鹿野　弘二	1
2540	標識化による金属内包フラーレン及びヘテロフラーレンの研究及びその応用	大槻　　勤	2
2541	Ac-229から Th-229m, g への壊変過程に関する研究	中西　　孝	1
2542	Th-229m の製造とその崩壊特性	三頭　聰明	1
2543	宇宙化学的試料および環境試料の光量子放射化分析	海老原　充	2
2544	電子ビームによるフリーラジカル生成の研究	結城　秀行	1
2545	金属及び半導体材料中の軽元素の定量のための分離・捕集法の開発	桝本　和義	2
2546	水素誘起空孔による拡散の促進	佐藤伊佐務	1
2547	DNA２本鎖切断の遺伝的影響；１倍体酵母と二倍体酵母の比較研究	山崎　仁丈	4

平成17年度後期採択課題一覧表

課題番号	課　　題　　名	申込責任者	採　択 シフト数
原子核関連分野			
2548	A(γ, η)反応における閾値エネルギー近傍でのS_{11}共鳴の励起関数測定 －核媒質による共鳴エネルギー減少の可能性－	笠木治郎太	24
2549	NKS2 実験のためのBM4 ガンマビームライン整備	前田　和茂	12
2550	指向性をもった電子検出器の性能評価	友野　　大	12
2551	重水素原子核標的での2π光生成反応の研究	前田　和茂	20
2552	Photoproduction of Neutral Kaons on Deuterium Target near Threshold Region	橋本　　治	52
放射光関連分野			
2553	フォトニック結晶からのコヒーレントな放射の研究(6) －フォトニック結晶配置依存性の測定－	柴田　行男	4
放射化学・物性関連分野			
2554	標識化による金属内包フラーレン及びヘテロフラーレンの製造及びその応用研究	大槻　　勤	2
2555	長寿命放射性核種の環境中移行における基礎化学反応研究	関根　　勉	2
2556	水素誘起空孔による拡散の促進	山崎　仁丈	1
2557	制動放射線誘導放射性核種の生成量に関する実測値と計算値の比較	中西　　孝	3
2558	光量子放射化分析法による光通信用材料中の不純物評価	鹿野　弘二	1
2559	金属及び半導体材料中の軽元素の定量のための分離・捕集法の開発	桝本　和義	2
2560	宇宙化学的試料および環境試料の光量子放射化分析	大浦　泰嗣	2
2561	固体抽出剤を用いた希土類元素とアクチノイド元素の分離に関する研究	鈴木　達也	3
2562	電子ビームによるフリーラジカル生成の研究	結城　秀行	1